Airborne and Underwater Response of Acoustic Structures

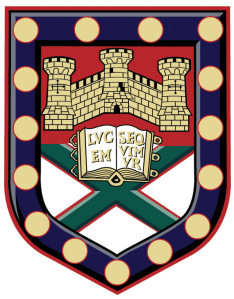

A. R. J. Murray

School of Physics

University of Exeter

A thesis submitted for the degree of

Doctor of Philosophy in Physics

May 2014

Airborne and Underwater Response of Acoustic Structures

Submitted by Alasdair Robert John Murray to the University of Exeter as a thesis for the degree of Doctor of Philosophy in Physics
2014

I certify that all material in this thesis which is not my own work has been identified and that no material has previously been submitted and approved for the award of a degree by this or any other University.

Alasdair Robert John Murray
2014

To my parents Ian and Mary for their endless support and encouragement.

Acknowledgements

Writing has been a mostly lonely and soul destroying task. So to all those over the past four years who have been there and kept me (mostly) sane I thank you eternally.

To Alastair, Roy, and Ian who have provided so many insights when my knowledge was found lacking. For finding new perspectives when I exhausted all my own. A few lines doesn't really show my appreciation enough. I will never forget my first year when Ian and Roy would verbally battle over the underlying physics of my work, while I marvelled at the 'ball' going back and forth.

To Graham and Rob at Sonardyne who helped to fund this research. I'm not sure whether anything commercially useful came out of this project, only the future will tell, but it has certainly been an worthwhile experience for me and I thank you for supporting research. Also, to Adam at Sonardyne who arranged so much stuff for me.

To Euan who shared his modal matching code, was patient while I wrapped my head around it and helped develop the codes used within.

To James Bell with whom the first experiments began. As enjoyable as our time building 'dens' were, I concede that I am glad the methods have moved on somewhat. We can now walk rather than crawl around the kit and there is no more listening to ear splitting single tones through the night.

To everyone who has read, amended and suggested improvements for this thesis. I dread to imagine how it would have turned out without your input.

To the workshop technicians who have worked tirelessly. In particular to Nick and Kev who have spent numerous hours producing samples and experimental kit just so I can come back and ask for more. A number of large experimental kits took form during the past four years and both of you have been excellent sounding boards for what we can and can't do...usually followed by finding a way to do what we can't do anyway. I can't apologise enough for all those arrays of thousands of holes and slits that I had you produce for me.

To my friends in Exeter and around the world. You've provided so many stories that I'd love to share. Unfortunately this is not the place and I am not capable of doing them justice.

To my colleagues in physics who made it an enjoyable place to work. For fear of missing someone I'll refrain from naming names, you know who you all are. Many of you have provided input of some form through discussions and editorial comments on this work, I thank you eternally and suspect that there may well be cakes in the near future.

To those on the squash ladder, it will always frustrate me that I couldn't beat some of you more often and others of you at all.

To those who played poker. Overall I think that I broke even and I doubt there shall ever be a better way to mix ice cubes and whisk(e)y.

Finally, and most of all, to my family who've always been there through thick and thin. I wouldn't be where I am without all of your knowledge, encouragement and support.

Abstract

Acoustics is a vast subject that has been utilised in many forms for millennia. Recent work has, amongst other things, explored the control of sound using geometric structure to complement inherent material properties. In this thesis, structured plates and surfaces are exploited to engineer specific acoustic responses. The acoustic transmittance and reflectance of these systems is explored in air and underwater to further understanding and develop structures that possess tailored acoustic properties.

Original investigations are presented across six chapters. The first three investigations explore the transmittance of periodically perforated plates in air. The fourth investigation considers a non-resonant mechanism of obtaining complete transmission by varying the fluid environment and the fluid in the apertures of a periodically perforated plate is explored. The fifth investigation considers the transmittance through a slit in an acoustically soft plate underwater. Finally, the surface waves supported on periodically structured surfaces are explored by observing the reflectance of the surface.

An acoustic field incident upon a perforated plate is partly transmitted. However, at frequencies dictated by the thickness of the plate, the acoustic field is completely transmitted. Stacking two plates with a small separation creates a resonant cavity between the plates that is the origin of a narrow acoustic stop-band at the frequency of the resonance. By varying the offset of the stacked plates and by varying the gap between the plates the frequency of this acoustic stop band is controlled. Altering the geometry of the plate surface within the gaps allows the gap to behave like an array of Helmholtz resonators, in doing so the frequency of the acoustic stop-band is significantly lowered.

Varying the acoustic properties of the fluid contained within the apertures of a periodically perforated plates changes how sound is transmitted through the structure. By careful choice of the fluid environment and aperture media, it is demonstrated numerically that broadband total transmittance can be obtained.

Acoustic tunnelling is demonstrated through an acoustically soft-walled slit underwater. The slit exhibits a cut-off frequency below which no propagating waves can exist, in contrast to a rigid-walled slit where propagating waves exist down to zero frequency. Resonant acoustic tunnelling is observed through two closely spaced slits in a series connection, at a frequency below the cut-off frequency of the lowest supported propagating mode.

A preliminary study of pseudo surface acoustic waves on periodically structured surfaces observes the excitation of surface waves in reflection. A long pitch grating, added to the surface allows diffractive coupling of incident acoustic radiation to the surface wave. However, the height of the grating above the sample is shown to strongly affect the frequency at which the surface wave is detected.

All the structures investigated may be designed to provide a desired response by careful choice of the geometry and materials.

Contents

Contents i

List of Figures vii

1 Introduction 1

1.1 Outline of Thesis . . . 4

2 Background 7

2.1 Introduction . . . 7

2.1.1 Common Notation . . . 7

2.2 The Acoustic Wave Equation . . . 8

2.2.1 The Continuity Equation . . . 8

2.2.2 The Equation of State . . . 9

2.2.3 The Force Equation . . . 9

2.2.4 The Linear Wave Equation . . . 10

2.2.5 Harmonic Plane Waves . . . 11

2.3 Impedance . . . 12

2.3.1 Geometric Acoustic Impedance . . . 13

2.4 Pipe Acoustics . . . 13

2.4.1 Pipes Terminated by a Single Closed End . . . 14

2.4.2 Pipes Terminated by an Open End . . . 14

2.4.3 The Helmholtz Resonator . . . 15

2.5 Acoustic Losses . . . 17

2.6 Floquet Theory . . . 18

3 Techniques Used to Simulate the Acoustic Response 21

3.1 Introduction . . . 21

3.2 Analytic Treatment . . . 21

3.3 Modal Matching Method . . . 22

3.4 Finite Element Method (FEM) . . . 23

3.4.1 Solving the Acoustic Equations in the Mesh . . . 23
3.4.2 Types of Study . . . 25
3.4.3 Boundary Conditions and Domain Assignments . . . 25
3.4.4 Meshing . . . 26
3.4.5 Extracting Solutions . . . 27
3.5 Advantages and Disadvantages of the Three Methods . . . 27

4 Techniques Used to Measure the Acoustic Response 29
4.1 Introduction . . . 29
4.2 Airborne Experiments . . . 29
4.2.1 Apparatus . . . 29
4.2.2 Collimating Mirrors . . . 30
4.2.3 Experimental Arrangement for Transmission Experiments . . . 30
4.2.4 Experimental Arrangement for Reflection Experiments . . . 32
4.3 Underwater Experiments . . . 32
4.3.1 Apparatus . . . 32
4.3.2 Experimental Arrangement for Underwater Transmission Experiments . . . 32
4.4 Data Acquisition . . . 33
4.4.1 Additional Data Obtained Using Continuous Wave Method . . . 35
4.5 Frequency Range . . . 35
4.5.1 Airborne Frequency Range . . . 36
4.6 Data Presentation . . . 36

5 Acoustic Transmission of Hole Arrays in Air 37
5.1 Introduction . . . 37
5.2 Acoustic Transmittance of the Single Fishnet . . . 37
5.2.1 Simulated Transmittance . . . 37
5.2.2 Analytic Model of the Single Fishnet . . . 38
5.2.3 Experimental Transmittance . . . 39
5.3 Acoustic Transmittance of the Double Fishnet . . . 40
5.3.1 Simulated Transmittance . . . 42
5.3.2 Analytic Model of the Double Fishnet . . . 43
5.3.2.1 Even-order Modes . . . 43
5.3.2.2 Odd-order Modes . . . 43
5.3.2.3 Resonant Mode of the Gap . . . 45
5.3.3 Pressure Profiles of the Crossing Modes . . . 46
5.3.4 Experimental Transmittance . . . 48

5.4 Acoustic Transmittance of Double Fishnet with Unequal Thickness Plates 49
5.4.1 Simulated Transmittance . . . 50
5.4.2 Experimental Transmittance . . . 51
5.5 Concluding Remarks . . . 51

6 Controlling the Stop-band of the Double Fishnet Structure 53
6.1 Introduction . . . 53
6.2 Acoustic Transmittance of the Double Fishnet as a Function of Incident Angle . . . 53
6.2.1 Simulated Transmittance . . . 53
6.2.2 Experimental Study of the Effect of Incident Angle . . . 54
6.3 Effect of Misalignment on the Acoustic Stopband . . . 55
6.3.1 Simulated Transmittance . . . 55
6.3.2 Analytical Model of Effect of Misalignment . . . 55
6.3.3 Experimental Study of the Effect of Plate Misalignment . . . 58
6.3.3.1 Diagonal Misalignment . . . 59
6.3.3.2 Lateral Misalignment . . . 59
6.4 Effect of Gap Size on the Acoustic Stopband . . . 59
6.4.1 Analytic Modelling of the Effect of Gap Size . . . 61
6.4.1.1 Even-order Modes . . . 63
6.4.1.2 Odd-order Modes . . . 64
6.4.2 Experimental Study of the Effect of Gap Size . . . 66
6.5 Acoustic Triple Mode . . . 66
6.5.0.1 Experimental Evidence of the Triple Mode . . . 68
6.6 Concluding Remarks . . . 69

7 Acoustic Transmission of Structured Hole Arrays in Air 71
7.1 Introduction . . . 71
7.2 Helmholtz Double Fishnet Sample . . . 71
7.2.1 Simulated Transmittance of the Helmholtz Double Fishnet . . . 72
7.2.2 Analogy to the Helmholtz Resonator . . . 72
7.2.3 Analytic Model of the Helmholtz Double Fishnet . . . 73
7.2.4 Even-order modes . . . 74
7.2.5 Odd-order Modes . . . 74
7.3 Effect of the Gap Size on the Stop-band of the Helmholtz Double Fishnet 75
7.3.1 Simulated Transmittance as a Function of Gap Size . . . 75
7.3.2 Analytic Model as a Function of Gap Size . . . 76
7.3.2.1 Analysis of the Lowest Frequency Mode . . . 76

7.3.2.2 Splitting of the Fundamental Mode . . . 77
7.3.3 Experimental Study of Gap Size . . . 78
7.4 Concluding Remarks . . . 79

8 Acoustic Intromission at Near-Normal Incidence 81
8.1 Introduction . . . 81
8.2 Transmission Between Dissimilar Media . . . 81
8.2.1 Transmission Between Dissimilar Media at Normal Incidence . . . 81
8.2.2 Transmission Between Dissimilar Media at Oblique Incidence . . . 83
8.2.3 Angle of Acoustic Intromission . . . 85
8.2.3.1 Geometric Intromission . . . 85
8.3 Geometric Intromission within a Single Fluid . . . 87
8.4 Geometric Intromission with a Different Fluid Filling the Apertures . . . 90
8.5 Conclusions and Future Work . . . 92
8.6 Acknowledgement . . . 92

9 Resonant Acoustic Tunnelling through Acoustically Soft Waveguides 93
9.1 Introduction . . . 93
9.2 Acoustic Wave Guides . . . 94
9.3 Wave Tunnelling . . . 95
9.4 Samples and Modelling . . . 96
9.5 Acoustic Transmittance of a Single Slit in Polyurethane Foam . . . 97
9.5.1 Simulated Transmittance . . . 99
9.5.2 Experimental Transmittance . . . 99
9.6 Resonant Acoustic Tunnelling through Two Closely-Spaced Soft-walled Slits . . . 101
9.6.1 Simulated Transmittance . . . 101
9.6.2 Experimental Transmittance . . . 101
9.7 Concluding Remarks . . . 103

10 Acoustic Pseudo-Surface-Waves on Rigid Slit Arrays 107
10.1 Introduction . . . 107
10.2 Surface Acoustic Waves . . . 107
10.3 Simulated Dispersion of Structured Slits . . . 110
10.3.1 Pressure Field Profiles of Surface Modes . . . 113
10.4 Experimental Dispersion of Slitted Surfaces . . . 115
10.5 Concluding Remarks . . . 116

11 Conclusions and Future Work **119**
11.1 Introduction . . . 119
11.1.1 Summary of Thesis . . . 119
11.2 Future Work . . . 122
11.2.1 Broadening the Acoustic Stop Band of the Double Fishnet by Combining Multiple Fishnets . . . 122
11.2.2 Proposal for Experimental Demonstration of Acoustic Intromission at Normal Incidence . . . 123
11.2.3 Expansion of Studies into Resonant Acoustic Tunnelling . . . 124
11.2.4 Development of New Structures for the In-Plane Control of Pseudo Acoustic Surface Waves . . . 124
11.3 Publications . . . 126
11.4 Conferences . . . 127

Appendices **129**

A Single Fishnet Modal Matching Code **131**

B Double Fishnet Modal Matching Code **137**

References **147**

List of Figures

2.1 Wavefronts of a plane wave propagating in the z-direction with wave number k. 11

2.2 Schematic of a flanged Helmholtz resonator with cavity V, neck cross-section S and neck length L. 16

3.1 Schematic side view of the SF structure showing the different regions used in formulating the modal matching calculation of the structure's transmittance. 22

3.2 Schematic of the different domains and boundaries used in the FEM model of a single fishnet. The features are highlighted and named in each case. 26

4.1 Circuit diagram of the internally constructed microphone. 30

4.2 Schematic of the experimental arrangement for taking experimental transmission data in (a) xz-plane view and (b) yz-plane view. 31

4.3 Schematic of the experimental arrangement for taking reflection data. . 31

4.4 Schematic of the experimental arrangement for taking underwater data. 33

4.5 (a) Example of a detected pulse and (b) the example pulse after zero-buffering and windowing. 34

4.6 (a) FFT of detected reference signal and (b) FFT of buffered reference signal. 35

4.7 Frequency range of the airborne and underwater arrangements over which reasonable data can be acquired. 36

5.1 Schematic drawing of a single rigid plate perforated with a periodic square array of circular holes. Λ is the pitch of the hole array, d is the diameter of the holes and h_{p} is the thickness of the plate. 38

5.2 Transmission spectra through a single solid plate perforated with a square array of holes as a function of the plate thickness, h_p. The diameter of the holes is 2.4 mm and the pitch of the hole array is 8 mm. Dashed lines a, b and c correspond to the experimentally obtained data in figure 5.4. 39

5.3 Experimental transmission data (blue) of three difference thickness single fishnet structures compared with simulated data excluding the effects of thermo-viscous losses (red). In each system the hole diameter $d = 2.4$ mm and the pitch of the hole array $\Lambda = 8$ mm. 40

5.4 Experimental transmission data (blue) of three difference thickness single fishnet structures compared with simulated data including thermo-viscous losses (red). In each system the hole diameter $d = 2.4$ mm and the pitch of the hole array $\Lambda = 8$ mm. 41

5.5 Schematic drawing of the DF structure consisting of a pair of rigid plates perforated with a periodic square array of circular holes. 41

5.6 Transmission spectra of the DF structure as a function of the plate thickness h_p. Red indicates high transmission, blue indicates low transmission and black indicates less than -46 dB transmission. Dashed lines a, b and c correspond to the experimentally obtained data in figure 5.11. . . 42

5.7 Resonant frequencies of the DF as numerically determined by equations (5.2) and (5.13). Odd-order modes are shown as black lines and even-order modes are blue lines. 46

5.8 Transmission spectra of the DF structure as a function of the plate thickness h_p. Markers correspond to the instantaneous pressure profiles in figure 5.9. 47

5.9 Instantaneous pressure profiles along a line through the centre of the pipe at the marked positions in figure 5.6. The shape of the even-order mode remains essentially unchanged as the plate thickness varies, however the odd-order mode changes due to coupling into the gap. 48

5.10 Instantaneous pressure profiles along a line through the centre of the pipe for the two fundamental modes at $h_p = 5$ mm. 49

5.11 Experimental transmission data (blue) of three ADF structures compared with modelled data (red). In each system the gap size $h_g = 0.94$ mm, the hole diameter $d = 2.4$ mm and the pitch of the hole array $\Lambda = 8$ mm. 50

5.12 Modelled data of the transmission through the DF structure where the ratio of the plate thickness $h_{p1} : h_{p2}$ is (a) 1:2 and (b) 1:3. 51

5.13 Experimental data of the transmission through the DF structure for the cases of (a) $h_{p1} = 2.97$ mm, $h_{p2} = 5.94$ mm, (b) $h_{p1} = 2.97$ mm, $h_{p2} = 12$ mm and (c) $h_{p1} = 5.94$ mm, $h_2 = 12$ mm. 52

6.1 Schematic drawing of the DF structure consisting of a pair of rigid plates perforated with a periodic square array of circular holes. 54

6.2 (a) MM modelled dispersion of the DF with pitch $\Lambda = 8.00$ mm, plate thickness $h_p = 12.00$ mm and gap size $h_g = 0.94$ mm. (b) Experimentally determined dispersion of the DF out to 45° where the limited size of the sample prevented data being obtained at higher angles. 55

6.3 MM modelled transmission spectra of the DF structure as a function of the (a) diagonal and (b) lateral offset h_{off}. Black regions indicate less than −46 dB (0.05%) transmission. The pitch of the hole array $\Lambda = 8.00$ mm, the hole diameter $d = 2.40$ mm and the plate thickness $h_p = 12.00$ mm. 56

6.4 Transmission modes (solid lines) and acoustic stop-band (dashed lines) calculated from the analytical model, (a) diagonal offset and (b) lateral offset. 56

6.5 Time-averaged pressure profiles in an xy-plane through the centre of a gap $h_g = 0.94$ mm. The profiles are taken at the stop-band frequencies for offsets of h_{off} = (a) 0 mm, (b) 0.5 mm, (c) 1.0 mm, (d) 1.5 mm, (e) 2.0 mm and (f) 2.5 mm. 58

6.6 Experimental (blue lines) and modelled (red lines) transmission data for the DF structure diagonal offsets of h_{off} = (a) 0 mm, (b) 1.4 mm, (c) 2.8 mm, (d) 4.2 mm, (e) 5.6 mm. 60

6.7 Experimental (blue lines) and modelled (blue lines) transmission data for the DF structure lateral offsets of h_{off} = (a) 0 mm, (b) 1 mm, (c) 2 mm, (d) 3 mm, (e) 4 mm and (f) 1.7 mm. 61

6.8 MM modelled transmission spectra of the DF structure as a function of the gap size h_g. Black indicates less than −46 dB transmission, red represents high transmission. The pitch of the hole array is $\Lambda = 8$ mm, the hole diameter is $d = 2.4$ mm and the plate thickness is $h_p = 12$ mm. The dashed white lines labelled a-e correspond to the experimental data in figure 6.12 62

6.9 Schematic diagram of the pipe geometry used to analyse the transmittance of the DF at large values of h_g. 63

6.10 (a)Repeat of figure 6.8 to facilitate comparison. (b) Combined plot of the transmission modes (solid lines) and acoustic stop-band (dashed lines) calculated from the three analytical models. 65

6.11 Time-averaged pressure field at the frequency of the acoustic stop-band on a plane through the centre of the unit cell. 65

6.12 Experimental (blue line) and FEM modelled (red line) transmission data for the DF structure at gap sizes h_g = (a) 0.94 mm, (b) 1.88 mm, (c) 2.82 m and (d) 3.76 mm. 67

6.13 MM modelled transmission spectra of the DF structure as a function of the gap size h_g. (a) Plate thickness h_p = 12 mm, hole diameter d = 2.4 mm and pitch Λ = 8 mm. (b) Plate thickness h_p = 12 mm, hole diameter d = 0.45 mm and pitch Λ = 3 mm. 67

6.14 Analytic prediction of the instantaneous pressure field for each of the three resonances seen around f = 25 kHz for a gap size h_g = 6.8 mm. . 68

6.15 Experimental (blue lines) and simulated (red lines) transmission data of the the DF structure at gap sizes (a) 4.8 mm and (b) 6.8 mm. 69

7.1 Schematic of the HDF structure with plate thickness h_p and gap size h_g. The HDF has a hole array with pitch Λ and a hole diameter d. Rectangular grooves of depth h_m milled into one face of each plate give a total cavity height of $h_H = 2h_m + h_g$. (a) A yz-plane view of the unit cell centred on one of the holes. (b) An xy-plane view of the unit cell within the gap showing the hole enclosed by an island with side l. . . . 72

7.2 Comparison between a DF (red line) where Λ = 8.00 mm, h_p = 5.94 mm, d = 2.40 mm and h_g = 0.94 mm and an equivalent HDF (blue line) where h_m = 3.00 mm and l = 4.00 mm. 73

7.3 (a)Modal matching method modelling of the transmission spectra of the HDF sample as a function of the gap size h_g. The black region corresponds to the stop-band, defined as less than −46 dB (0.05%) transmission. (b) Pipe mode frequencies (blue lines) and stop-band frequency (red line) calculated from the analytic treatment of the HDF. 75

7.4 Time-averaged pressure profiles in a central xz-plane through the HDF structure. Profiles show the 2nd mode, the upper branch of the split fundamental and the lower branch of the split fundamental at gap sizes h_g = 0.2mm and h_g = 1.4 mm. The out-of-plane line corresponds to the instantaneous pressure of the mode at the phase angle of maximum amplitude. 78

7.5 Experimental (blue line) and modelled (red line) data for the HDF structure with gap sizes of $h_g = 0.47$ mm, 0.94 mm and 1.41 mm respectively. 80

8.1 Transmission and reflection of a plane wave incident normal to the interface between two media with different specific impedances. 82

8.2 Transmission and reflection of a plane wave incident at an oblique angle to a planar interface between two media with different acoustic impedances. 83

8.3 Figures taken from Holland [1] showing (a) Theoretical reflection loss for a seabed whose sound speed is smaller than that of water. Sound speed and density ratios are 0.9822 and 1.2174. respectively and (b) Bottom reflection loss from first sediment layer on the Malta Plain. The salient feature is the peak at 75° degrees from normal, corresponding to the angle of intromission. 86

8.4 Experimental and FEM model data showing the broadband transmission of TE radiation through a 1D metallic grating, taken from Aközbek *et al.* [2] 87

8.5 Schematic drawing of a single rigid plate perforated with a periodic square array of circular holes. Λ is the pitch of the hole array, d is the diameter of the holes and h_p is the thickness of the plate. 88

8.6 Schematic side view of the SF structure showing the different regions used in formulating the modal matching calculation of the structure's transmittance. 88

8.7 MM modelling of the transmittance of a SF with an aperture area ratio of 0.2 at normal incidence (black line) and at the angle of intromission, $\theta_I = 78.46°$ (blue line). 89

8.8 (a) MM modelling of the normal incidence transmittance of a SF in water, with air filling the holes and an aperture area ratio of $0.0002\dot{3}$. (b) Data in (a) re-plotted against the wavelength in water 91

8.9 Modal matching modelling of the normal incidence transmittance of a SF in water, with silicon oil (Dow 200, 1 centistoke) filling the holes and an aperture area ratio of 0.53. 92

9.1 Schematic diagram of (a) single foam slit and (b) double foam slit. . . . 95

9.2 Schematic showing a wave incident with energy E upon a double barrier system. At energies $E_1, 2, 3$ corresponding to the energy levels of the double barrier the incident wave is completely transmitted. 96

9.3 Acoustic transmittance through a 10 mm thick plate of PU foam. 98

9.4 System used to model the transmission through foam slits. Perfectly matched layers are shaded blue, soft boundaries are highlighted in green, the acoustic wave is launched from the orange shaded region and the transmittance is determined by integration of the time-averaged pressure field along the red line. 98
9.5 FEM simulated transmittance through a single slit with various thickness plates of PU foam. 100
9.6 Acoustic transmittance through a 4 mm wide slit in a (a) 2 mm and (b) 5 mm thick polyurethane foam plate. 100
9.7 Simulated FEM transmittance through a pair of foam plates with a slit each plate, aligned with each other. The plate thickness is $h_p = 10$ mm and the plate separation h_g is varied from 4 mm to 7 mm. 102
9.8 Experimental transmittance through a $w = 4$ mm wide slit in a pair of $h_p = 2$ mm thick polyurethane foam plates which are separated by a $h_g = 4.8$ mm gap (blue line). FEM modelling of the transmittance of the structure (red line). 102
9.9 Experimental transmittance through a $w = 4$ mm wide slit in a pair of $h_p = 2$ mm thick polyurethane foam plates that are separated by an assumed $h_g = 4.8$ mm gap. FEM modelling of the transmittance with a modified gap of $h_g = 4.2$ mm (red line). 103
9.10 Schematic diagram of sample in frame whilst (a) uncompressed and (b) compressed. 104

10.1 Depictions of the surface motion associated with (a) Rayleigh waves and (b) Love waves. Images obtained from the Wikimedia Commons. 109
10.2 Geometry of the surfaces used in the surface wave experiments, (a) solid plate with array of slits milled into the the surface and (b) with the addition of a long pitch grating. 110
10.3 (a) FEM prediction of the dispersion of the slitted surface and (b) simulated reflectance of the structure at normal incidence. (c) FEM determined dispersion plot of 200 µm slit sample after the addition of a 12 mm pitch grating and (d) simulated reflectance of the structure at normal incidence. 111
10.4 FEM simulation of the band structure of the slitted surface with (red lines) and without (blue lines) the addition of a 3Λ grating. Solid black lines correspond to the sound line and first diffracted sound line associated with Λ. Dashed black lines correspond to the additional diffracted sound lines associated with the 3Λ grating. 113

10.5 (a) FEM predicted dispersion of the $d = 850$ µm slit sample and (b) simulated reflectance of the structure at normal incidence. (c) Dispersion plot of the sample after the addition of a 12 mm pitch grating and (d) simulated reflectance of the structure at $\theta_{inc} = 0°$ and $\theta_{inc} = 10°$. 114
10.6 (a) Instantaneous pressure profile of lower branch of the APSW at normal incidence. (b) Instantaneous pressure profile of upper branch of the APSW at normal incidence. 114
10.7 Dispersion plots of the samples. (a) $w = 200$ µm, $h_d = 2.97$ mm and $\Lambda = 4$ mm, and (a) $w = 850$ µm, $h_d = 2.65$ mm and $\Lambda = 4$ mm. 115
10.8 Modified geometry of the surface with rods raised vertically above the surface by a height, h_r. 116
10.9 Experimental (blue points) and modified simulated data (red line) for the dispersion of the APSW on the $w = 850$ µm sample. 117

11.1 (a) Modelled data of the transmission through a single fishnet with plate thickness $h_p = 12$ mm, a double fishnet with plate thickness $h_p = 5.94$ mm plates and a quadruple fishnet with plate thickness $h_p = 2.97$ mm. Where relevant, the gap size $h_g = 0.94$ mm. (b) Modelled data of the transmission through a QF with plate thickness $h_p = 2.97$ mm for (a) $h_{g1,2,3} = 0.94$ mm, (b) $h_{g1} = 0.47$ mm, $h_{g2} = 0.94$ mm, $h_{g3} = 1.41$ mm and (c) $h_{g1} = 0.47$ mm, $h_{g2} = 1.41$ mm, $h_{g3} = 1.88$ mm. 123
11.2 Schematic diagram of the square array of holes with pitch Λ, hole diameter d and hole depth h_d. 125
11.3 Mode speed of the APSW supported on a square array of closed-ended holes. The pitch of the hole array $\Lambda = 4$ mm, the diameter of the holes $d = 1$ mm and the hole depth h_d is varied from 3-6.5 mm in increments of 0.5 mm, corresponding to lines A-H respectively. 126

A.1 Schematic side view of the SF structure showing the different regions used in formulating the modal matching calculation of the structure's transmittance. 132

B.1 Schematic side view of the DF structure showing the different regions used in formulating the modal matching calculation of the transmittance. 138

It's all noise

Chapter 1

Introduction

Throughout history there has been considerable effort placed in explaining the world around us. One particular area of interest is how sound interacts with the environment. An echo is an acoustic phenomenon whereby a sound is reflected from the surrounding environment and detected a number of times. Before the physical origins of the echo were understood the Greeks provided a fairytale explanation. The story of Echo tells us of a wood nymph who loved the sound of her own voice. One day, Echo betrayed the goddess Juno by enabling the escape of Juno's adulterous husband. In revenge, Juno cursed Echo to never speak again. The sole exception being that she could respond in kind with the words spoken to her [3].

Other interesting phenomena related to the interaction of sound with the structure have been exploited to great effect. The Hellenistic theater of Epidaurus in Greece, is one such example renowned for its remarkable acoustic properties. A speaker stood at the centre of the stage can be heard with little apparent loss of intensity all the way to the outer seats. Whether intentional or coincidental, the structure of the seating acts as an acoustic filter that allows sound to travel from the center of the stage whilst removing the background noise of the open air environment [4]. On the other side of the world, the staircase of El Castillo at Chichen Itza possesses two notable acoustic phenomena associated with its structure. A handclap from the base of the staircase produces a reflection that sounds remarkably similar to the call of the Quetzal bird [5]; considered divine by the Mayans, the Quetzal bird was associated with the snake deity *Quetzalcoatl*. The staircase also exhibits a diffraction phenomenon leading an observer at one end of the staircase to hear the sound of raindrops falling into water when people climb the other end of the staircase [5, 6]. Within Chichen Itza lies the Sacred Cenote (a well), a tribute to the rain god Chaak, making the sound of raindrops all the more intriguing.

Periodically structured surfaces, such as the Chichen Itza staircase or an array of

slits, also support a form of surface acoustic wave (SAW), labelled here as an acoustic pseudo-surface-wave (APSW). SAWs are acoustic waves that are confined at a surface; their fields decay exponentially away from the surface - a feature known as evanescence. There are two forms of SAW: Rayleigh provided the description of SAWs with particle oscillations normal to the interface, specifically at a solid-vacuum interface [7]; Love provided the description of SAWs with particle oscillations parallel to the interface and perpendicular to the direction of propagation [8]. Similar waves to the Rayleigh-type SAW arise under different conditions: Lamb waves are guided within a solid plate [9] rather than at a single interface and are exploited extensively in non-destructive testing. Stoneley waves exist at the interface between two solids [10] and Scholte waves exist at the interface between a fluid and an elastic solid [11]. Scholte waves commonly occur in boreholes and can be used to determine material properties of the borehole walls [12].

An APSW exists at the interface between a fluid and a rigid, periodically structured surface and has been labelled with the 'pseudo' prefix due to the form of the fields. While the fields of the APSW decay exponentially into the fluid medium, the fields that are allowed to penetrate beneath the surface (i.e., the fields within the slits on a periodic slit array) do not have the exponential decay associated with SAWs. It is perhaps more appropriate to describe them as waves guided by the surface. Previously, APSWs have been shown to be supported on rectangular-groove gratings [13], a honeycomb structure [14] and doubly periodic square gratings [15]. A graphene-like (hexagonal) arrangement of holes was recently shown to support a APSW that exhibits a band structure somewhat analogous to that of electrons in graphene [16].

Similar work has been undertaken electromagnetically, originating from Pendry's proposed structure to support a surface wave that would mimic surface plasmons [17]. The proposed structure consisted of a periodic square array of infinitely deep, square waveguides. The surface of the structure supports a dispersive wave with an asymptote at the resonance of the holes; for the infinitely deep waveguide, this corresponds to the cut-off frequency. The fields of the wave decay exponentially both above and below the surface. Hibbins *et al* subsequently verified the existence of such waves on an array of terminated waveguides [18], which additionally support a family of modes that asymptote towards each of the resonant modes of the waveguide [19]. The fields of the higher order surface waves no longer exhibit exponentially decaying fields into the structured surface; the fields now correspond to the resonant modes of the surface structure. Advancing the design of structured surfaces from a simple periodic feature to a provide control over the propagation of surface waves is of considerable interest. By varying the speed at which surface waves propagate over difference parts of the surface it should be possible to create surface wave 'black holes' (a surface that traps an incident wave in an infinite spiral) , surface wave lenses and other novel structures.

A step towards the formation of a surface wave black hole has been taken with the experimental realisation of a Luneburg lens [20] for microwave surface waves [21]. The range of surface wave velocities available on the Luneburg lens surface was insufficient to achieve the black hole design. Acoustically, if full control over SAWs is achieved it might one day be possible to shield buildings from the destructive force of earthquakes [22], in fact an experimental cloak has already been developed showing promise [23]. Another use of structured surfaces is in collimating and focusing a wave transmitted through a single aperture surrounded by a series of grooves [24, 25].

The discovery of extraordinary optical transmission (EOT) by Ebbesen [26, 27], often defined as a resonant mechanism that facilitates a transmitted intensity greater than that predicted by classical aperture theory [28], has generated increased interest in the transmission properties of periodic arrays of sub-wavelength holes and slits. The similarity between the governing equations of electromagnetism and acoustics has stimulated comparable work with sound waves. Enhanced transmission has been reported acoustically for solid bodies structured with periodic arrays of holes or slits [29–32]. Unlike the electromagnetic case for periodic holes in a metal plate, holes in an acoustically rigid wall do not possess a cut-off frequency preventing the propagation of plane-waves and so enhanced transmission of sound through arrays of holes in a rigid plate is typically associated with the excitation of Fabry-Pérot-like resonances in the pipes [33]. Conversely, sound screening by rigid plates, perforated with periodic arrays of holes has been demonstrated [34]. The sound screening corresponding to the Wood's anomaly at the frequency where the wavelength corresponds to the double periodicity of the hole array. More recently, the response of two perforated plates separated by a small gap has been explored. The resonant mode of the gap, defined by the pitch of the hole array, is the origin of a band of near-perfect acoustic attenuation [35, 36]. A recent experimental study of this structure confirmed the existence of the stop band [37]. Other work has proposed perforated plates as a method of achieving sub-wavelength imaging [38] and recently a structure formed from perforated plates was experimentally demonstrated as an acoustic ground cloak [39, 40]. A ground cloak disguises the wave scattered from a ground based object and makes it appear as if the object is not there.

In addition to the resonant transmission methods mentioned above, which are inherently narrowband and lossy, there is another path to enhanced transmission. The Brewster angle is a well known electromagnetic phenomenon whereby transverse magnetic radiation incident upon a surface is transmitted without reflection. A similar effect, known as intromission, exists acoustically at the interface between two media with suitable material properties [41]. Both phenomena are due to impedance matching across a boundary. An analogous situation was recently explored in both regimes where the impedance matching is achieved through geometry rather than material properties

[42–45].

Structured materials have been shown to exercise control over acoustic waves in other ways. Omni-directional acoustic absorbers have been demonstrated by by designing a shell that refracts incident sound towards an absorbing core [46, 47]. The graded impedance is achieved through a number of layers consisting of porous cylinders where the fill fraction is varied from layer to layer. Other structures built from a unit cell of coiled up space have been numerically shown to demonstrate negative refraction and acoustic tunnelling [48]. A precursor to this is the work on path length refraction undertaken by Kock and Harvey [49]. A number of structures were developed using structure to offer control over the propagation properties of sound. More recently, a structure demonstrating negative refraction was realised experimentally [50].

The work presented in this thesis furthers the investigation into the interaction of sound with a number of structured systems. A considerable portion is devoted to the study of the double fishnet, which shows promise as a route to creating sound blocking windows that allow air to flow through them whilst preventing the transmission of sound. Such structures may find use in silencing machinery where air flow is required for cooling or in offices where opening windows allows external noise can be distracting. The latter chapters take a look at some unusual properties of structured surfaces that allow us to demonstrate acoustic intromission at normal incidence and resonant acoustic tunnelling. Finally, we transfer and develop an experimental method for the detection of surface waves from the electromagnetic to acoustic regimes as part of a preliminary study into APSWs.

1.1 Outline of Thesis

Chapter 2 presents an overview of work relevant to the material presented in this thesis. First the acoustic wave equation is described. Definitions of the acoustic impedance and geometric impedance are provided. The conditions leading to resonance in open-ended pipes and pipes terminated at one end are detailed. The conditions leading to the Helmholtz resonance are provided. A brief discussion of the effect of viscous losses in confined regions is had. Finally, Floquet's theory is provided.

Chapter 3 describes the various modelling techniques used to predict the responses of the studied systems. Three different methods are employed throughout this thesis. Simulations and understanding are provided by analytical analysis of highly simplified systems, the method of modal matching and finite element method modelling.

Chapter 4 describes the experimental arrangements used to measure the response of the studied structures. Details of the airborne transmission and reflection arrangements and the underwater transmission arrangement are provided. The methods employed to

obtain and analyse data are also provided.

Chapter 5 is concerned with the airborne transmission of sound through rigid plates which have been perforated with a periodic square array of holes. The experiment is then extended by considering the transmission of two identical plates that are stacked together and separated by a small gap. Varying the angle of incidence upon the stacked plates is examined. Finally, the thickness of one of the plates is varied to observe the effect of commensurate thickness plates.

Chapter 6 extends the work in the previous chapter by exploring the effects of misaligning the plates with respect to each other and of varying the gap between the two plates.

Chapter 7 further extends the work in the previous two chapters by looking at the effect of structuring the 'gap-side' of each plate.

Chapter 8 investigates the acoustic transmission through a a single rigid plate perforated with a square array of holes at the angle of geometric intromission. This work is extended by considering the effect changing the incident/transmission medium and the medium within the holes has upon the angle of intromission.

Chapter 9 considers the transmission of sound through a single acoustically soft slit. Combining two slits together and separating them by a small gap allows demonstration of resonant acoustic tunnelling.

Chapter 10 deals with the reflection of sound incident upon a patterned surface. It is well established that sound can propagate along the interface of structured surfaces and here we measure the dispersion over three distinct geometries. In the case of this thesis, the media are air and a structured surface consisting of a periodic array of closed ended slits.

Chapter 11 summarises the work presented in this thesis and provides an outlook on potential extensions to the work.

Appendix A provides a derivation of the modal-matching analysis used to simulate data for the work presented in chapters 5 and 8.

Appendix B provides a derivation of the modal-matching analysis used to simulate data for the work presented in chapters 5 and 6.

Chapter 2

Background

2.1 Introduction

The work in this thesis is broadly concerned with the transmittance and reflectance of structured plates/surfaces. This chapter provides a background on the physics used to understand the observations that are made. Section 2.2 provides a reduced derivation of the acoustic wave equation. Section 2.3 introduces the concept of acoustic impedance that defines one of the major acoustic material properties. Section 2.4 discusses the interaction of sound with both closed-ended and open-ended pipes, and Helmholtz resonators. Section 2.5 provides an overview of the losses associated with the thermal and viscous properties of fluids. Further background specific to the content of the chapters is provided within the relevant chapters.

2.1.1 Common Notation

$\vec{r} =$ *equilibrium position* of a fluid element

$$\vec{r} = x\hat{x} + y\hat{y} + z\hat{z}$$

$\vec{u} =$ *particle velocity* of a fluid element

$$\vec{u} = u_x\hat{x} + u_y\hat{y} + u_z\hat{z}$$

$\rho_0 =$ *equilibrium density* at (x, y, z)
$\rho =$ *instantaneous density* at (x, y, z)
$s =$ *condensation* at (x, y, z)

$$s = \frac{\rho - \rho_0}{\rho_0}$$

P_0 = *equilibrium pressure* at (x, y, z)
P = *instantaneous pressure* at (x, y, z)
p = *acoustic pressure* at (x, y, z)

$$p = P - P_0$$

K = *adiabatic bulk modulus* of the fluid
c = *thermodynamic speed of sound* of the fluid

2.2 The Acoustic Wave Equation

To understand the structures investigated in this thesis we first need a description of how sound propagates in fluids. As the structures are considered to be perfectly rigid objects, the theory does not require consideration of the vibrational and flexural propagation within solids. Taking a fluid medium at equilibrium, we consider what happens if an element of the fluid is rapidly moved from one point to another. With the motion, the fluid in front of the element is compressed while the fluid behind the element undergoes rarefaction, leading to local changes in the pressure and density of the medium. The local changes in pressure act on the surrounding medium to provide the restoring forces responsible for propagating a wave through the medium. To describe this behaviour we need to describe the displacement of the element within the fluid as a function of time, how the density of the element changes as it is displaced, and how the pressure of the element changes. Thus three statements are required to describe the propagation of sound waves in a medium [41].

1. Motion of the element leads to a change in the density of the element.
2. A corresponding change in pressure occurs due to the changing density.
3. Inequalities in the pressure cause further motion of the element.

2.2.1 The Continuity Equation

Regarding the first statement, which states that a rapid movement of an element causes a change in the density. We require a relationship between the particle motion, which we will describe with the velocity $\vec{u}$, and the instantaneous density ρ at each point within the fluid. Consider a small element that is large enough to contain a large number of particles and hence can be considered as a continuous medium, yet small enough that the acoustic properties of the medium are uniform. As the element experiences a local

change in pressure due to the propagating acoustic wave, the relationship between $\vec{u}$ and ρ can be expressed as 'the rate at which the density increases must equate with the net influx of mass flowing into the element' [41].

$$\frac{\partial \rho}{\partial t} + \nabla \cdot (\rho \vec{u}) = 0. \tag{2.1}$$

This equation is exact, however in the limit that the equilibrium density ρ_0 is approximately constant with time, equation (2.1) can be recast into the linear continuity equation by substituting $\rho = \rho_0 (1 + s)$.

$$\rho_0 \frac{\partial s}{\partial t} + \nabla \cdot (\rho_0 \vec{u}) = 0. \tag{2.2}$$

2.2.2 The Equation of State

The second statement says that a change in density causes a corresponding change in the local pressure. The equation of state must relates three physical properties of the medium, ρ, K, and P, and will describe the thermodynamic behaviour of the medium. In the context of this thesis, we can consider the acoustic processes to be isentropic (adiabatic and reversible) due to the relatively small changes in pressure and density which are experienced. The relationship between the pressure and the density of the fluid medium can be described by

$$P = P_0 + \left(\frac{\partial P}{\partial \rho}\right)_{\rho_0} (\rho - \rho_0) + \frac{1}{2}\left(\frac{\partial^2 P}{\partial \rho^2}\right)_{\rho_0} (\rho - \rho_0)^2 + \cdots, \tag{2.3}$$

where the partial derivatives are determined for the isentropic compression and rarefaction of the fluid about the equilibrium density. In the limit of small amplitude fluctuations only the lowest order term needs to be retained, giving a linear relationship between the pressure and the change in density.

$$P - P_0 \approx K \frac{(\rho - \rho_0)}{\rho_0}, \tag{2.4}$$

where $K = \rho_0 \left(\frac{\partial P}{\partial \rho}\right)_{\rho_0}$. This can be rewritten in a simpler form,

$$p = Ks. \tag{2.5}$$

2.2.3 The Force Equation

Finally we examine the third statement, which states that pressure inequalities within the medium result in forces that act upon on a fluid element. Consider an element

of the fluid with volume $dV = dx\,dy\,dz$ and containing a mass dm. The forces the element experiences due to the local changes in pressure will accelerate the element, satisfying Newton's second law $d\vec{f} = \vec{a}\,dm$. In the absence of viscous effects (the inclusion of viscous effects will be discussed in section 2.5), the net force experienced by the element is given by

$$d\vec{F} = -\nabla P dV. \tag{2.6}$$

Additionally the force due to gravitational attraction acts upon the elements, however the additional term can be considered negligible due to the small amplitude oscillations encountered. The expression for the acceleration of the fluid element is complicated by the particle velocity $\vec{u}$ being a function of both time and space. An approximate solution can be obtained from the Taylor expansion of a fluid element with particle velocity $\vec{u}(x, y, z, t)$ which moves to a new location $\vec{r}(x + dx, y + dy, z + dz, t + dt)$:

$$\begin{aligned}\vec{u}(x + u_x dt, y + u_y dy, z + u_z dt, t + dt) \\ = \vec{u}(x, y, z, t) + \frac{\partial \vec{u}}{\partial x} u_x dt + \frac{\partial \vec{u}}{\partial y} u_y dt + \frac{\partial \vec{u}}{\partial z} u_z dt + \frac{\partial \vec{u}}{\partial t} dt,\end{aligned} \tag{2.7}$$

from which the acceleration in the limit of $dt \to 0$ becomes

$$\vec{a} = \frac{\partial \vec{u}}{\partial t} + (\vec{u} \cdot \nabla)\vec{u}. \tag{2.8}$$

The mass of the element $dm = \rho dV$ can be substituted into Newton's second law to give

$$-\nabla P = \rho \left(\frac{\partial \vec{u}}{\partial t} + (\vec{u} \cdot \nabla)\vec{u} \right). \tag{2.9}$$

In the limit of small amplitude oscillations, where $|(\vec{u} \cdot \nabla)\vec{u}| \ll |\partial \vec{u}/\partial t|$ this reduces to the mass continuity equation

$$-\nabla P = \rho_0 \frac{\partial \vec{u}}{\partial t}. \tag{2.10}$$

2.2.4 The Linear Wave Equation

An equation involving a single variable p is arrived at by combining equations 2.2,2.4 and 2.10.

$$\nabla^2 p = \frac{1}{c^2} \frac{\partial^2 p}{\partial t^2}. \tag{2.11}$$

The linear wave equation is applicable for the propagation of sound in fluids that can be considered lossless.

Euler is credited with providing the general form of the continuity equations from which a description of the propagation of sound was obtained: the conservation of

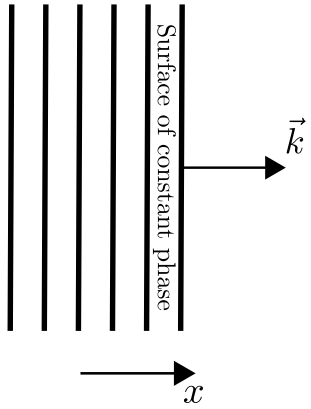

Figure 2.1: Wavefronts of a plane wave propagating in the z-direction with wave number k.

mass (equation 2.1), for the case of inviscid flow, and the conservation of momentum (equation 2.9) [51, 52]. The equations correspond to the Navier-Stokes equations, which provide a full description of the propagation of fluids, in the limit of zero viscosity and no heat conduction. For acoustic propagation through confined regions, the viscous and heat conduction terms can no longer be ignored and the Navier-Stokes equations are required to determine the acoustic propagation (see section 2.5).

2.2.5 Harmonic Plane Waves

A plane wave propagates in a single direction with constant phase and amplitude at any point in a plane perpendicular to the direction of propagation. If the plane wave is propagating in the z-direction (see figure 2.1), the linear wave equation (2.11) simplifies to

$$\frac{\partial^2 p}{\partial z^2} = \frac{1}{c^2}\frac{\partial^2 p}{\partial t^2}. \tag{2.12}$$

The solution of which is a wave with the form

$$p = \mathbf{A}\exp\left[i\left(\omega t - kz\right)\right] + \mathbf{B}\exp\left[i\left(\omega t + kz\right)\right], \tag{2.13}$$

where $\mathbf{A}$ and $\mathbf{B}$ are amplitude coefficients and the corresponding particle velocity is obtained from equation (2.10).

$$\vec{u} = \frac{\mathbf{A}}{\rho_0 c}\exp\left[i\left(\omega t - kz\right)\right]\hat{z} - \frac{\mathbf{B}}{\rho_0 c}\exp\left[i\left(\omega t + kz\right)\right]\hat{z}, \tag{2.14}$$

where the negative and positive k components within the exponentials correspond to the forward and backward propagating waves respectively. Equations 2.13 and 2.14

allow the acoustic response of the structures studied in this thesis to be determined (section 3).

2.3 Impedance

The acoustic impedance is a characteristic property of a medium that relates the acoustic pressure and the particle velocity of an acoustic wave propagating within the medium.

$$\mathrm{z} = \frac{p}{u}, \tag{2.15}$$

which for an acoustic plane wave at normal incidence simplifies to

$$\mathrm{z} = \rho_0 c. \tag{2.16}$$

The mismatch in impedances between two media can be used to determine the transmission and reflection of a wave across the interface. The Rayleigh transmission [equation (2.17)] and reflection [equation (2.18)] amplitude coefficients determine the ratio of the amplitude of the transmitted and reflected waves from the impedance of the two media. The transmission and reflection amplitude coefficients of a normally incident plane wave from medium 1 to medium 2 are given by [41],

$$t = \frac{2\mathrm{z}_2}{\mathrm{z}_2 + \mathrm{z}_1}, \tag{2.17}$$

$$r = \frac{\mathrm{z}_2 - \mathrm{z}_1}{\mathrm{z}_2 + \mathrm{z}_1}, \tag{2.18}$$

where the subscripts denote each of the two media. Whether the sound is propagating from a high impedance medium to a low impedance medium or vice versa dictates the boundary condition encountered by an incident wave. Acoustically hard media are characterised by a high impedance relative to the incident medium while soft media have a low relative impedance. A wave incident upon an infinite impedance medium is presented with a perfectly rigid boundary and will exhibit a velocity node at the interface; the reflected wave will be π out of phase with the incident wave. A wave incident upon a zero impedance medium is presented with a perfectly soft boundary and will exhibit a pressure node at the interface; the reflected wave will be in phase with the incident wave. These perfect boundaries are never encountered but they make reasonable approximations in the right situation and are far simpler to work with.

2.3.1 Geometric Acoustic Impedance

Taken alone, the acoustic impedance of a medium for a plane wave [equation (2.16)] suggests that a plane wave propagating along a pipe will continue to propagate with no reflection when a change in cross-section is encountered. The geometric acoustic impedance, Z, takes into account changes in geometry, and is given by the ratio of the acoustic pressure to the volume velocity, U.

$$\mathrm{Z} = \frac{p}{U}, \tag{2.19}$$

where $U = uS$ and S is the cross-sectional area of the structure. Hence, Z relates to z through the relation

$$\mathrm{Z} = \frac{\mathrm{z}}{S}, \tag{2.20}$$

from which it can be inferred that a rapid change in geometry (compared to the wavelength) will cause a reflection because the wavefunction describing the mode has changed. The geometric acoustic impedance is critical to the work presented in chapter 8 where we look at angle of acoustic intromission.

2.4 Pipe Acoustics

The structures investigated in chapters 5, 6, 7 and 10 can be analysed by approximating them to various arrangements of pipes or slits, either open-ended or terminated. In doing so, the assumption is made that the surrounding materials are perfectly hard and hence no sound propagates within the surrounding material. The properties of pipes depend greatly on the the geometry of the pipe and the size compared to the wavelength of the incident sound. In keeping with the design of the structures investigated, the pipes will be assumed to have a constant cross-section, which is small enough such that the only allowed propagating mode is a plane wave, yet sufficiently large that viscous effects can be considered to be negligible (see section 2.5).

Consider a straight pipe with length h_p and cross-sectional area A with its axis in the z-direction. The entrance to the pipe sits at $z = 0$ and is terminated at $z = h_\mathrm{p}$. An acoustic wave with planar wave fronts is normally incident on the pipe. Assuming plane wave propagation within the pipe the wave will take the form

$$p = \mathbf{A}\exp\left[i\left(\omega t + k(h_\mathrm{p} - z)\right)\right] + \mathbf{B}\exp\left[i\left(\omega t - k(h_\mathrm{p} - z)\right)\right], \tag{2.21}$$

where $\mathbf{A}$ and $\mathbf{B}$ are amplitude coefficients determined by the boundary conditions at $z = 0$ and $z = h_\mathrm{p}$. Across the boundaries, both the pressure and particle velocity must

be continuous. Thus the acoustic impedance at $z = 0$ and $z = h_\mathrm{p}$ are obtained by combining equations (2.13) and (2.14). At $z = 0$,

$$\mathrm{Z}_0 = \rho_0 c \frac{\mathbf{A}\exp\left[ikh_\mathrm{p}\right] + \mathbf{B}\exp\left[-ikh_\mathrm{p}\right]}{\mathbf{A}\exp\left[ikh_\mathrm{p}\right] - \mathbf{B}\exp\left[-ikh_\mathrm{p}\right]}. \tag{2.22}$$

At $z = h_\mathrm{p}$,

$$\mathrm{Z}_{h_\mathrm{p}} = \rho_0 c \frac{\mathbf{A} + \mathbf{B}}{\mathbf{A} - \mathbf{B}}. \tag{2.23}$$

The two equations can then be combined to eliminate $\mathbf{A}$ and $\mathbf{B}$.

$$\frac{\mathrm{Z}_0}{\rho_0 c} = \frac{\left(\frac{\mathrm{Z}_{h_\mathrm{p}}}{\rho_0 c}\right) + i\tan\left(kh_\mathrm{p}\right)}{1 + i\left(\frac{\mathrm{Z}_{h_\mathrm{p}}}{\rho_0 c}\right)\tan\left(kh_\mathrm{p}\right)}. \tag{2.24}$$

2.4.1 Pipes Terminated by a Single Closed End

Consider a pipe which is open at $z = 0$ and terminated by a rigid boundary at $z = h_\mathrm{p}$. The equivalent scenario can be found by letting $\mathrm{Z}_{h_\mathrm{p}}$ tend to infinity. The resulting equation is

$$\frac{\mathrm{Z}_0}{\rho_0 c} = -i\cot\left(kh_\mathrm{p}\right). \tag{2.25}$$

The resonances of the system occur when the input impedance, Z_0, is a minimum, i.e., when $\cot\left(kh_\mathrm{p}\right) = 0$, giving

$$k_n h_\mathrm{p} = \frac{(2n-1)\,\pi}{2}, \tag{2.26}$$

where n is a positive integer and for which the resonant frequencies are given by

$$f_n = \frac{(2n-1)\,c}{4h_\mathrm{p}}. \tag{2.27}$$

The lowest order mode corresponds to the condition that a quarter wavelength fits into the length of the pipe. Higher order modes are then found by fitting in an additional half wavelength.

2.4.2 Pipes Terminated by an Open End

Consider a pipe terminated by an open end. Under the simplifying assumption that the radiation impedance looking out the pipe is zero, a relationship between k_n and h_p is obtained in a similar manner to that of the closed-ended pipe.

$$n\pi = k_n h_\mathrm{p}, \tag{2.28}$$

for which the resonance frequencies are therefore

$$f_n = \frac{nc}{2h_\mathrm{p}}. \tag{2.29}$$

In reality the pipe length, h_p, requires a correction due to radiation impedance looking out of the pipe being finite. The radiation impedance of the open end can be obtained by treating the open-end of the pipe as a baffled piston. A brief description follows of how the radiation impedance of a baffled circular piston is calculated. Consider a circular piston of radius a and surface area S, which is oscillating with velocity $u = U_0 \exp(i\omega t)$. The motion of a small element of the piston with area dS produces an incremental pressure dp at some other element of area dS'. The total pressure can then be determined by integrating the incremental pressure over the surface of the piston [41].

For a flanged pipe, the correction is approximately equivalent to

$$h'_\mathrm{p} = h_\mathrm{p} + 0.85a, \tag{2.30}$$

where a is the radius of the pipe and the correction is applied to both open ends giving a total end-correction of approximately $1.7a$. The end-correction arises from the treatment the opening of the pipe as a baffled piston in the low frequency limit, $ka << 1$ [41].

2.4.3 The Helmholtz Resonator

The Helmholtz resonator [53] consists of a rigid walled cavity of volume, V, with a neck of area, S, and length, L, (figure 2.2). The resonator has a fundamental mode at a wavelength considerably longer than any of the dimensions of the resonator. Through analogy with a mass on a spring, where the fluid contained within the neck is the mass, and the fluid contained within the cavity is the the spring, the resonant frequency of this fundamental mode may be calculated as follows.

The effective length of the neck is longer than the physical length of the neck due to end effects. If it is assumed that the internal end of the neck approximates a flanged opening as well as the external end, the effective length of the neck is approximately $L' = L + 1.7a$. Assuming a neck with cross-section S, the mass of fluid contained within the neck is therefore

$$m = \rho_0 S L'. \tag{2.31}$$

Due to a vibration, the mass of air in then neck is moved by a small distance x. The resulting pressure change in the cavity is proportional to the change in volume of the

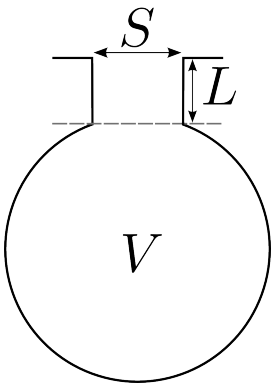

Figure 2.2: Schematic of a flanged Helmholtz resonator with cavity V, neck cross-section S and neck length L.

cavity via the ratio of the specific heats, γ, where $\gamma = \frac{C_P}{C_V}$; C_P and C_V are the heat capacities at constant pressure and constant volume respectively.

$$\frac{p}{P_0} = -\gamma\frac{\Delta V}{V} = -\gamma\frac{Sx}{V}. \tag{2.32}$$

A restoring force is applied to the mass of fluid in the neck as a result of the pressure change in the cavity. Applying Newton's second law results in

$$\frac{d^2x}{dt^2} = \frac{F}{m} = \frac{pS}{\rho_0 SL'} = -\frac{\gamma SP_0}{\rho_0 VL'}x. \tag{2.33}$$

The restoring force is thus proportional to the displacement and the frequency of oscillation is given by

$$f = \frac{1}{2\pi}\sqrt{\frac{\gamma SP_0}{\rho_0 VL'}}. \tag{2.34}$$

The speed of sound in a medium is given by the relation [41]

$$c^2 = \frac{\gamma P_0}{\rho_0}, \tag{2.35}$$

which reduces the equation determining the resonant frequency of a Helmholtz resonator to

$$f_H = \frac{c}{2\pi}\sqrt{\frac{S}{VL'}}. \tag{2.36}$$

The quality factor of a Helmholtz resonator is given by

$$Q = 2\pi\sqrt{V\left(\frac{L'}{S}\right)^3}. \tag{2.37}$$

Helmholtz resonators are relevant to the investigations presented in chapter 7.

2.5 Acoustic Losses

Until now it has been assumed that the losses associated with the propagation of the acoustic wave are negligible. While this is often the case, many of the results described in this thesis require the inclusion of viscous losses to truly describe the results observed. The viscous losses encountered are associated with the shearing forces between layers of a fluid that are moving at different speeds.

The first successful theory of sound absorption was developed by Stokes [54] by taking into account the effects of viscosity in a fluid. The nature of the boundary condition applicable at the interface between a fluid and a solid was widely debated in the 19th century. Navier is credited with providing the currently accepted boundary condition [55] which states that the tangential particle velocity falls to zero at the boundary with a solid. This *no slip* condition allows a bounding layer to be defined over which the particle velocity rises from zero to the maximal particle velocity and leads to curvature of the velocity wavefronts [56]. Kirchoff is credited with providing the theory of sound propagation through tubes [57], alterations to which were proposed by Rayleigh to treat the case of slits [58]. Rayleigh later provided a full treatment of the case of sound propagating between two parallel walls [59].

Retaining the effects of viscosity in developing the general force equation (i.e., Newton's second law) leads to the *Navier-Stokes* equation [55].

$$\rho\left(\frac{\partial\vec{u}}{\partial t}+\left(\vec{u}\cdot\nabla\right)\vec{u}\right)=-\nabla p+\left(\frac{4}{3}\eta+\eta_B\right)\nabla\left(\nabla\cdot\vec{u}\right)-\eta\nabla\times\nabla\times\vec{u}, \tag{2.38}$$

where the coefficient of shear viscosity, η, and bulk viscosity, η_B, are inherent to the medium of propagation and are determined experimentally. The final term on the RHS is associated with the vorticity of the fluid, which is negligible for our investigations. Vorticity is generally associated with turbulent (unstable) fluid flow.

The effect of the bounding layer is that energy losses occur due to the shearing experienced as layers moving at different speeds pass over one another. The effects of these losses are notable in the experimental results presented in chapters 5, 6, 7 and 10. Qualifying the situations under which viscous effects become significant is beyond the scope of this thesis; a comprehensive account is given by Tijdeman describing the propagation of sound waves in cylindrical tubes [56].

2.6 Floquet Theory

Floquet's theorem is integral to the calculation of the transmission/reflection of a wave from periodic structures. It is of importance when analysing any sort of periodic structure and is used in developing the modal-matching simulations found in appendices A and B. Although the maths is relatively well-known, a simple situation is described to demonstrate Floquet's theorem.

Consider a one dimensional structure which is infinite in the $\pm x$ direction and consists of a periodic feature of period Λ. Floquet's theorem can be used to solve how this structure interacts with an incident wave. The scattered wave is represented by the function $A(x)$ and the geometric periodicity of the surface forces the scattered field to be periodic i.e.,

$$\begin{aligned} A(x+\Lambda) &= CA(x), \\ A(x+2\Lambda) &= CA(x+\Lambda), \\ &\vdots \\ A(x+n\Lambda) &= CA(x+(n-1)\Lambda), \end{aligned}$$

where C is a complex constant and $|C| \leq 1$ to maintain the boundedness of the wave i.e. to prevent it being amplified. In general, $C = e^{ik\Lambda}$, where $k =$ a complex constant. From this definition, a function $P(x)$ can be defined, where $P(x) = A(x)e^{-ikx}$ and consequently:

$$\begin{aligned} P(x+\Lambda) &= A(x+\Lambda)e^{-ik(x+\Lambda)} = CA(x)e^{-ikx}e^{-ik\Lambda} = A(x)e^{-ikx} \\ &= P(x), \end{aligned}$$

and hence,

$$P(x+n\Lambda) = P(x).$$

P(x) is now a function which is is periodic with the same period Λ as the structure and can be expressed via a Fourier series expansion:

$$P(x) = \sum_{n=-\infty}^{\infty} p_{\mathrm{n}} e^{i\frac{2\pi n}{\Lambda}x}$$

where p_{n} is the amplitude coefficient of the n^{th} term.

Substituting in:

$$P(x) = A(x)e^{ikx}$$

then,

$$u(x) = \sum_{n=-\infty}^{\infty} p_{\mathrm{n}} e^{ikx} e^{i\frac{2\pi n}{\Lambda}x},$$
$$u(x) = \sum_{n=-\infty}^{\infty} p_{\mathrm{n}} e^{ik_{\mathrm{x_n}}x},$$

where

$$k_{\mathrm{x_n}} = k + \frac{2\pi n}{d}.$$

This represents a harmonic expansion of the wave A(x) where each $k_{\mathrm{x_n}}$ term represents a spatial *Floquet Harmonic* within an infinite series of waves which may propagate along the periodic axis in either direction. Floquet's theorem can be expanded to cope with higher dimension periodic structures.

Chapter 3

Techniques Used to Simulate the Acoustic Response

3.1 Introduction

This chapter provides background to the modelling methods used in this thesis, the Modal Matching (MM) method, an analytic treatment, and the Finite Element Method (FEM). Modal matching is used in Chapters 5, 6 and 8 to simulate the transmittance of fishnet structures in the absence of losses within the system. The method is considerably faster than FEM modelling for simple systems, where the description is purely analytical. The analytic treatments used in chapters 5, 6, 7 and 8 are vastly simplified models of the system that can provide a more intuitive understanding of the investigated systems. FEM modelling is a full-wave solver that allows modelling of the response of complex systems and the inclusion of complex physics such as the effects of viscous losses. The FEM modelling is extremely powerful but doesn't necessarily provide the intuitive understanding of a system gained from simpler analyses. In the lossless regime, the MM and FEM methods give near identical results.

3.2 Analytic Treatment

The structures studied in chapters 5, 6, 7 and 8 may be approximated as a series of pipes in different formations. Pipe acoustics has been extensively studied and the analytical treatment of the investigated systems makes use of simplified systems of pipes to determine the resonant modes of the investigated fishnet structures. The method makes assumptions to define the acoustic field in a system and using analytic reasoning searches for resonances. For simplicity it ignores any periodicity in the system i.e. it determines the response of single isolated pipe rather than an array of pipes.

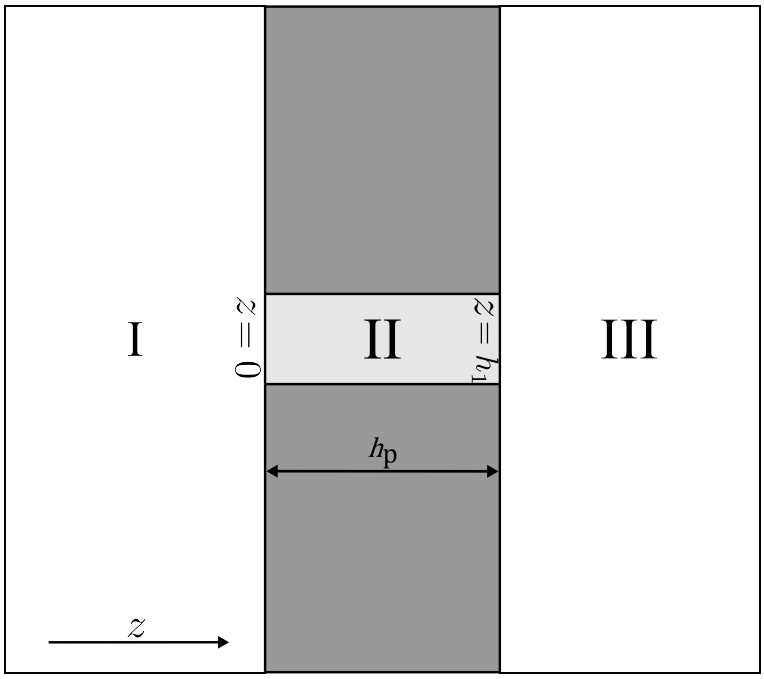

Figure 3.1: Schematic side view of the SF structure showing the different regions used in formulating the modal matching calculation of the structure's transmittance.

The utility of the analytical modelling is that it explicitly indicates the nature of the the various resonances and antiresonance. The model is best described through the implementations in chapters 5, 6, 7 and 8 however as a simple example refer to the derivation of the resonant modes of an open-ended pipe provided in section 2.4.

3.3 Modal Matching Method

The method of modal matching method determines the response of a system by solving the acoustic wave equation at the interfaces between two or more different regions and applying appropriate boundary conditions across it. The method is ideally suited to simple geometries with well defined boundary conditions such as that imposed by a perfectly rigid body. Here, as an example, we discuss the assumptions and boundary conditions applied to determine the transmittance of a single 'fishnet' (or hole array), a periodic structure described by a unit cell consisting of a rigid plate perforated with a single perforation running between the front and back faces (figure 3.1). A discussion of the resonant acoustic tunnelling of sub-wavelength apertures was provided by Christensen *et al.* [33] and a full description of the MM method used to calculate the transmittance of single and double fishnets is given in appendices A and B.

The structure is split into three regions, two semi-infinite free space regions either

side of the fishnet and the region within the fishnet, see figure 3.1. The boundary conditions imposed at the interface between these regions are readily arrived at by considering a uniform line of particles incident upon the interface of the unit cell. At the instantaneous moment in time that the particles reach the interface between the incident medium and the front face of the fishnet structure, the particles are all travelling with the same velocity. Thus the normal velocity across the entire unit cell must be continuous. At the same instant, particles incident on the rigid plate will exert a pressure on it while particles incident on the open end of the pipe will be free to propagate and exert a different pressure. Thus the pressure exerted is only continuous over the area of the hole.

Within the pipe the fields are expressed solely as the lowest order propagating mode, a plane wave. Higher order modes are prevented from propagating, i.e. they have a cut-off frequency, dictated by the sub-wavelength diameter of the pipe. The incident, scattered and transmitted fields above and below the surface of the fishnet are expressed as an infinite series of plane waves; Diffracted orders are accounted for through an implementation of Floquet's Theory [60]. In order to solve the problem successfully, the number of diffracted orders described by the infinite Fourier series must be truncated. The number of diffracted orders is chosen to achieve suitable convergence whilst minimising the computation time. We find that two diffracted orders is sufficient for the results to be sufficiently converged.

3.4 Finite Element Method (FEM)

The FEM method is a numerical modelling process used to predict the response of a wide variety of systems. Problems are subdivided into discrete elements represented by polygonal or polyhedral elements referred to as the 'mesh'. The relevant equations (as explained in section 3.4.1) are solved between each of the elements until a solution that is consistent across the whole system is found.

The software package COMSOL MULTIPHYSICS [61] is used to undertake the FEM modelling in this thesis. Models are constructed using the computer aided design component included with the software. Different modelling domains may be assigned different properties depending on the materials and the physics that is required to be solved within the domain.

3.4.1 Solving the Acoustic Equations in the Mesh

The domains of the model are split into *Pressure Acoustics* (PA) and *Thermo-Acoustics* (TA) depending on the physics that is required to be solved within the domain.

The PA physics is assigned to domains where losses are likely to be negligible, for example the semi-infinite incident and transmission domains either side of the fishnet structure. An incident field is provided using the *background pressure field* domain assignment. The software then applies the finite element method to solve for the pressure field, p_t, for each element using the wave equation,

$$\nabla \cdot \frac{1}{\rho_\mathrm{c}} \left(\nabla p_\mathrm{t}\right) - \frac{k^2 p_\mathrm{t}}{\rho_\mathrm{c}} = 0, \tag{3.1}$$

where ρ_c is the density of the domain material, p_t is the total pressure field, and k is the wave number. The particle velocity, $\vec{u}$, can then be obtained using,

$$\vec{u} = \frac{\nabla p_\mathrm{t}}{\rho_c}. \tag{3.2}$$

The wave equation must be satisfied for each mesh element leading to a matrix of many simultaneous equations which are solved for numerically.

In domains where losses due to thermal or viscous losses are no longer negligible, the TA domain assignment is applied. Within the TA domain a full description of the propagation of sound in fluids, which is derived from the governing equations of fluid flow, is required. Three equations form this description:

1. The conservation of momentum, referred to as the the Navier-Stokes equation:

$$i\omega\rho_0\vec{u} = \nabla \cdot \left[-\rho\mathbf{I} + \mu\left(\nabla\vec{u} + (\nabla\vec{u})^T\right) - \left(\frac{2}{3}\mu - \mu_\mathrm{B}\right)(\nabla\cdot\vec{u})\,\mathbf{I}\right], \tag{3.3}$$

   where $\mathbf{u}$ is the local particle velocity, μ is the dynamic viscosity, μ_B is the bulk viscosity and $\mathbf{I}$ is the unit matrix.

2. The conservation of mass, given by the continuity equation:

$$i\omega\rho_0\left(\frac{p}{p_0} - \frac{T}{T_0}\right) + \rho_0\nabla\cdot\vec{u} = 0, \tag{3.4}$$

   where T is the temperature in Kelvin and T_0 is the equilibrium temperature.

3. The energy conservation equation:

$$i\omega\rho_0 C_p T = -\nabla\cdot\left(k_\mathrm{T}\nabla T\right) + i\omega p, \tag{3.5}$$

   where C_p is the heat capacity at constant pressure and k_T is the thermal conductivity.

The complexity added by the inclusion of viscous effects significantly increases the size of the matrix of simultaneous equations to be solved for in TA domains. The structures in this thesis generally use a combination of PA and TA domains which must be matched across the common interfaces.

3.4.2 Types of Study

Two types of studies are used with the FEM modelling, a frequency-domain study and an eigen-frequency study. The frequency-domain study simulates the experimental set up by injecting a wave at given frequency for which the software finds a solution satisfying the relevant PA and TA equations. Using this study we are able to sweep through a range of frequencies and model the response of a system as a function of frequency which can then be compared to experimental data.

The eigen-frequency model determines the resonant frequencies of a given system by searching for the eigen-modes of the system. This is achieved by searching for solutions around a initial value and minimising the change in solution from one iteration to the next. Through this process the solver iteratively determines eigen-frequencies until a desired convergence is achieved.

3.4.3 Boundary Conditions and Domain Assignments

Figure 3.2 shows a cut-plane of a model used to determine the transmittance through a periodic hole array. The domains and boundaries are highlighted according to the labels.

Floquet periodicity is applied to parallel pairs of boundaries in order to model periodic structures as infinite arrays. The periodic condition is defined by a wave-vector, k_{F}, between pairs of boundaries which is used to satisfy the Floquet boundary conditions:

$$\vec{u}_{\mathrm{dst}} = \vec{u}_{\mathrm{src}} \exp\left[-ik_{\mathrm{F}} \cdot (\vec{r}_{\mathrm{dst}} - \vec{r}_{\mathrm{src}})\right], \tag{3.6}$$

$$T_{\mathrm{dst}} = T_{\mathrm{src}} \exp\left[-ik_{\mathrm{F}} \cdot (\vec{r}_{\mathrm{dst}} - \vec{r}_{\mathrm{src}})\right], \tag{3.7}$$

$$p_{\mathrm{dst}} = p_{\mathrm{src}} \exp\left[-ik_{\mathrm{F}} \cdot (\vec{r}_{\mathrm{dst}} - \vec{r}_{\mathrm{src}})\right], \tag{3.8}$$

where the subscripts ‘dst’ and ‘src’ refer to the destination and source boundaries. The angle of incidence in the frequency domain studies can be set by determining the phase relationship between the boundaries via $\Delta\phi = k_{\mathrm{F}} \cdot (\vec{r}_{\mathrm{dst}} - \vec{r}_{\mathrm{src}})$.

In order to model the experimental geometry a semi-infinite domain is required to mimic the free space regions surrounding the sample in reality. Without special domains which achieve this, the simulation would suffer from reflections and resonances, just as if

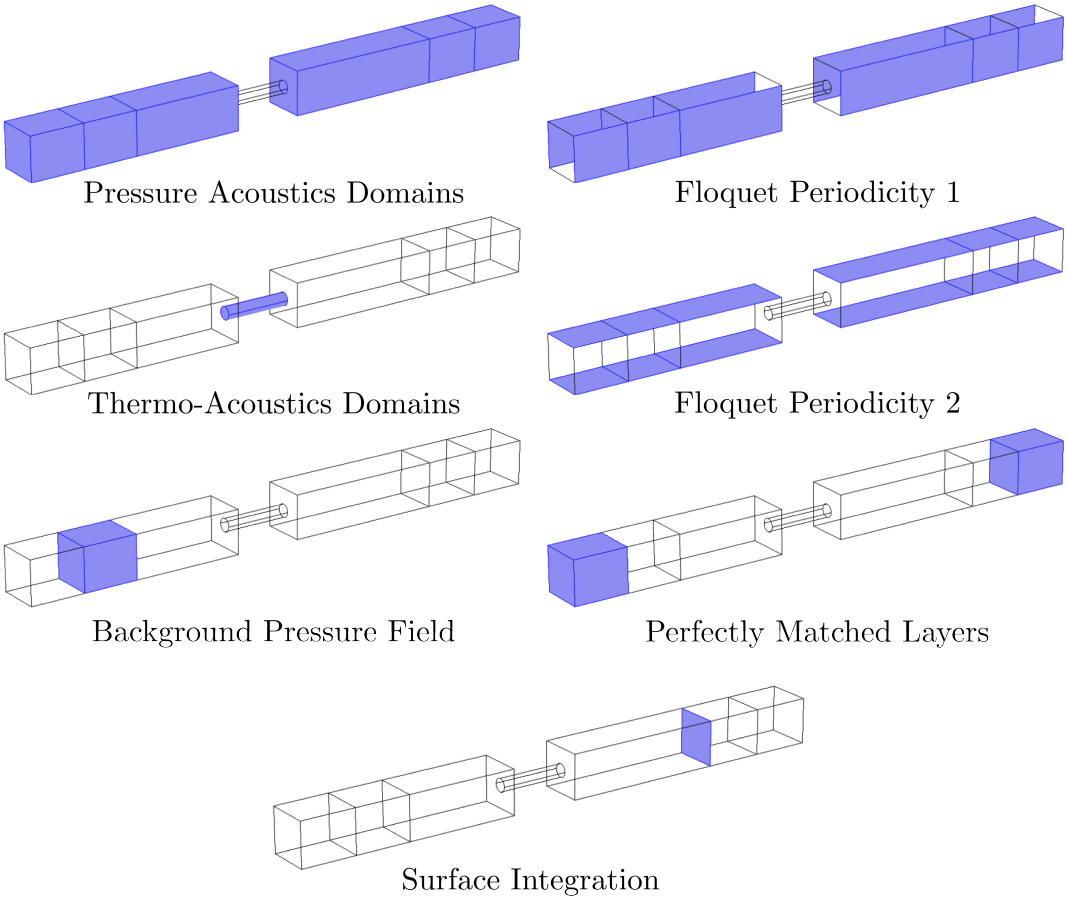

Figure 3.2: Schematic of the different domains and boundaries used in the FEM model of a single fishnet. The features are highlighted and named in each case.

the experimental setup was enclosed in a small box. A *Perfectly Matched Layer* (PML) applies a complex coordinate scaling within a domain such that the any waves incident within the PML are absorbed. An appropriate PML will produce no reflections of the wave incident upon it while absorbing the wave within it. Due to the mathematical complexities of implementing PMLs they do not absorb well at high angles of incidence.

3.4.4 Meshing

The structure of a mesh determines the accuracy of a simulation and influences the overall computation time required to solve for the fields. In general there should be five mesh elements per wavelength (determined by the highest frequency solved for). However, the mesh must also properly represent the geometry i.e., sharp corners and curved regions require denser meshes. Regions of rapidly changing fields also require a denser mesh e.g., within narrow regions where viscous losses (as discussed in chapter

2) have to be accounted for. A *boundary layer* mesh provides an extremely fine mesh close to the boundary while minimising the increase in the number of mesh elements. This is achieved by placing layers of elongated elements close to the boundaries.

3.4.5 Extracting Solutions

In frequency-domain studies the simulated transmittance/reflectance is determined by integrating the time-averaged pressure field across a boundary (see figure 3.2) and then normalising. The boundary is chosen within one of the PA domains where it does not interact with the interface between different domains e.g. the interface between PA and PML, or PA and TA regions. In reflection models (chapter 10) the time-averaged scattered pressure field is multiplied by $e^{-ik_x x}$, which through the orthogonality relationships of Fourier harmonics allows the zeroth order reflectance to be determined. The total reflected field is composed of the scattered field and the background through the relationship $p_\mathrm{t} = p_\mathrm{b} + p_\mathrm{s}$. Only the scattered field is of interest.

Eigen-frequency studies typically generate many solutions, the majority of which are spurious modes of the entire model which change in frequency depending on the size of the outer boundaries of the model (i.e., not the geometry of the structure of interest, e.g., the PML regions). To determine which of the eigen-frequencies are genuine the field profiles need to be studied, although as a rule of thumb for the systems studied the eigen-frequencies with the smallest imaginary component tended to be the genuine resonances of the system.

3.5 Advantages and Disadvantages of the Three Methods

The analytic treatment described in section 3.2 is a relatively simplistic model requiring a number of assumptions about the system to be modelled. The analytic modelling quickly shows where the various resonances and anti-resonances of a system will occur. As will be shown through the later implementations it is remarkable how much insight can be provided by these simplistic models; especially regarding why they respond as they do to a given input. The analytic model quickly fails when a system becomes increasingly complex, in part due to the need to employ computers to solve large numbers of simultaneous equations. In the studies presented the analytic model works extremely well because the structures can be modelled as relatively simple systems and there is no attempt made to model the vibrational modes of the solid parts of the structure, or the effects of thermo-viscous losses.

While the analytic model provides great insight into the nature of the resonances and anti-resonances associated with simple systems, a model that predicts the response of

the system off resonance is required. The MM method presented in section 3.3 provides this. In essence the MM method is also a simple analytic treatment of the system in question. An equation describing the acoustic response of the system is arrived at and can be numerically solved to obtain the complete frequency response of the system. The MM can only be employed in situations where the system in question is relatively simple and has clearly defined boundary conditions. While the MM method provides a great deal of insight into how a system will react for various input parameters, there is little to no indication of why it reacts in that way.

Complicated systems involving complex geometries or multiple different aspects of physics become extremely difficult to solve using simple analyses or the modal matching method. FEM modelling allows determination of the complete response of such systems by breaking the problem down into many small regions and solving the required equations in each domain simultaneously with all of the other regions. Such calculations can only be performed by a computer and even then the models can take a large amount of time to find the solution. In this thesis the vibrations of solids have been neglected to allow simplification of the models, however FEM modelling would allow the acoustic waves in the fluid and the vibrations associated with the solid structure to be solved for. FEM modelling has been employed to allow modelling of thermo-viscous effects, which can have a considerable impact upon the acoustic behaviour in narrow regions.

Chapter 4

Techniques Used to Measure the Acoustic Response

4.1 Introduction

This chapter details the apparatus and experimental arrangements used to conduct the investigations in this thesis. The experimental arrangements used for the airborne experiments in chapters 5, 6, 7 and 10 are described in section 4.2 and the set-up used for the underwater experiments in chapter 9 is described in section 4.3. The method for recording and analysing data is identical for both airborne and underwater investigations; section 4.4 details how the transmission and reflection response of the investigated structures is obtained.

4.2 Airborne Experiments

In order to conduct experimental investigations into the transmission and reflection properties of the structures studied, a collimating mirror arrangement is used to provide a plane wave incident onto the samples.

4.2.1 Apparatus

- An acoustic source (*Scan-Speak R3004/602010*) capable of generating sound from 1 kHz up to 40 kHz.
- A microphone constructed using an electret condenser microphone cartridge (*Panasonic WM-61A*) (see Figure 4.1 for circuit diagram)
- A waveform generator (*Agilent 33220A*)

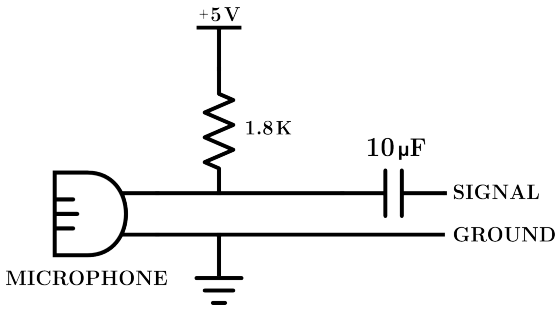

Figure 4.1: Circuit diagram of the internally constructed microphone.

- An audio amplifier (*Cambridge Audio Topaz*)
- A digital oscilloscope (*Picoscope 4604*)
- A Lock-In Amplifier (*Stanford Research Systems SR830*, see section 4.4.1)

4.2.2 Collimating Mirrors

A collimating mirror is used to obtain a plane wave from a point-like acoustic source located at the focus. A second identical mirror is used to refocus the collimated wave onto a microphone located at the focus. Ideally the mirrors should have a parabolic profile however for ease of production a spherical profile is used; there is negligible difference between either profile for the dimensions used. Each mirror is made by machining the 45 cm diameter cap of a 4 m diameter sphere into a 45 cm diameter aluminium cylinder to provide a 1 m focal length.

4.2.3 Experimental Arrangement for Transmission Experiments

Figure 4.2 shows the arrangement of the apparatus used for transmission experiments from (a) above (figure 4.2(a)) and (b) the side (figure 4.2(b)). The arrangement allows sound to be emitted from a source, collimated into a plane wave, transmitted through a sample or reference aperture and refocused onto a microphone as follows. The centres of the collimating mirrors and the sample are located at equal heights and separated by a nominal distance of 3.5 m. An acoustic source is placed at the focus of one of the mirrors such that the emitted pulse is directed towards the second mirror. A microphone is placed at the focus of the second mirror such that it detects sound focused from the mirror. Both the source and the microphone are vertically offset from the line passing through the centre of the two mirrors to minimise diffractive interference caused by placement of the source and detector in the path of the collimated beams (see figure 4.2(b)). Each mirror is rotated so that the strength of the detected signal is maximised.

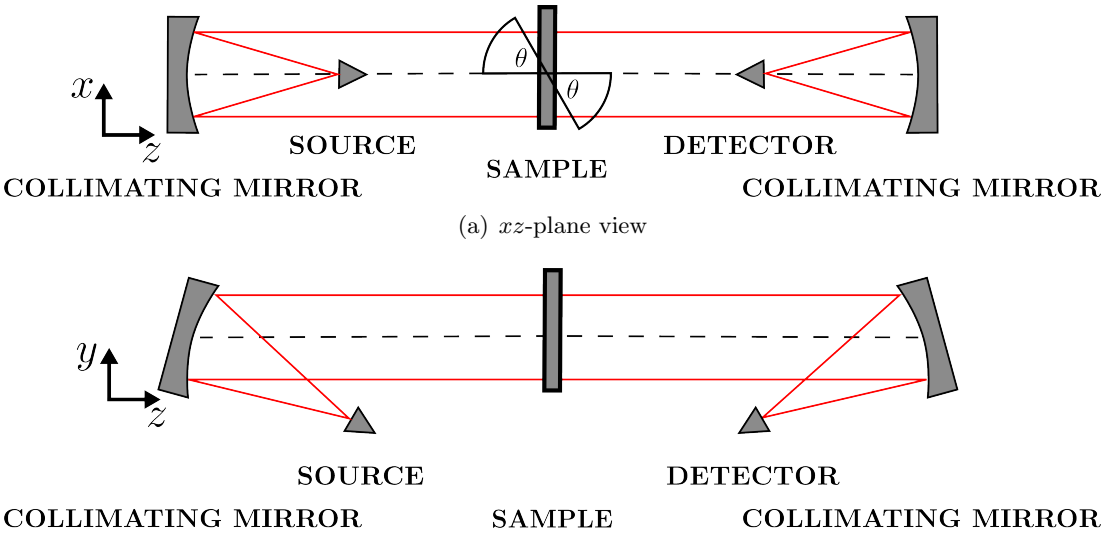

(a) xz-plane view

(b) yz-plane view

Figure 4.2: Schematic of the experimental arrangement for taking experimental transmission data in (a) xz-plane view and (b) yz-plane view.

Ideally the sample would occupy an area greater than the projection of the collimated beam, thus approximating an infinite sample, however smaller samples can be used by placing a rigid aperture around the sample. The angular dependence of a sample can be obtained by rotating the sample about the y axis. Acoustic absorber is strategically located to reduce the strength of any sound reaching the microphone via alternate paths.

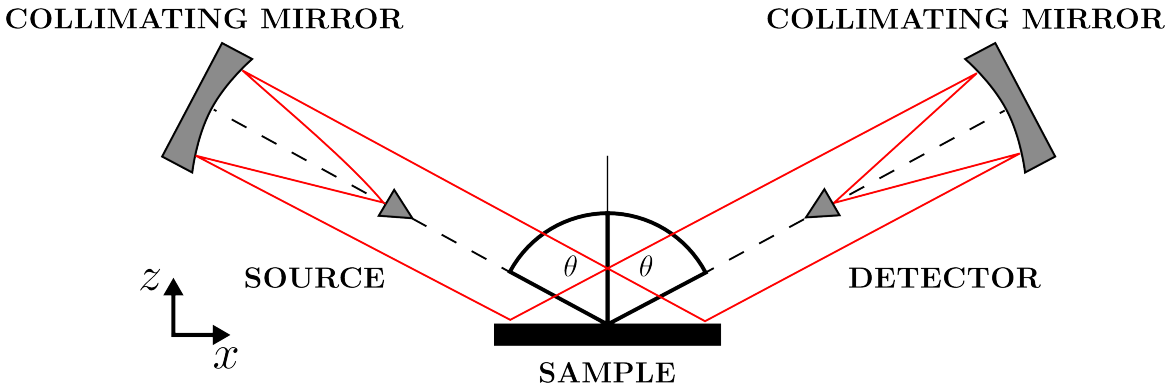

Figure 4.3: Schematic of the experimental arrangement for taking reflection data.

4.2.4 Experimental Arrangement for Reflection Experiments

Figure 4.3 shows the arrangement of the apparatus for reflection experiments. The arrangement allows sound emitted from a source to be collimated, reflected from a sample or reference surface, and refocused onto a microphone as follows. The centres of the collimating mirrors and the sample are located at the same height. The source and detector are placed as in the arrangement for transmission experiments (section 4.2.3). Each mirror is rotated so that the collimated beam reflecting of the sample gives a maximum signal at the detector. A frame was constructed to allow movement of one mirror by an angle θ whilst rotating the sample by $\frac{\theta}{2}$. The radius of the frame (2 m) is such that a 0.1° change in the incident angle corresponds to a 35 mm shift of the mirror around the sample, allowing considerable reliability in determination of the incident angle. The smallest angle of incidence achievable is 8.5°.

4.3 Underwater Experiments

Underwater experiments are undertaken in a 3 m × 2 m × 1.2 m tank as follows.

4.3.1 Apparatus

- A pair of underwater transducers capable of acting as either source or hydrophone (*Reson TC4013*)
- A waveform generator (*Agilent 33220A*)
- A low noise amplifier (*Brookdeal Electronics Type 450*)
- A wideband power amplifier (*Krohn-Hite 7500*)
- A digital oscilloscope (*Picoscope 4604*)

4.3.2 Experimental Arrangement for Underwater Transmission Experiments

Each transducer is attached to a 1 m long carbon fibre tube that is fixed to a carriage running along a beam spanning the short axis of the tank. The transducers are submerged to approximately half the depth of the tank and a sample placed between them (see figure 4.4). The sample is offset between the source and detector, with placement closest to the detector. The reasons for which are twofold: Firstly, the positioning of the sample minimises the detection of sound that is diffracted around the sample. Secondly, the investigations in chapter 9 look at the the transmission through a single

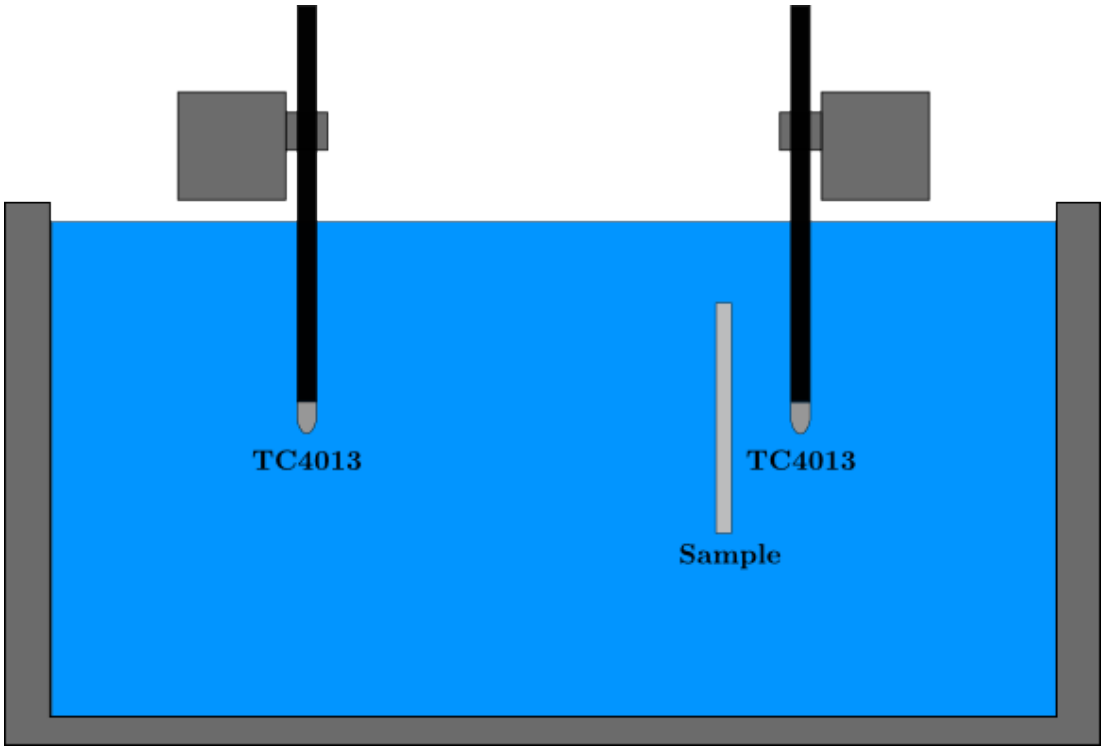

Figure 4.4: Schematic of the experimental arrangement for taking underwater data.

aperture. Placing the sample proximally to the detector minimises the signal loss due to beam spread as the transmitted wave diffracts out of the aperture.

4.4 Data Acquisition

The digital oscilloscope and the waveform generator are connected to a computer from which they can be controlled via a LabVIEW interface. Channel A of the digital oscilloscope is connected to the synchronisation output of the waveform generator and the output of the waveform generator is connected to the input of the audio amplifier (airborne)/ power amplifier (underwater), the output of which is connected to the source. The microphone (airborne) is connected directly into channel B of the digital oscilloscope; the hydrophone (underwater) is passed through a low noise amplifier to Channel B of the oscilloscope.

A custom waveform is formed by multiplying a single cycle of a sine wave with a Gaussian window. The electronic representation of the waveform is generated by the waveform generator and emitted as an acoustic pulse by the source. The detected signal is time-gated from just prior to the arrival of the pulse at the detector until sufficient time has passed that the signal returns to the background level; care is taken to avoid

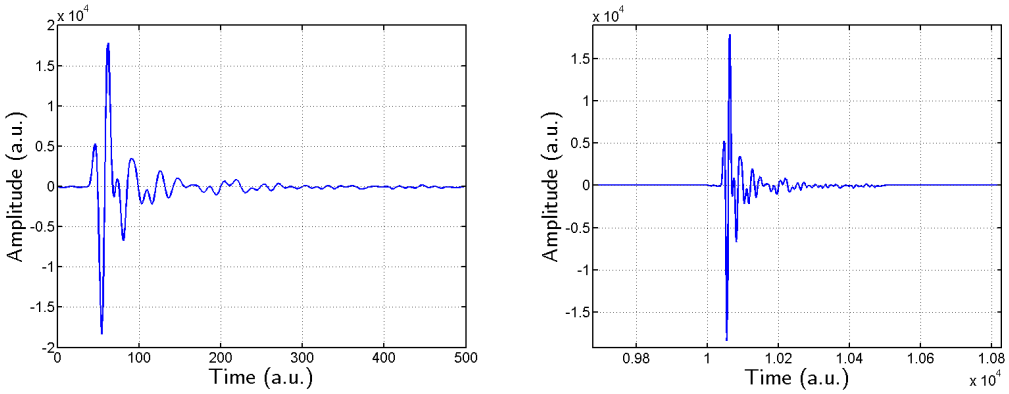

(a) (b)

Figure 4.5: (a) Example of a detected pulse and (b) the example pulse after zero-buffering and windowing.

the recording of any signals detected via alternate paths. The process is repeated and the recorded pulses are averaged to remove any background noise. Finally the averaged recorded pulse is windowed to ensure the signal level is zero at the beginning and end of the pulse; a trapezoidal window is used such that only the background level either side of the detected pulse is affected. An example of the detected pulse is shown in figure 4.5(a) and the buffered pulse in figure 4.5(b).

A fast fourier transform (FFT) of the detected pulse is taken after the signal has been buffered by the addition of ten-thousand zeroes, which artificially enhances the frequency resolution of the FFT. The effect of the buffering can be seen by comparing the FFT of the unbuffered example signal (figure 4.6(a)) and that of the buffered signal (figure 4.6(b). The FFT of the detected pulse with the sample present is compared to that of the FFT of a reference signal taken in the absence of the sample. Transmission or reflection properties are determined from this comparison. In addition to using the magnitude of the FFT to determine the amplitude of the transmitted/reflected signal relative to a reference signal, the FFT can also be used to compare the relative phase of each frequency component of the pulse. This analysis is useful for determining the frequency of a resonance when it cannot be determined from the amplitude. The phase of a frequency component is determined from the FFT by taking the arctan of the quotient of the imaginary and real parts.

$$\arctan\left(\frac{FFT_{\text{imag}}}{FFT_{\text{real}}}\right). \tag{4.1}$$

Due to the tan function being π-degenerate the phase has to be unwrapped so that the phase is continuously increasing as the frequency is increased rather than cycling

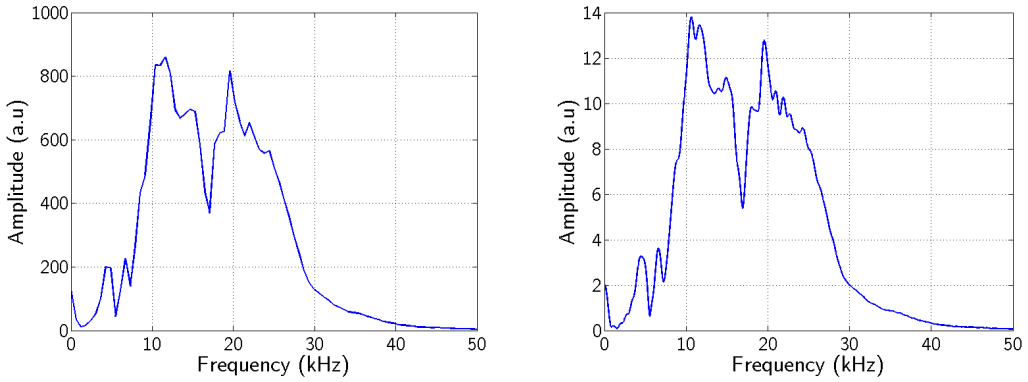

(a) (b)

Figure 4.6: (a) FFT of detected reference signal and (b) FFT of buffered reference signal.

between 0 and π. After unwrapping, the phase difference between the sample signal and the reference signal is taken. The phase difference should be zero everywhere except after going through a resonance where the phase will gain an additional π. To identify the frequency of the resonances the gradient of the phase is taken; where the gradient is a maximum corresponds to the resonant frequency. Chapter 10 uses this additional analysis due to the difficulties in identifying the frequency of the modes from the amplitude data.

4.4.1 Additional Data Obtained Using Continuous Wave Method

The experimental data in section 6.2 is undertaken using a different method to that above[1]. Using the transmission kit arrangement, (4.2.3), a continuous wave signal at a single frequency is transmitted from the source to the detector. The frequency of the signal is swept from 10 kHz to 40 kHz and the amplitude of the signal recorded by the lock-in amplifier for each frequency The lock-in amplifier replaces the digital oscilloscope in the arrangement. Amplitude data for the sample is divided by a reference signal obtained in the absence of the sample.

4.5 Frequency Range

To obtain the frequency range over which we may acquire data the frequency response of two reference signals taken proximally in time are compared. Ideally the magnitudes of the FFT's when divided would be equal to one across all frequencies.

[1]This method was superseded by the previously described method due to the significant improvements in the speed and signal-to-noise ratio of obtaining experimental data.

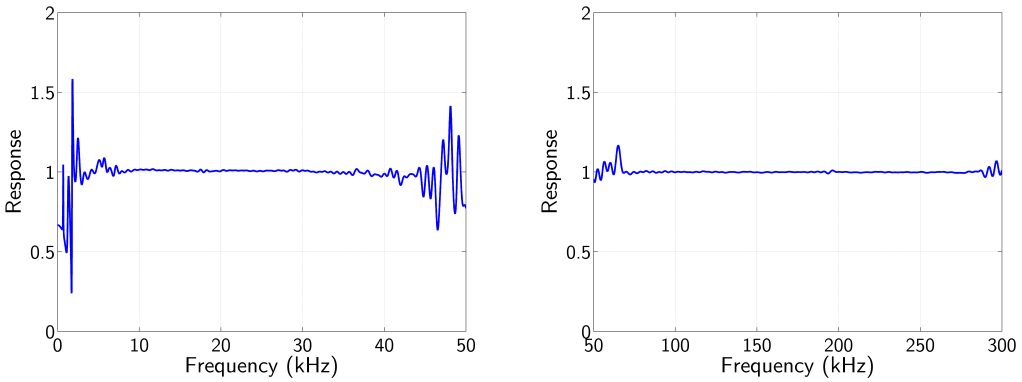

(a) Airborne Range (b) Underwater Range

Figure 4.7: Frequency range of the airborne and underwater arrangements over which reasonable data can be acquired.

4.5.1 Airborne Frequency Range

Figure 4.7(a) shows the ratio of the frequency response of two airborne reference signals. Between 8 kHz and 40 kHz the response is approximately equal to one, outside of this range the response degrades and we can no longer be confident about obtaining reliable data. This is due to a loss of reduced signal strength outside the frequency range and hence the ratio is of two small numbers.

Figure 4.7(b) shows the ratio of the frequency response of two underwater reference signals. The range over which we can confidently obtain data is approximately 70 kHz - 290 kHz.

4.6 Data Presentation

The experimental and modelled data is generally plotted on a decibel (dB) scale to facilitate to display of both high transmission and low transmission features. The pressure amplitude data is converted into decibels through the relationshiop given in equation (4.2).

$$20 \times \log\left(\frac{p_{\text{trans}}}{p_{\text{ref}}}\right), \tag{4.2}$$

where p_{trans} is the transmitted pressure level and p_{ref} is the reference pressure level.

Chapter 5

Acoustic Transmission of Hole Arrays in Air

5.1 Introduction

In this chapter, the acoustic transmittance of rigid plates perforated with a square array of circular holes (termed fishnets) are investigated. Initial experiments establish the transmittance of a series of single fishnet (SF) plates, which exhibit a series of transmission peaks associated with the excitation of pipe resonances in the holes. Following this we investigate the transmittance of a double fishnet (DF), which consists of two fishnets placed parallel to one another and separated by a sub-wavelength gap. The DF exhibits a similar series of transmission peaks in addition with a narrow acoustic stop-band associated with a resonant mode of the gap.

5.2 Acoustic Transmittance of the Single Fishnet

Consider a rigid plate of thickness h_p perforated with d diameter circular holes in a square array of pitch Λ to form an SF as shown in figure 5.1.

5.2.1 Simulated Transmittance

Figure 5.2 shows simulated transmission data for a SF as a function of the plate thickness h_p calculated using the MM method provided in appendix A. The pitch of the hole array is $\Lambda = 8$ mm and the hole diameter is $d = 2.4$ mm. A family of transmission peaks is clearly identified in red while blue regions indicate a lower level of transmission. As expected from the theory of an open-ended pipe (section c:theory:open-endedpipe), the thinner plates exhibit fewer peaks in transmission across the plotted frequency band

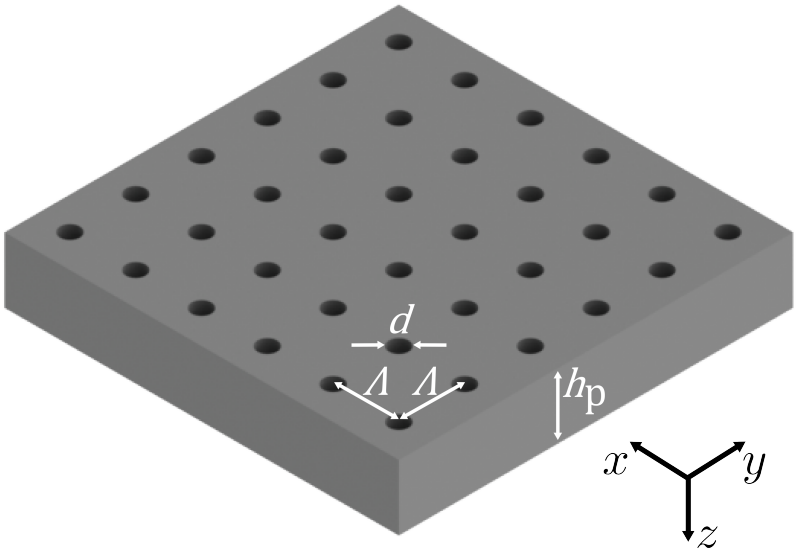

Figure 5.1: Schematic drawing of a single rigid plate perforated with a periodic square array of circular holes. Λ is the pitch of the hole array, d is the diameter of the holes and h_p is the thickness of the plate.

compared to the number for thicker plates and for a fixed plate thickness the peaks are equally spaced. Tracking any single transmission peak shows a decrease in the frequency at which it occurs as the thickness of the plate increases. These peaks bear a strong resemblance to the electromagnetic Fabry-Pèrot modes observed when light is transmitted through a pair of parallel partial mirrors [62].

5.2.2 Analytic Model of the Single Fishnet

We can understand these transmission peaks by comparison to the resonant modes of an open-ended pipe with cross-sectional area $S = \frac{\pi d^2}{4}$ and length h_p. An analysis of the resonant modes of this pipe (given in section 2.4.2) shows these resonant modes to be given by

$$f_n = \frac{Nc}{2h'_p}, \tag{5.1}$$

where $h'_p = h_p + 1.7d$ is the effective length of the pipe after accounting for end effects and N is an integer. This states that resonant modes will occur at frequencies corresponding to the fitting of n half wavelengths into the effective thickness of the plate.

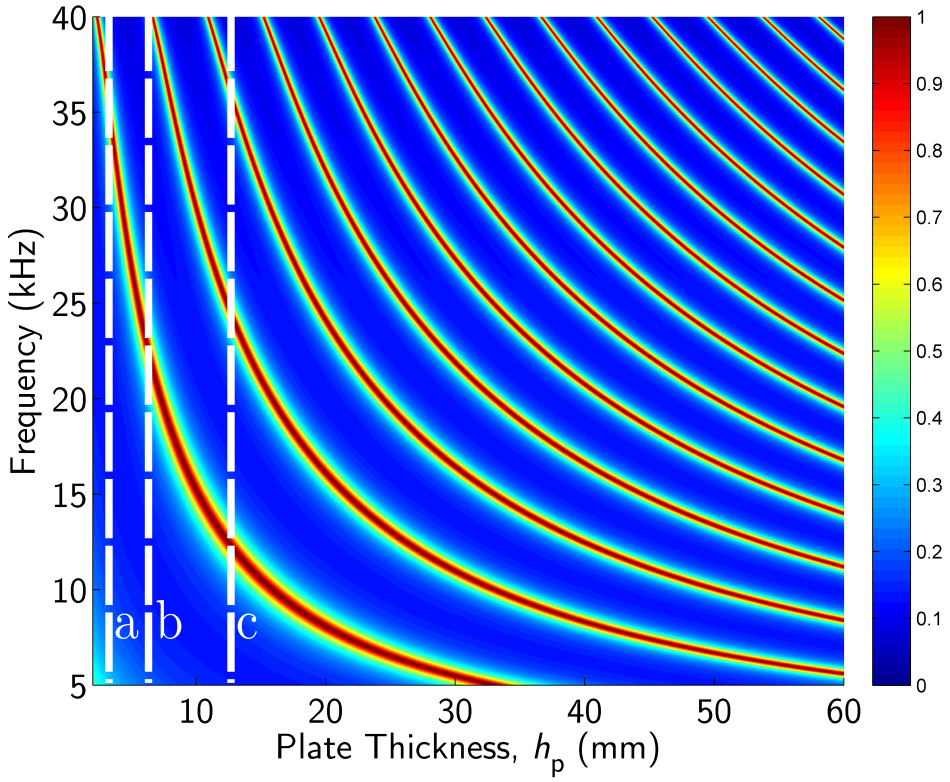

Figure 5.2: Transmission spectra through a single solid plate perforated with a square array of holes as a function of the plate thickness, h_p. The diameter of the holes is 2.4 mm and the pitch of the hole array is 8 mm. Dashed lines a, b and c correspond to the experimentally obtained data in figure 5.4.

Arbitrarily choosing a plate thickness of $h_p = 20$ mm suggests transmission peaks will occur at 8 kHz intervals beginning at 8 kHz in accordance with the predictions of the MM method (Appendix A shown in figure 5.2.

5.2.3 Experimental Transmittance

The acoustic transmittance through three SF structures has been measured experimentally using the collimated beam arrangement described in section 4.2.3. The samples consist of 200 mm × 200 mm perspex plates with thickness $h_p = 2.97$ mm, 5.96 mm and 12 mm. Each plate is perforated with a square array of holes with radius $d = 2.40$ mm and pitch $\Lambda = 8.00$ mm. The values of h_p correspond to the white dashed lines labelled a, b and c in figure 5.2. The experimental data, shown in figure 5.3 (blue line) clearly distinguishes the peaks in transmission associated with the resonant pipe modes for each plate thickness. Comparison with the simulated transmission data (red line)

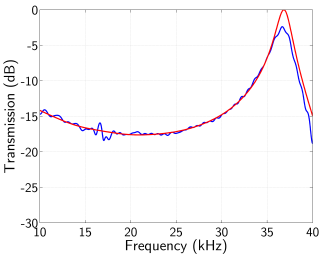

(a) $h_{\mathrm{p}} = 2.97$ mm

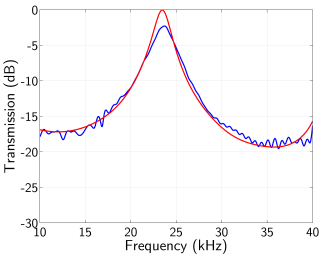

(b) $h_{\mathrm{p}} = 5.96$ mm

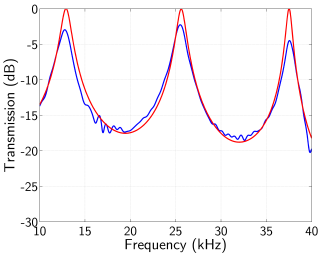

(c) $h_{\mathrm{p}} = 12$ mm

Figure 5.3: Experimental transmission data (blue) of three difference thickness single fishnet structures compared with simulated data excluding the effects of thermo-viscous losses (red). In each system the hole diameter $d = 2.4$ mm and the pitch of the hole array $\Lambda = 8$ mm.

from the MM method shows quite good agreement with the positions of the modes. However, the experimental data shows a reduced level of transmission compared to that of the simulated data.

This reduced level of transmission is not due to losses inherent to the experimental arrangement but rather due to thermo-viscous losses within the holes of the SF (section 2.5). Using FEM modelling we are able to simulate the transmission of the structure with the inclusion of these losses. Figure 5.4 shows the same experimental data as figure 5.3 overlaid with the simulated transmission data (red line) as predicted from the FEM model. The level of transmission now agrees with that experimentally achieved. From here on, experimental data will be presented solely with simulated data from FEM modelling.

5.3 Acoustic Transmittance of the Double Fishnet

Consider now a structure consisting of two fishnets placed in parallel with their holes aligned and separated by a sub-wavelength gap h_{g} to form a DF as shown in figure 5.5. The DF has been predicted to possess an acoustic stop-band associated with the gap

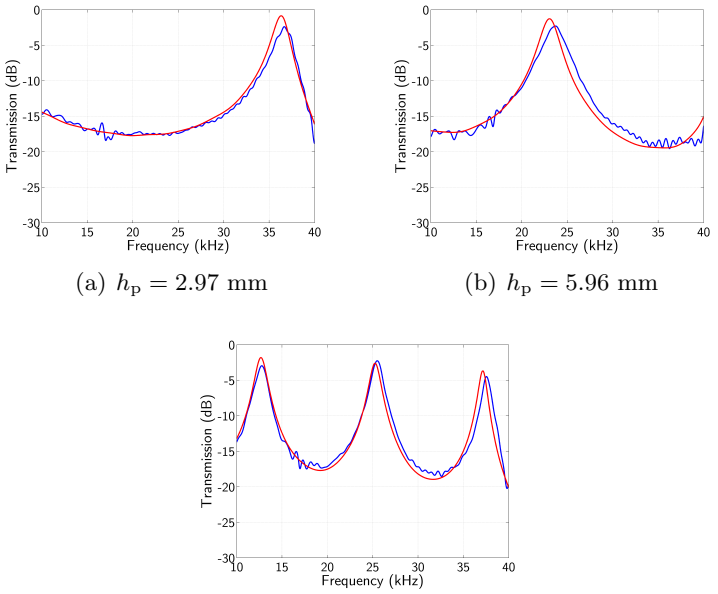

(a) $h_\mathrm{p} = 2.97$ mm (b) $h_\mathrm{p} = 5.96$ mm

(c) $h_\mathrm{p} = 12$ mm

Figure 5.4: Experimental transmission data (blue) of three difference thickness single fishnet structures compared with simulated data including thermo-viscous losses (red). In each system the hole diameter $d = 2.4$ mm and the pitch of the hole array $\Lambda = 8$ mm.

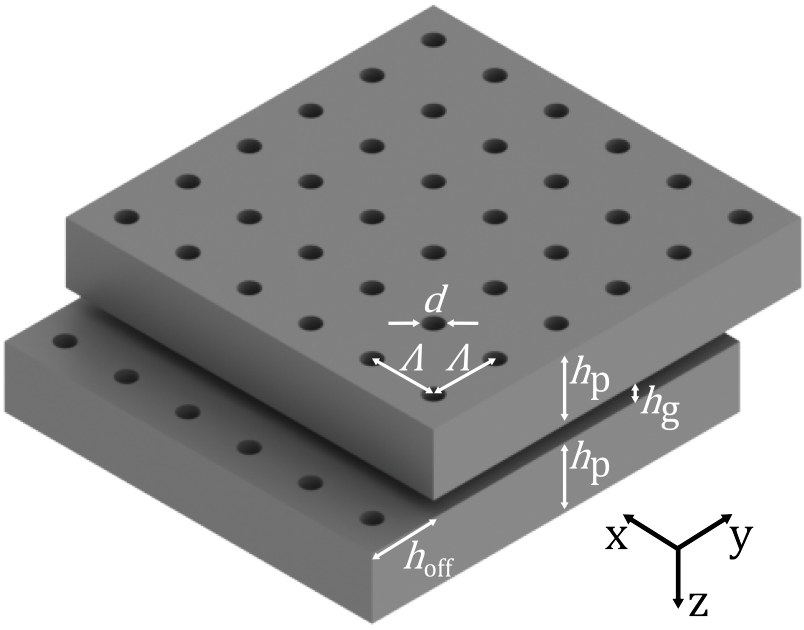

Figure 5.5: Schematic drawing of the DF structure consisting of a pair of rigid plates perforated with a periodic square array of circular holes.

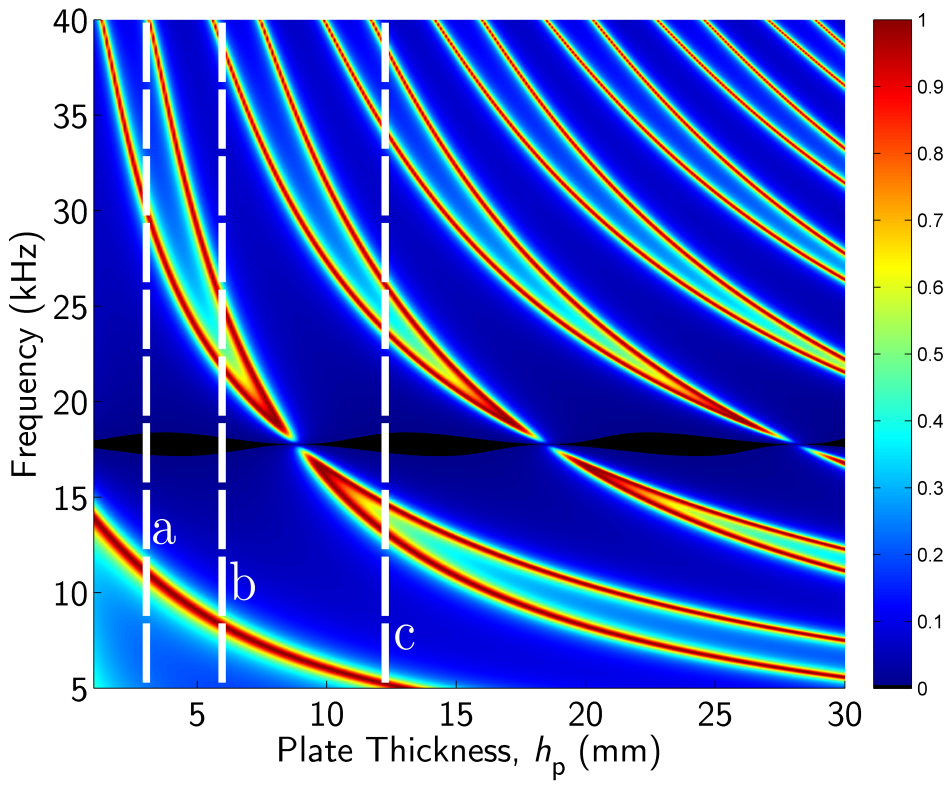

Figure 5.6: Transmission spectra of the DF structure as a function of the plate thickness h_p. Red indicates high transmission, blue indicates low transmission and black indicates less than -46 dB transmission. Dashed lines a, b and c correspond to the experimentally obtained data in figure 5.11.

between the plates [36, 63].

5.3.1 Simulated Transmittance

Figure 5.6 shows the transmittance of the DF as a function of the plate thickness as calculated using the MM method provided in appendix B. As with the SF above, the pitch is $\Lambda = 8.00$ mm and the hole diameter is $d = 2.40$ mm; the gap between the plates is $h_g = 0.94$ mm. In this analysis the plate thickness h_p corresponds to the thickness of an individual plate rather than the total thickness of the structure which is $2h_p + h_g$. As with the SF a series of transmission peaks (red) are observed. However, rather than being equally spaced the modes appear to be collected in pairs which converge at 18 kHz. This apparent mode crossing will be revisited in section 5.3.3.

A narrow band of less than -46 dB (0.05%) transmission can be seen at 18 kHz (black band) across the range of h_p. It is this acoustic stop-band which is of interest

as it may provide a way of preventing the transmission of sound whilst allowing air to flow through the structure. That the stop-band is unaffected by the plate thickness indicates that it arises because of the gap. The frequency of the stop-band can be estimated by fitting a half-wavelength in between two adjacent holes which for the described structure corresponds to 21.5 kHz.

5.3.2 Analytic Model of the Double Fishnet

To analyse the acoustic transmittance of this structure, consider a unit cell of the square array centred on a pair of aligned holes. The two holes may be considered to form a single open-ended pipe whose walls include a gap at its mid-point. As with the SF this pipe will support a series of pipe resonances at frequencies governed by the length of the pipe, the modes of which can be calculated as follows.

Consider an open-ended pipe with length $h_\mathrm{T} = 2h_\mathrm{p} + h_\mathrm{g} + \Delta L$ (where ΔL is the end correction) and cross-section S, running in the z direction from $z = -\frac{h_\mathrm{T}}{2}$ to $z = +\frac{h_\mathrm{T}}{2}$. The pipe has a resonant side branch at its midpoint at $z = 0$ which we assume has negligible width in the z direction.

5.3.2.1 Even-order Modes

The even-order pipe modes have a pressure node at $z = 0$ and so do not couple to the side branch. The resonance frequencies of the even-order modes are hence the same as for the case where no side branch is present, given by:

$$f = \frac{Nc}{2h_\mathrm{T}}, \tag{5.2}$$

where N is an even integer and c is the speed of sound.

5.3.2.2 Odd-order Modes

For the odd-order pipe modes the acoustic pressure has nodes at $z = -\frac{h_\mathrm{T}}{2}$ and $z = +\frac{h_\mathrm{T}}{2}$, ignoring end effects, and is symmetric about the point $z = 0$. In the region $0 \leq z \leq h_\mathrm{T}/2$ the acoustic pressure can be represented by the standing wave

$$p_1(z,t) = D \exp\left(i2\pi f t\right) \sin\left[\left(\frac{2\pi f}{c}\right)\left(z - \frac{h_\mathrm{T}}{2}\right)\right], \tag{5.3}$$

where D is a constant and f is the mode frequency.

The corresponding expression for the associated standing wave of volume velocity

in the same region is

$$U_1(z,t) = i\frac{D}{Z}\exp\left(i2\pi ft\right)\cos\left[\left(\frac{2\pi f}{c}\right)\left(z-\frac{h_\mathrm{T}}{2}\right)\right], \tag{5.4}$$

where Z is the acoustic impedance for a travelling wave in the pipe. Volume velocity is defined in the positive z direction. Equation (5.4) is obtained from equation (5.3) using the continuity equation $\frac{\partial p_1}{\partial t} = -Zc\frac{\partial U_1}{\partial z}$.

At $z = 0$, equations (5.3) and (5.4) give

$$p_1(0,t) = -D\exp\left(i2\pi ft\right)\sin\left(\frac{\pi f h_\mathrm{T}}{c}\right), \tag{5.5}$$

and

$$U_1 = i\frac{D}{Z}\exp\left(i2\pi ft\right)\cos\left(\frac{\pi f h_\mathrm{T}}{c}\right). \tag{5.6}$$

By considering the symmetry about $z = 0$ the standing waves $p_2(z,t)$ and $U_2(z,t)$ in the region $-\frac{h_\mathrm{T}}{2} \leq z \leq 0$ gives, at $z = 0$

$$p_2(0,t) = -D\exp\left(i2\pi ft\right)\sin\left(\frac{\pi f h_\mathrm{T}}{c}\right), \tag{5.7}$$

and

$$U_1 = -i\frac{D}{Z}\exp\left(i2\pi ft\right)\cos\left(\frac{\pi f h_\mathrm{T}}{c}\right). \tag{5.8}$$

The pressure $p_3(t)$ at the entrance to the side branch ($z = 0$) can be obtained from equation (5.5) (or equivalently from equation (5.7)).

For reasons of continuity the volume velocity $U_3(t)$ into the side branch is the difference between the expressions in equations (5.6) and (5.8).

$$U_3(t) = U_2(0,t) - U_1(0,t) = -i\frac{2D}{Z}\exp\left(i2\pi ft\right)\cos\left(\frac{\pi f h_\mathrm{T}}{c}\right). \tag{5.9}$$

Additionally, $p_3(t)$ and $U_3(t)$ are related by the acoustic input impedance of the side branch which, assuming a lossless side branch, is purely imaginary. Using equations (5.5) and (5.9), this relation can be written as

$$\frac{p_3(t)}{U_3(t)} = \frac{Z}{2i}\tan\left(\frac{\pi f h_\mathrm{T}}{c}\right) = iX, \tag{5.10}$$

where X is the input reactance of the side branch.

Equation (5.10) may be rearranged to give an expression for the frequencies of the

odd-order modes:

$$f = -\frac{c}{\pi h_{\mathrm{T}}} \tan^{-1}\left(\frac{2X}{Z}\right). \tag{5.11}$$

Note that Z is independent of f but X is not, as is shown below.

For a resonant side branch with a resonant frequency f_{gap}, the input reactance at frequency f can be written as

$$X = -\frac{zS}{\alpha} \cot\left(\frac{\pi}{2}\frac{f}{f_{\mathrm{gap}}}\right), \tag{5.12}$$

where α is the cross-section of the entrance to the side branch. This expression is easily derived for a resonant side branch in the form of a closed pipe of uniform cross-section α; for a resonant side branch of a different geometry, equation (5.12) is only an approximation. Note that the input reactance X goes to zero at the resonant frequency f_{gap}.

Equations (5.11) and (5.12) are combined to give

$$\tan\left(\frac{\pi f h_{\mathrm{T}}}{c}\right) = \frac{2S}{\alpha} \cot\left(\frac{\pi}{2}\frac{f}{f_{gap}}\right), \tag{5.13}$$

which can be numerically solved to obtain values for the frequencies f of the odd-order modes. The cross-section of the entrance to the side branch can be approximated as the curved surface of a cylinder joining the two pipes. The solutions shown in figure 5.7 were obtained using a value of 1.27 arrived at by taking $S = \frac{\pi d^2}{4}$ and $\alpha = \pi d h_{\mathrm{g}}$.

The predicted mode frequencies for both even- and odd-order modes are shown in figure 5.7 over a range of values of h_{p}.

5.3.2.3 Resonant Mode of the Gap

A more accurate expression for the frequency of the stop-band can be obtained by considering the fundamental mode of the gap. The unit cell provides boundary conditions from which this fundamental mode may be estimated. A simplifying assumption is made that the radially expanding acoustic field into the gap has plane wave fronts parallel to the cell boundaries. Due to the narrowness of the gap the fields are considered to be two-dimensional, expanding in the x and y axes. The spatial variation of the pressure amplitude is approximated by a solution of Bessel's equation of order zero, of the form

$$p(r) = AJ_0(kr) + BY_0(kr), \tag{5.14}$$

where A and B are constants, k is the wave number, r is the distance from the centre of the hole (measured along a line perpendicular to the unit cell boundary) and J_0 and

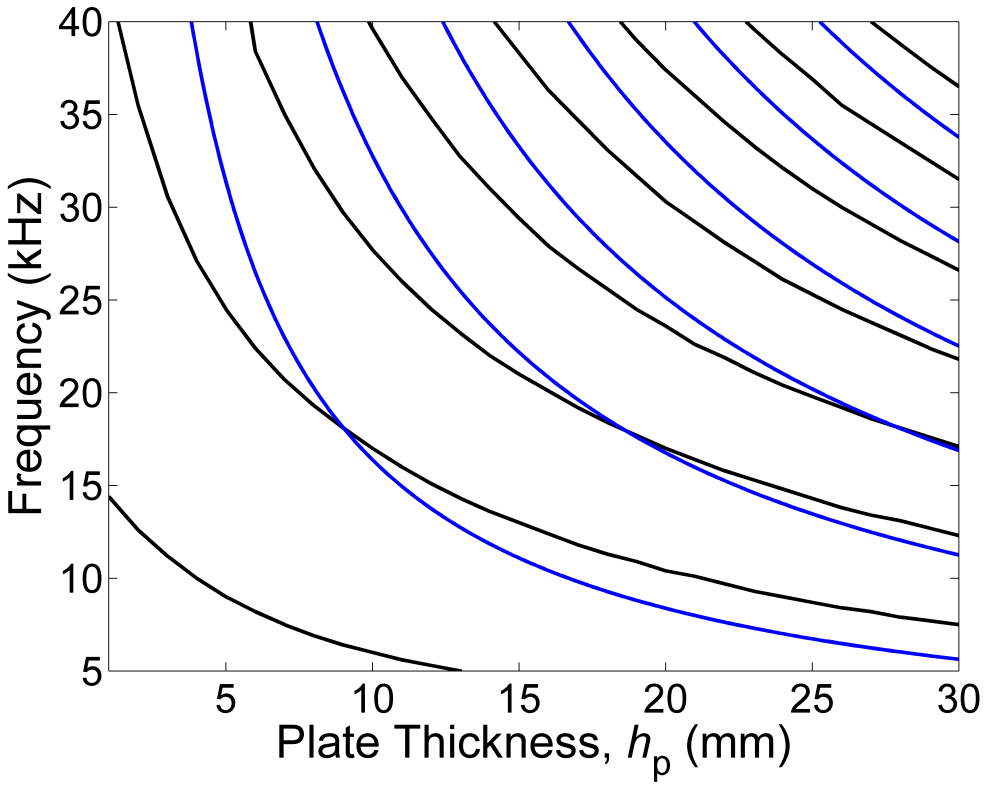

Figure 5.7: Resonant frequencies of the DF as numerically determined by equations (5.2) and (5.13). Odd-order modes are shown as black lines and even-order modes are blue lines.

Y_0 are zero-order Bessel functions of the first and second kinds, respectively. Symmetry arguments require a pressure anti-node at the boundary of the unit cell and a pressure node at the perimeter of the hole that, due to end effects, exists outside the gap region, i.e. within the pipe. By considering the positions of the node and anti-node for the structure, for which $a/\Lambda = 0.15$, the ratio of A/B is estimated as 1.1 and k is estimated as $2.5/\Lambda$. This corresponds to a resonant frequency of 17 kHz for a pitch of 8 mm which agrees more closely with the stop-band seen in figure 5.6.

5.3.3 Pressure Profiles of the Crossing Modes

The modes of the DF can be formed into pairs which appear to cross over at the frequency of the stop-band. To understand what is happening, instantaneous pressure profiles along a line through the centre of the pipe are plotted from FEM modelling in figure 5.9 (corresponding to markers A-I in figure 5.8). The mode following the line B, D, E, G, I corresponds to the 2nd mode of the system which is unperturbed by the

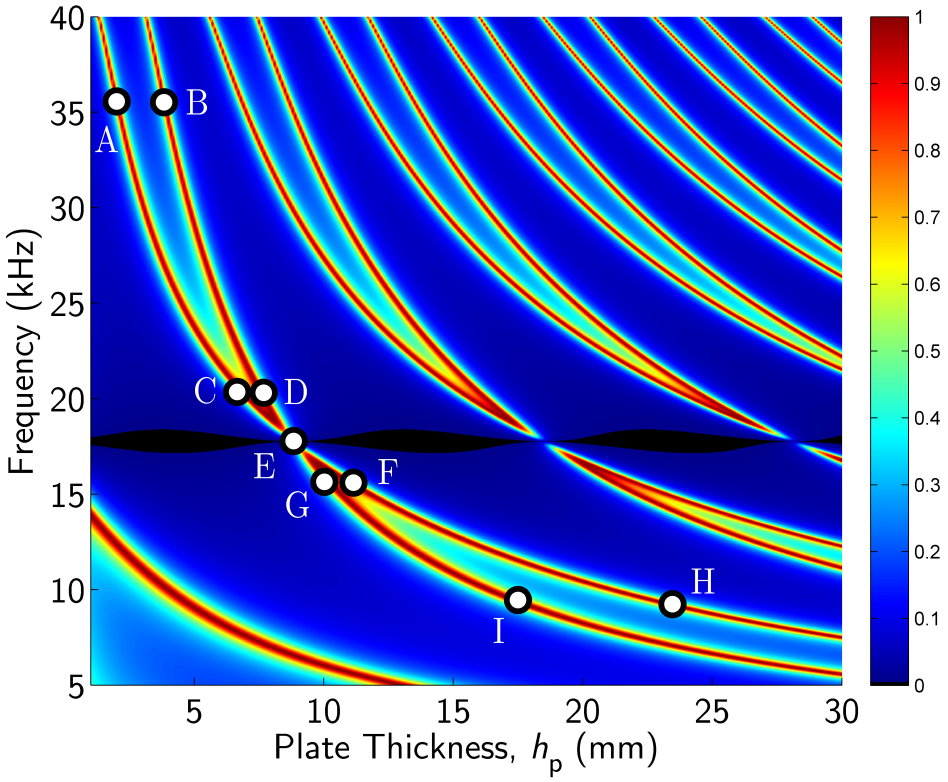

Figure 5.8: Transmission spectra of the DF structure as a function of the plate thickness h_p. Markers correspond to the instantaneous pressure profiles in figure 5.9.

presence of the gap. As the plate thickness is increased the shape of the mode remains largely unchanged. The mode following the line A, C, E, F, H reveals that the mode doesn't cross over the 2nd mode. Between A, C and E the pressure profiles correspond to the fundamental mode of the system and between E, F and H the pressure profiles correspond to the third mode of the system. Comparing figures 5.2 and 5.6 at positions of equivalent thickness the splitting of the odd modes becomes apparent (note that the total thickness of the DF is $2h_p + h_g$). The odd modes split and diverge either side of the stop-band, the shift in frequency is upwards for frequencies above f_{gap} and downwards for frequencies below f_{gap}. The interaction of the odd-order modes with the gap leads to a situation where at a given plate thickness a mode associated with one value of N may exist at two different frequencies, although the profiles of the modes are somewhat different. For instance, when $h_p = 5$ mm the modes at 12 kHz and 23 kHz both appear as the fundamental resonance ($N = 1$) as seen in figure 5.10.

Pressure profile E corresponds to the stop-band frequency at which no sound is transmitted through the structure and there is no pressure field excited in the latter

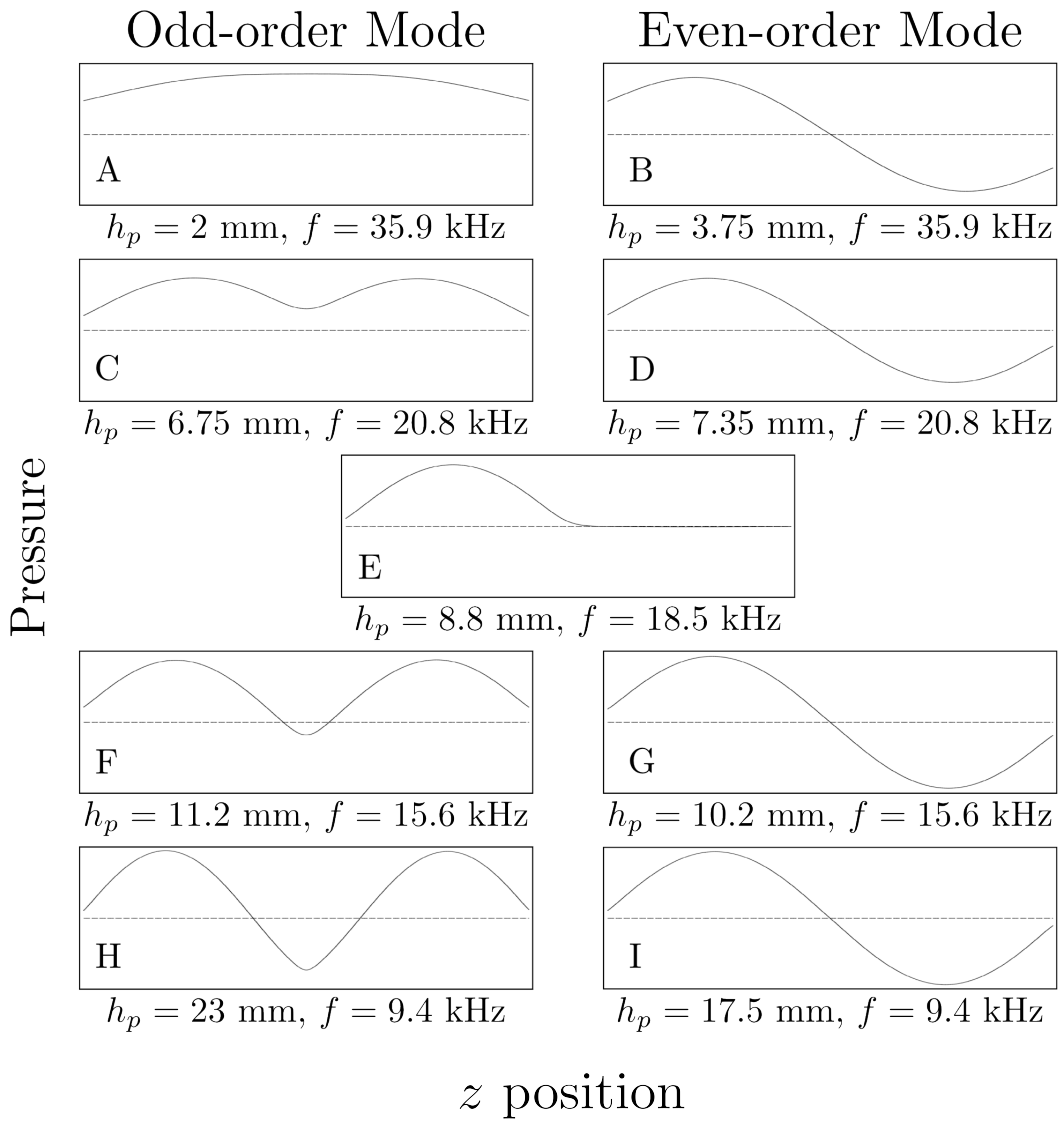

Figure 5.9: Instantaneous pressure profiles along a line through the centre of the pipe at the marked positions in figure 5.6. The shape of the even-order mode remains essentially unchanged as the plate thickness varies, however the odd-order mode changes due to coupling into the gap.

half of the pipe.

5.3.4 Experimental Transmittance

The acoustic transmittance through three DF structures has been measured experimentally using the collimated beam arrangement (section 4.2.3). The three samples consist of a pair of 200 mm × 200 mm perspex plates with thickness $h_\mathrm{p} = 2.97$ mm, 5.96 mm

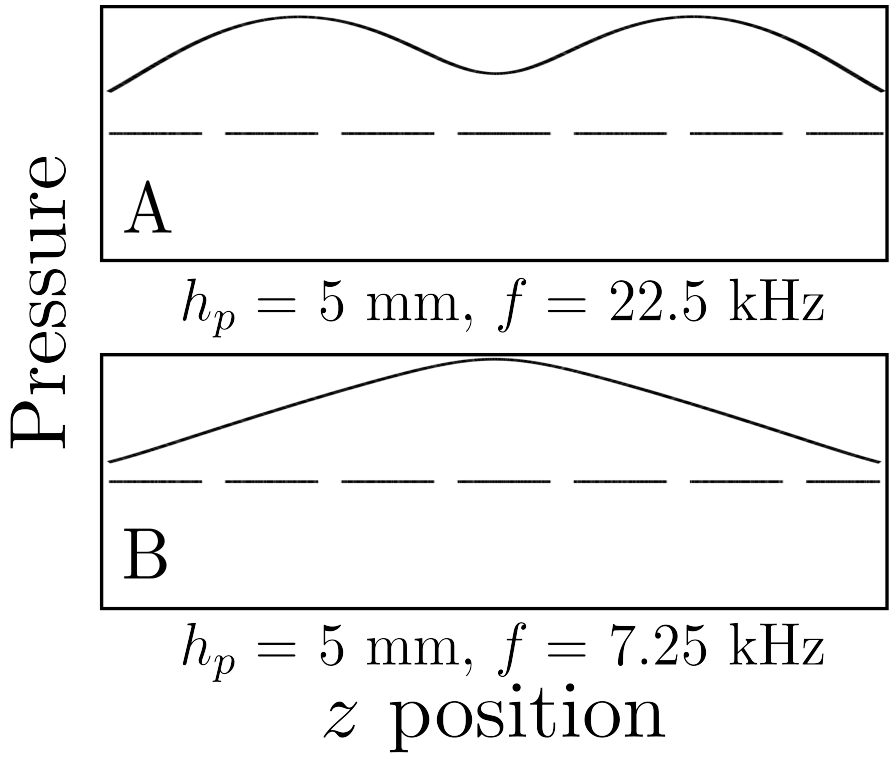

Figure 5.10: Instantaneous pressure profiles along a line through the centre of the pipe for the two fundamental modes at $h_\mathrm{p} = 5$ mm.

and 12 mm. Each plate is perforated with a square array of holes with radius $d = 2.4$ mm and pitch $\Lambda = 8$ mm. The plates comprising each pair were clamped together with a separation of 0.94 mm corresponding to the thickness of two metal washers.

Figure 5.11 shows the experimentally determined transmittance of each of the three pairs of plates. The experimental data (blue lines) are in good agreement with the simulations undertaken by the FEM method (red lines). The normalized transmission falls to less than -40 dB at the centre of the stop band for all three structures.

5.4 Acoustic Transmittance of Double Fishnet with Unequal Thickness Plates

As the plate thickness h_p is increased in the DF the odd-order modes appear to cross over the even-order modes at the frequency of the gap resonance such that the first mode becomes the third mode, the third becomes the fifth mode and so on. To explore this further, the relationship between the thickness of each plate in the DF is changed such that there is a simple ratio in thickness between the two plates.

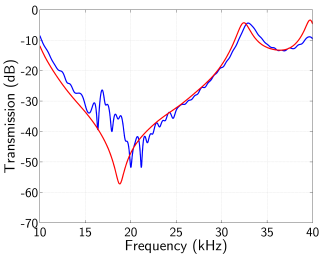

(a) $h_{\mathrm{p}} = 2.97$ mm

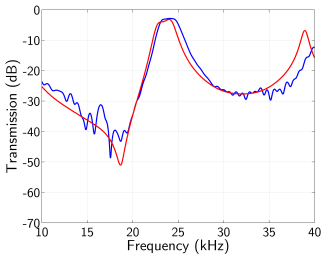

(b) $h_{\mathrm{p}} = 5.94$ mm

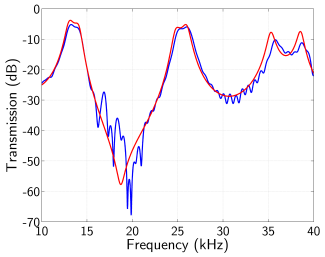

(c) $h_{\mathrm{p}} = 12$ mm

Figure 5.11: Experimental transmission data (blue) of three ADF structures compared with modelled data (red). In each system the gap size $h_{\mathrm{g}} = 0.94$ mm, the hole diameter $d = 2.4$ mm and the pitch of the hole array $\Lambda = 8$ mm.

5.4.1 Simulated Transmittance

Figure 5.12 shows the transmission relationship between plate thickness and frequency for a two to one (5.12(a)) and a three to one (5.12(b)) plate ratio simulated using the MM method. The ratio is such that h_{p1} corresponds to the thickness of the thin plate and h_{p2} corresponds to the thick plate.

In the case of a two to one plate thickness ratio there is a mode crossing for every three modes rather than every two as for the equal thickness plates. For the three to one plate thickness ratio, the mode crossing occurs for every four modes. Unlike the equal thickness plate case where all the even-order modes were unperturbed by the gap the relationship is now more complicated. With reference to the analytic model of a single open-ended pipe with a side-branch at its mid point used to analyse the DF structure previously, the two to one ratio is equivalent to having a side-branch a third of the way along the pipe. The first and second modes will be perturbed by the presence of the gap while the third mode which possesses a pressure node at the position of the gap is largely unaffected. Higher order modes will be similarly unaffected by the gap when a pressure node lies at its position. Similarly when the ratio is three to one the situation is equivalent to a single pipe with a side branch a quarter of the way along the pipe. In this case modes possessing a pressure node a quarter of the way along the pipe will

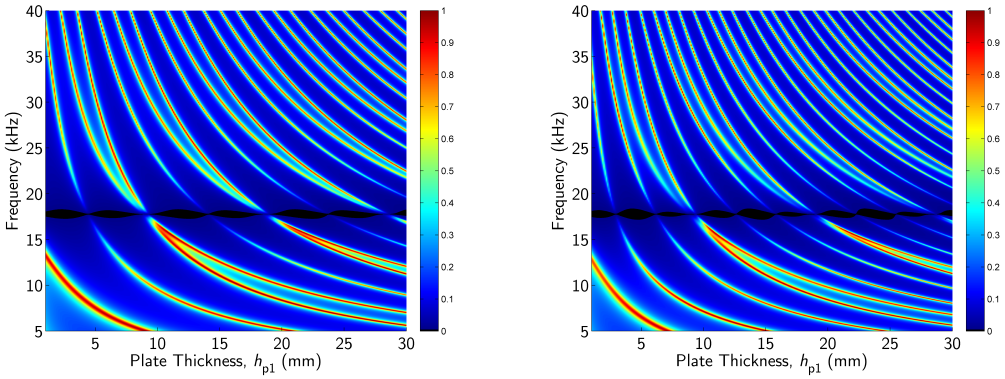

(a) $2h_{\mathrm{p1}} = h_{\mathrm{p2}}$ (b) $3h_{\mathrm{p1}} = h_{\mathrm{p2}}$

Figure 5.12: Modelled data of the transmission through the DF structure where the ratio of the plate thickness $h_{\mathrm{p1}} : h_{\mathrm{p2}}$ is (a) 1:2 and (b) 1:3.

be unperturbed by the gap, in other words every fourth mode will be unperturbed.

5.4.2 Experimental Transmittance

The acoustic transmittance through three DF structures with plates of unequal thickness has been measured experimentally using the collimated beam arrangement described in section (4.2.3). The three samples consist of 200 mm × 200 mm perspex plates with thickness $h_{\mathrm{p}} = 2.97$ mm, 5.96 mm and 12 mm. Each plate is perforated with a square array of holes with radius $d = 2.4$ mm and pitch $\Lambda = 8$ mm. Pairs of plates are combined to make DF structures with (a) $h_{\mathrm{p1}} = 2.97$ mm, $h_{\mathrm{p2}} = 5.94$ mm, (b) $h_{\mathrm{p1}} = 2.97$ mm, $h_{\mathrm{p2}} = 12$ mm and (c) $h_{\mathrm{p1}} = 5.94$ mm, $h_{\mathrm{p2}} = 12$ mm.The plates comprising each pair were clamped together with a separation of 0.94 mm corresponding to the thickness of two metal washers. Figure 5.13 shows the experimental data (blue line) compared with FEM modelling of each structure (red line). The data is in good agreement and confirms that the stop-band remains unaffected by variations of the position of the gap within a long pipe of length $h_{\mathrm{p1}} + h_{\mathrm{p2}}$.

5.5 Concluding Remarks

In this chapter the acoustic transmittance of rigid plates that have been perforated with a square array of holes has been investigated both numerically and experimentally. The SF was shown to exhibit a series of transmission peaks at frequencies corresponding to the excitation of pipe resonances. The DF was shown to exhibit a similar family of transmission peaks associated with the excitation of pipe resonances at frequencies

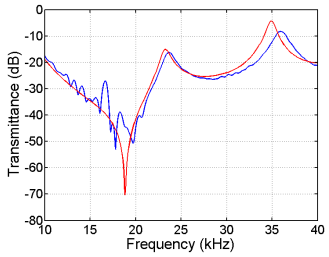

(a) $h_{p1} = 2.97$ mm, $h_{p2} = 5.94$ mm

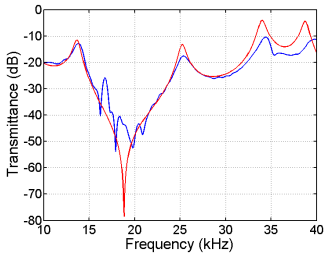

(b) $h_{p1} = 2.97$ mm, $h_{p2} = 12$ mm

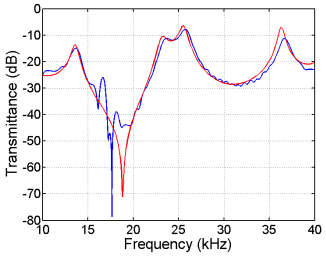

(c) $h_{p1} = 5.94$ mm, $h_2 = 12$ mm

Figure 5.13: Experimental data of the transmission through the DF structure for the cases of (a) $h_{p1} = 2.97$ mm, $h_{p2} = 5.94$ mm, (b) $h_{p1} = 2.97$ mm, $h_{p2} = 12$ mm and (c) $h_{p1} = 5.94$ mm, $h_2 = 12$ mm.

determined by the total thickness of the structure. While the even-order modes are unperturbed by the gap between the plates, the odd-order modes are shifted in frequency from where they would be expected to lie in the absence of the gap. In addition to the transmission peaks, an acoustic stop-band corresponding to the excitation of a resonant mode of the gap was shown and demonstrated to be unaffected by the thickness of the plates. Allowing one of the plates to vary in size from the other, which is equivalent to shifting the position of a resonant side branch along a single long pipe, similarly has no effect on the frequency of the stop-band.

Chapter 6

Controlling the Stop-band of the Double Fishnet Structure

6.1 Introduction

The double fishnet structure (DF) (figure 6.1) was shown in the preceding chapter to possess a stop-band at a frequency determined by the resonant frequency of the gap. Changing the pitch Λ of the structure allows the frequency of the stop-band to be trivially shifted, however in practice this isn't likely to be practical and prevents simple tuning of the stop-band once the structure has been machined. In this chapter we explore the effects of the changing angle of incidence θ, varying the plate misalignment h_{off} and altering the gap size h_{g}.

6.2 Acoustic Transmittance of the Double Fishnet as a Function of Incident Angle

Here the effect of varying the incident angle θ on the acoustic transmittance of the DF is investigated. Prior modelling suggests that the stop-band is largely unaffected by the varying angle of incidence [36].

6.2.1 Simulated Transmittance

The modal matching (MM) method (appendix B) is used to simulate the transmittance of a DF with plate thickness $h_{\text{p}} = 12$ mm, hole pitch $\Lambda = 8.00$ mm, hole diameter $d = 2.40$ mm and gap size $h_{\text{g}} = 0.94$ mm. Figure 6.2(a) shows the results of this modelling plotted as f against the wave vector k_x where k_x relates to the angle of incidence through $k_x = k_0 \sin(\theta)$. Dispersion of the pipe modes with the angle of incidence is

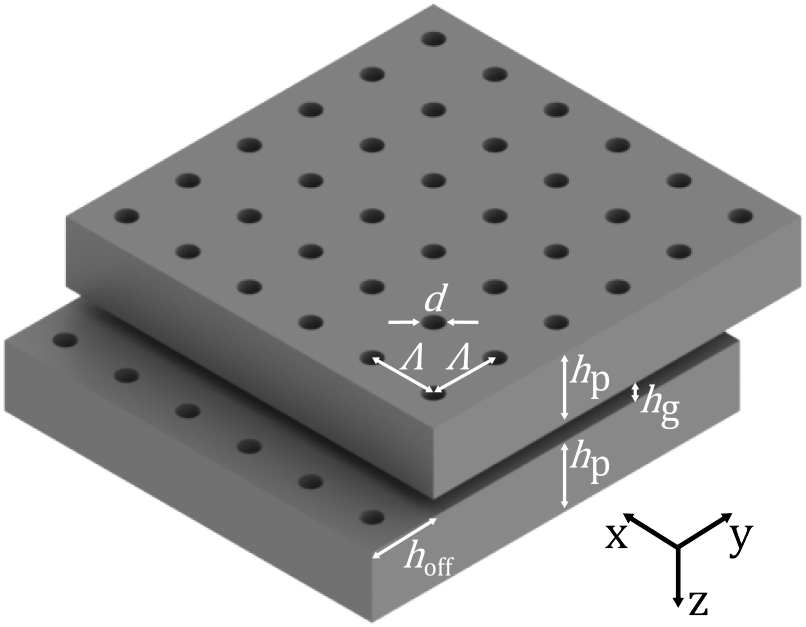

Figure 6.1: Schematic drawing of the DF structure consisting of a pair of rigid plates perforated with a periodic square array of circular holes.

clearly seen. The stop-band shifts up in frequency slightly and narrows as θ is increased. A second stop-band relating to the second order mode of the gap can be seen appearing at high angles of incidence.

6.2.2 Experimental Study of the Effect of Incident Angle

Experimental data was taken for a sample identical to the previously modelled DF using the transmission kit (section 4.2.3) and the continuous wave method described in 4.4.1. The sample is rotated about the x axis to vary to angle of incidence (N.B. Rotation about the y axis would have the same effect). The range of incident angles is varied between 0° and 45°. Data at higher angles could not be obtained due to the effective decrease in the size of the experimental sample. Figure 6.2(b) shows the experimentally recorded data. The dispersion of the pipe modes are in agreement across the measured range although the strength of transmission is considerably weaker due to the effect of viscous losses which are not included in the MM modelling. The sensitivity of the experiment to low levels of transmission in the region of the stop-band makes it difficult to verify how the stop-band is affected by the angle of incidence.

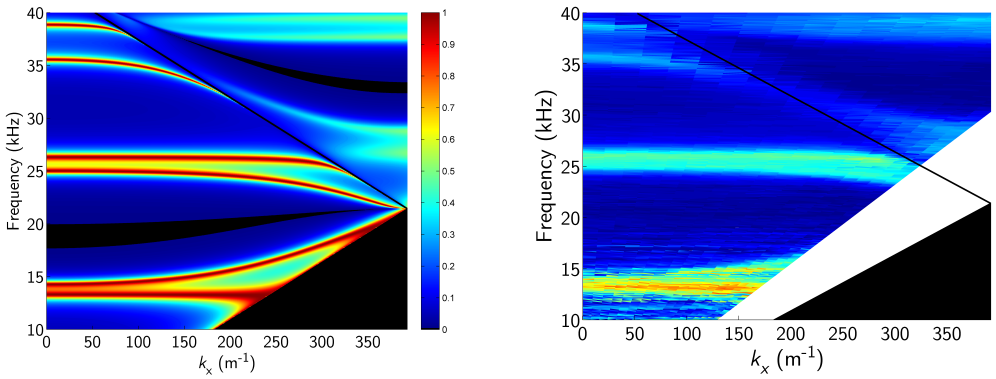

(a) (b)

Figure 6.2: (a) MM modelled dispersion of the DF with pitch $\Lambda = 8.00$ mm, plate thickness $h_p = 12.00$ mm and gap size $h_g = 0.94$ mm. (b) Experimentally determined dispersion of the DF out to 45° where the limited size of the sample prevented data being obtained at higher angles.

6.3 Effect of Misalignment on the Acoustic Stopband

Here we consider the effect that misalignment of the holes by a distance h_{off} has on the acoustic transmittance. The parameter h_{off} refers to the shortest distance between two misaligned holes.

6.3.1 Simulated Transmittance

The acoustic transmittance of the structure is simulated using the MM technique described in appendix B. Figure 6.3 shows the simulated transmittance as a function of both a diagonal offset (figure 6.3(a)) and a lateral offset (figure 6.3(b)) up to the edge of a unit cell of the DF. As the plates are progressively offset the stop-band is shifted up in frequency. As well as shifting the stop-band, pairs of pipe modes can be seen to converge at the point where the modes cross the stop-band. The frequency shift of the stop-band is almost identical for the case of both lateral and diagonal offsets. Comparison can be made between the values of h_{off} at which the stop-band crosses the pipe modes, at 1.8 mm (25 kHz) and 2.5 mm (37 kHz) for the case of diagonal offset, and at 1.8 mm and 2.7 mm for the case of lateral offset.

6.3.2 Analytical Model of Effect of Misalignment

To elucidate this behaviour an approximate analytical model was developed following a similar procedure to that used for the aligned plates (section 5.3.2). A square unit cell is chosen centred on a hole in the input side of the plate. The acoustic pressure in

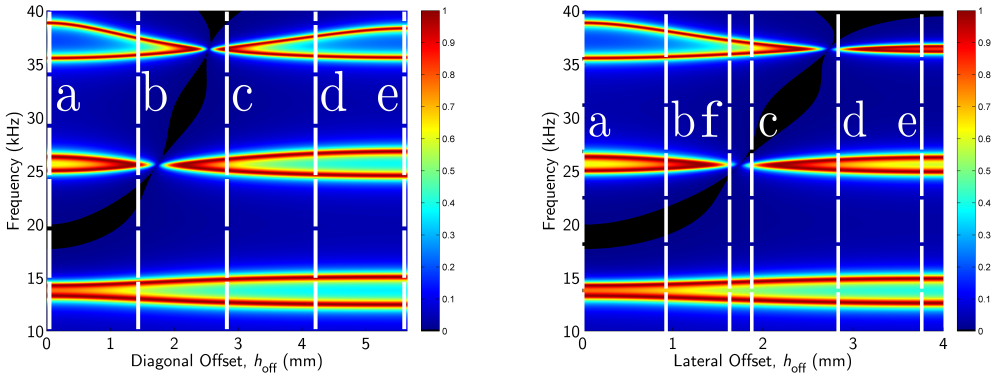

(a) (b)

Figure 6.3: MM modelled transmission spectra of the DF structure as a function of the (a) diagonal and (b) lateral offset h_{off}. Black regions indicate less than -46 dB (0.05%) transmission. The pitch of the hole array $\Lambda = 8.00$ mm, the hole diameter $d = 2.40$ mm and the plate thickness $h_{\text{p}} = 12.00$ mm.

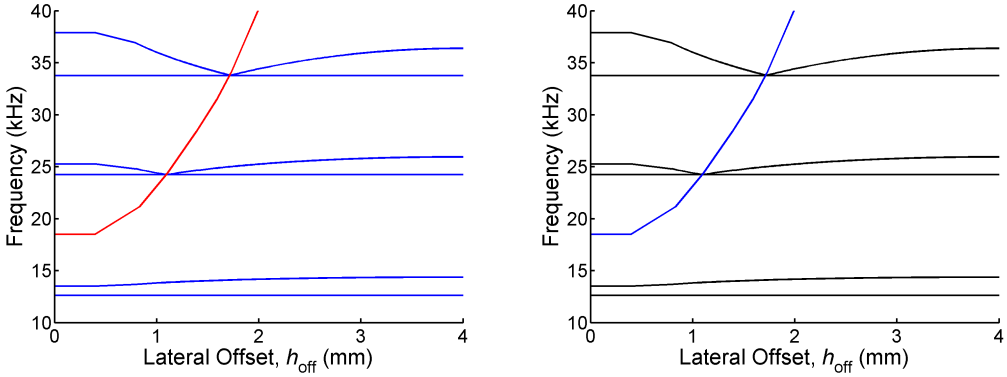

(a) (b)

Figure 6.4: Transmission modes (solid lines) and acoustic stop-band (dashed lines) calculated from the analytical model, (a) diagonal offset and (b) lateral offset.

the gap is approximated as a sum of zero-order Bessel functions, centred on the input hole, of the form

$$p(r) = AJ_0(kr) + BY_0(kr), \tag{6.1}$$

where A and B are constants, k is the wave-number, and r is the distance from the center of the input hole. The symmetry of the unit cell forces an anti-node at the square boundary, which is difficult to model using circular wavefronts, hence for simplicity the acoustic pressure field is assumed to have square wave fronts in the $x - y$ plane within the gap region. At any particular frequency, the ratio of A and B is determined by the

requirement for a pressure anti-node at the edge of the unit cell. Transmission through the structure is determined by the amplitude of this pressure field at the position of the output hole, with the condition for zero transmission being that the acoustic pressure in the gap exhibits a nodal line that runs through the position of the output hole. As observed in the modelling of the aligned plates, for $h_{\text{off}} = 0$ mm, the nodal line is assumed to lie at $r = 0.6$ mm; for $h_{\text{off}} \geq 1.2$ mm, the nodal line is at $r = h_{\text{off}}$; the range $0 < h_{\text{off}} < 1.2$ mm is handled by interpolation. Under this condition there is no field excited in the output hole in much the same way that the even-order modes of the aligned structure do not excite fields in the gap. As the offset of the plates is increased, the distance between the output hole and the unit-cell boundary is decreased and hence a shorter distance between the nodal line and the boundary anti-node is required, and hence a higher frequency. This is approximately equivalent to setting the wavelength to $\frac{\lambda}{4} = \sqrt{2}\frac{\Lambda}{2} - h_{\text{off}}$.

In addition to being used to model the variation of the stop-band frequency with hole offset, the analytical model can estimate shifts in the frequency of the pipe modes. The frequencies of the modes at $h_{\text{off}} = 0$ mm are determined as in section 5.3.2. The lower mode of each pair is assumed to be fixed in frequency, i.e., unaffected by varying h_{off}, (although by looking at the MM simulations in figure 6.3 this is clearly a simplification) and the splitting between the modes is then assumed to be proportional to the strength of the coupling between the holes in one plate and the holes in the other. The coupling strength is determined by the amplitude of the pressure field in the gap region at the centre of the output hole. This pressure field is of the form given in equation 6.1, calculated at the fixed mode frequency of each pair and choosing the ratio of A and B to satisfy the condition of an anti-node at the unit cell boundary. The coupling strength falls to zero at the stop-band frequency and hence the splitting is zero. We assume that the sound field is not defined for $r < 0.6$ mm; for $h_{\text{off}} = 0$ mm the splitting is determined from the sound field at $r = 0.6$ mm; for $h_{\text{off}} \geq 1.2$ mm the splitting is determined from the sound field at $r = h_{\text{off}}$; the splitting in the range $0 < h_{\text{off}} < 1.2$ mm is obtained by interpolation.

Figure 6.4 shows the predictions of this approximate analytical model for the cases of a diagonal offset (figure 6.4(a)) and a lateral offset (figure 6.4(b)). Despite the approximations involved in the analytic model there is good agreement between the MM data for the case of diagonal misalignment and the corresponding analytic modelling. Comparing the offsets at which the stop-band coincides with the pipe modes in the MM simulation (figure 6.3(a)) gives $h_{\text{off}} = 1.7$ mm and 2.5 mm; the equivalent offsets from the analytic model (figure 6.4(a)) gives $h_{\text{off}} = 1.6$ mm and 2.5 mm. The case of lateral misalignment shows less agreement between the MM data and the results from the analytical model. Comparing the offsets at which the stop-band coincides

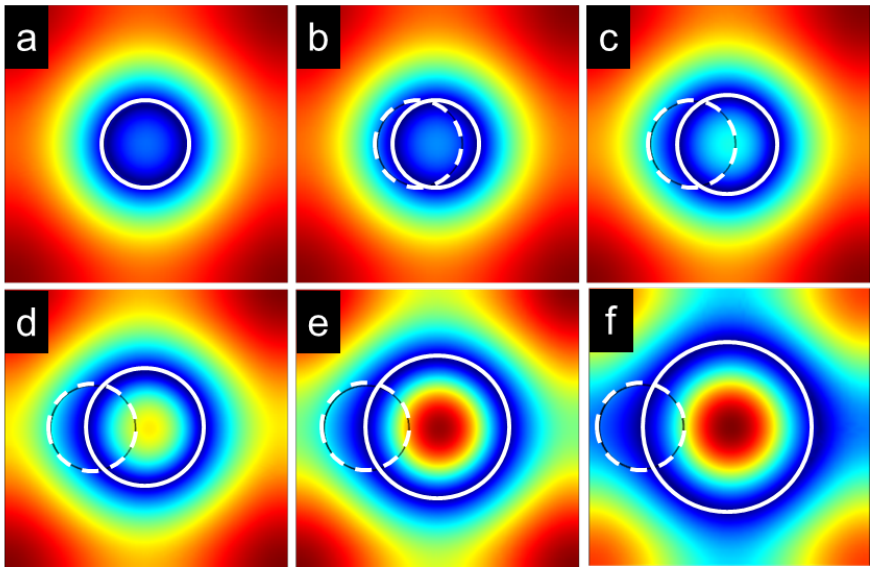

Figure 6.5: Time-averaged pressure profiles in an xy-plane through the centre of a gap $h_g = 0.94$ mm. The profiles are taken at the stop-band frequencies for offsets of h_{off} = (a) 0 mm, (b) 0.5 mm, (c) 1.0 mm, (d) 1.5 mm, (e) 2.0 mm and (f) 2.5 mm.

with the pipe modes in the MM data (figure 6.3(b)) gives $h_{off} = 1.7$ mm and 2.7 mm; the equivalent offsets in the analytical model (figure 6.4(b) occur at $h_{off} = 1.1$ mm and 1.8 mm. The corresponding values of h_{off} differ by a factor of approximately 1.50 in this case. The difference between the diagonal and lateral cases arises because of the assumption in the analytical model that the pressure field in the gap has square wavefronts and hence square nodal lines. FEM modelling of the time-averaged pressure within the gap reveal the nodal lines to be approximately circular. Figure 6.5 shows FEM plots of the time-averaged pressure field in the xy-plane at the center of the gap region for lateral offsets of h_{off} = (a) 0 mm, (b) 0.5 mm, (c) 1 mm, (d) 1.5 mm, (e) 2 mm and (f) 2.5 mm. The fields are shown at the stop-band frequency corresponding to each value of h_{off}. Each plot is centred on the input hole and it can be seen that a pressure node (marked by a solid white circle) runs through the position of the output hole (marked by a dashed white circle). As the output hole lies over the pressure node it can be shifted along the nodal line around the input hole without affecting the profile of the pressure field within the gap. Hence a lateral offset of $h_{off} = 1$ mm will give the same response as a diagonal offset of $h_{off} = 1$ mm.

6.3.3 Experimental Study of the Effect of Plate Misalignment

In the corresponding experimental studies we explore the transmittance of a DF as a function of diagonal and lateral misalignment using the transmission set-up (section

4.2.3). The DF studied has a plate thickness $h_p = 12$ mm, hole pitch $\Lambda = 8$ mm, hole diameter $d = 2.4$ mm and gap size $h_g = 0.94$ mm. To allow the sample plates to be misaligned the solid material between two diagonally or laterally adjacent holes in each corner of one of the plates is machined out. The slots that are formed allow the plates to be slid diagonally or laterally by one unit cell.

6.3.3.1 Diagonal Misalignment

Figure 6.6 shows experimental data (blue lines) and FEM modelled data (red lines) for diagonal offsets corresponding to integer steps of 1.42 mm (i.e. 1 mm in x and y) from $h_{off} = 0$ mm up to the edge of the unit cell. The values of h_{off} correspond with the dashed lines in figure 6.3(a). Experimental and modelled data accord well with each other and the shift of the stop-band is clearly seen from panels 6.6(a) and 6.6(b).

6.3.3.2 Lateral Misalignment

Figure 6.7 shows experimental data (blue lines) and FEM modelled data (red lines) for lateral offsets corresponding to integer steps of 1 mm from $h_{off} = 0$ mm up to the edge of the unit cell. An additional lateral offset of $h_{off} = 1.74$ mm is recorded, corresponding to the offset at which the stop-band coincides with a pair of pipe modes at approximately 25 kHz. The values of h_{off} correspond with the dashed lines in figure 6.3(b). Experimental and modelled data accord well with each other; the shift of the stop-band is clearly seen from panels 6.7(a)-6.7(d) and the additional offset of $h_{off} = 1.7$ mm clearly shows the suppression of the pipe modes when the stop-band coincides with them.

6.4 Effect of Gap Size on the Acoustic Stopband

We now turn our attention to the effect the gap size h_g has on the stop-band while the hole in the plate are aligned. It has been suggested that the bandwidth of the stop-band can be easily tailored by varying the gap size [36]. While this is valid for small values of h_g, we explore what happens to the stop-band as the gap size is increased beyond the range considered previously. Figure 6.8 shows the simulated transmittance of a DF with pitch $\Lambda = 8$ mm, hole diameter $d = 2.4$ mm and plate thickness $h_p = 12$ mm determined using the MM method (appendix B). The black region indicates the stop-band which has been defined as less than -46 dB (0.5% amplitude transmission). As h_g is increased from $h_g = 0$ mm to approximately $h_g = 1$ mm the width of the stop-band increases. However, as h_g is increased beyond $h_g = 1$ mm the frequency of

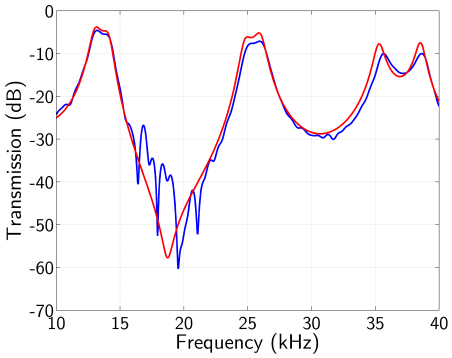

(a) $h_{\text{off}} = 0$ mm

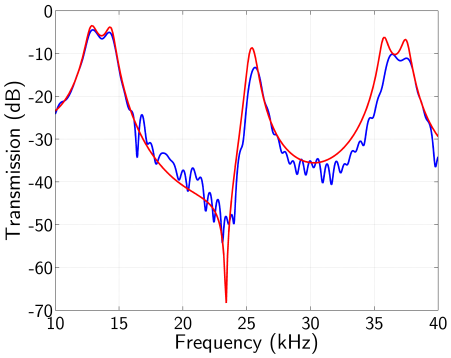

(b) $h_{\text{off}} = 1.4$ mm

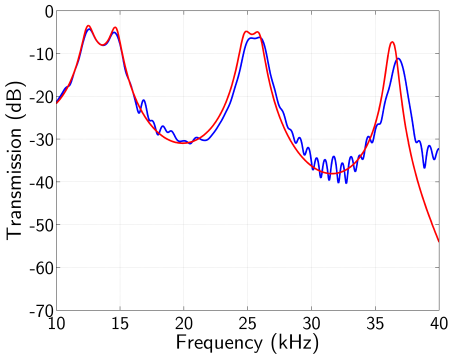

(c) $h_{\text{off}} = 2.8$ mm

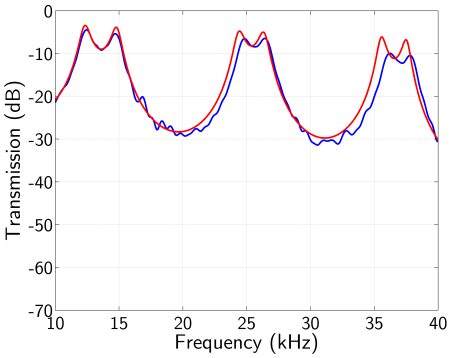

(d) $h_{\text{off}} = 4.2$ mm

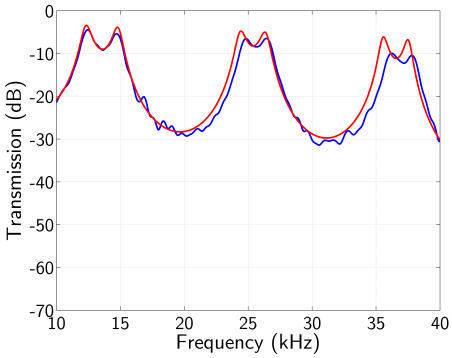

(e) $h_{\text{off}} = 5.6$ mm

Figure 6.6: Experimental (blue lines) and modelled (red lines) transmission data for the DF structure diagonal offsets of $h_{\text{off}} =$ (a) 0 mm, (b) 1.4 mm, (c) 2.8 mm, (d) 4.2 mm, (e) 5.6 mm.

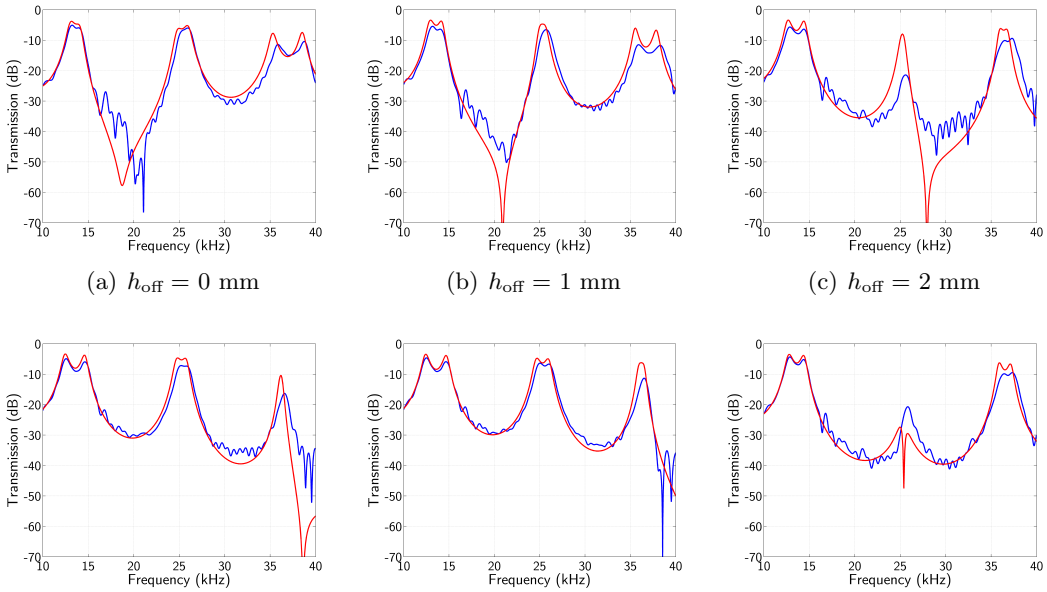

(a) $h_{\text{off}} = 0$ mm (b) $h_{\text{off}} = 1$ mm (c) $h_{\text{off}} = 2$ mm

(d) $h_{\text{off}} = 3$ mm (e) $h_{\text{off}} = 4$ mm (f) $h_{\text{off}} = 1.7$ mm

Figure 6.7: Experimental (blue lines) and modelled (blue lines) transmission data for the DF structure lateral offsets of h_{off} = (a) 0 mm, (b) 1 mm, (c) 2 mm, (d) 3 mm, (e) 4 mm and (f) 1.7 mm.

the stop-band is shifted upwards. The shift in frequency bears a strong resemblance to the shift observed when the plates are misaligned (section 6.3).

When $h_{\text{g}} = 0$ mm the structure resembles an array of open-ended pipes of length $2h_{\text{p}}$ and when $h_{\text{g}} \to \infty$ the structure resembles two uncoupled plates, each consisting of an array of open-ended pipes of length h_{p}. The modes of these two systems are readily determined from equation (2.29). It is apparent that there will be twice as many modes for $h_{\text{g}} = 0$ mm than when $h_{\text{g}} \to \infty$. Therefore pairs of pipe modes are expected to converge as h_{g} increases. However, figure 6.8 shows a more complicated picture. At large gap sizes there is unusual behaviour exhibited whereby some of the modes are shifted downwards in frequency and appear to change order. For example, at $h_{\text{g}} \approx 5$ mm and ≈ 7 mm three modes can be seen within a narrow frequency band. This behaviour is explained in section 6.5.

6.4.1 Analytic Modelling of the Effect of Gap Size

Three analytical models are used to understand the behaviour of the modes and the stop-band as a function of the gap size h_{g}; (1) for small values of h_{g} the system resembles that of the DF described previously in section 5.3 where the mode frequencies are determined by the pipe resonances of an open-ended pipe with a resonant side-branch

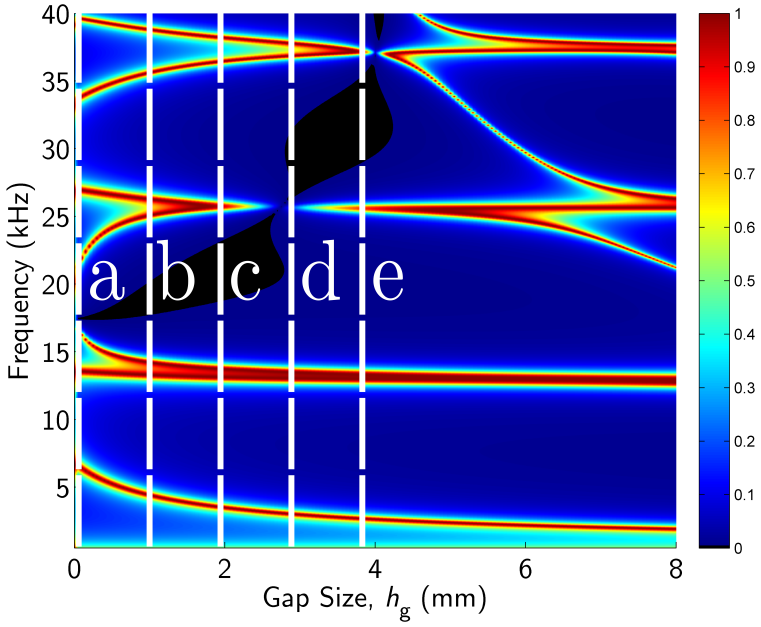

Figure 6.8: MM modelled transmission spectra of the DF structure as a function of the gap size h_g. Black indicates less than -46 dB transmission, red represents high transmission. The pitch of the hole array is $\Lambda = 8$ mm, the hole diameter is $d = 2.4$ mm and the plate thickness is $h_p = 12$ mm. The dashed white lines labelled a-e correspond to the experimental data in figure 6.12

at its mid-point; (2) for larger values of h_g, in each unit cell the hole-gap-hole system can be modelled as a pipe of varying cross-section whose resonance frequencies are calculated below, followed by an outline of (3) modelling of the stop-band in terms of the three dimensional pressure field in the gap.

Consider a pipe of length h_T where $h_T = 2h_p + h_g + \Delta L$ (where ΔL is the end correction associated with the hole termination) running from $z = -\frac{h_T}{2}$ to $z = \frac{h_T}{2}$ taking the form of a pipe of cross-section S_2 joined to a larger pipe of cross-section S_1 joined to a pipe of cross-section S_2 as in figure 6.9. The characteristic acoustic impedance of each pipe is given by $Z_n = \frac{\rho_0 c}{S_n}$ and this impedance relates to the pressure p and the volume velocity U via $Z = \frac{p}{U}$. The boundary condition at the effective pipe end gives $z = 0$ at $z = \frac{h_T}{2}$ and the symmetry of the system gives $p = 0$ at $z = 0$ for even-order modes and p is a maximum at $z = 0$ for odd-order modes.

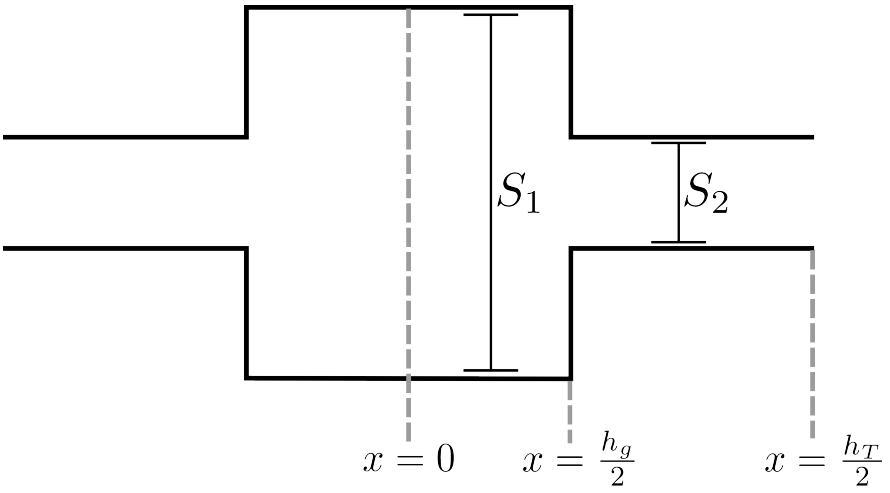

Figure 6.9: Schematic diagram of the pipe geometry used to analyse the transmittance of the DF at large values of h_{g}.

6.4.1.1 Even-order Modes

To satisfy the boundary conditions at $z = 0$ and $z = \frac{h_{\mathrm{T}}}{2}$ the pressure field p is described by p_1 for $0 \leq z \leq \frac{h_{\mathrm{g}}}{2}$ and p_2 for $\frac{h_{\mathrm{g}}}{2} \leq z \leq \frac{h_{\mathrm{T}}}{2}$.

$$p_1 = A \exp\left[i\omega t\right] \sin\left(\frac{\omega}{c} z\right), \tag{6.2a}$$

$$p_2 = B \exp\left[i\omega t\right] \sin\left(\frac{\omega}{c}\left(z - \frac{h_{\mathrm{T}}}{2}\right)\right). \tag{6.2b}$$

From which the equations U_1 and U_2 for the volume velocity can be obtained.

$$U_1 = i\frac{A}{Z_1} \exp\left[i\omega t\right] \cos\left(\frac{\omega}{c} z\right), \tag{6.3a}$$

$$U_2 = i\frac{B}{Z_2} \exp\left[i\omega t\right] \cos\left(\frac{\omega}{c}\left(z - \frac{h_{\mathrm{T}}}{2}\right)\right). \tag{6.3b}$$

Combining these equations and matching p and U at $z = \frac{h_{\mathrm{g}}}{2}$ gives

$$S_1 \cot\left(\frac{\omega}{c}\frac{h_{\mathrm{g}}}{2}\right) = -S_2 \cot\left(\frac{\omega}{c}\left(\frac{h_{\mathrm{T}}}{2} - \frac{h_{\mathrm{g}}}{2}\right)\right), \tag{6.4}$$

which can be rewritten as

$$\tan\left(\alpha X\right) = -\frac{S_1}{S_2} \tan\left(X\right), \tag{6.5}$$

where $\alpha = \frac{h_g}{2h_p+\Delta l}$ and $X = \frac{\omega}{c}(h_p + \Delta l)$. Solving for X at various values of α determines the frequencies of the even-order modes for various values of h_g.

6.4.1.2 Odd-order Modes

To satisfy the boundary conditions at $z = 0$ and $z = \frac{h_T}{2}$ the pressure field p is described by p_1 for $0 \leq z \leq \frac{h_g}{2}$ and p_2 for $\frac{h_g}{2} \leq z \leq \frac{h_T}{2}$.

$$p_1 = A \exp[i\omega t] \cos\left(\frac{\omega}{c} z\right), \tag{6.6a}$$

$$p_2 = B \exp[i\omega t] \sin\left(\frac{\omega}{c}\left(z - \frac{h_T}{2}\right)\right). \tag{6.6b}$$

From which the equations for the volume velocity can be obtained

$$U_1 = i\frac{A}{Z_1} \exp[i\omega t] \sin\left(\frac{\omega}{c} z\right), \tag{6.7a}$$

$$U_2 = i\frac{B}{Z_2} \exp[i\omega t] \cos\left(\frac{\omega}{c}\left(z - h'_p\right)\right). \tag{6.7b}$$

Combining these equations and matching p and U at $z = \frac{h_g}{2}$ gives

$$S_1 \tan\left(\frac{\omega}{c}\frac{h_g}{2}\right) = S_2 \cot\left(\frac{\omega}{c}\left(\frac{h_T}{2} - \frac{h_g}{2}\right)\right), \tag{6.8}$$

which can be rewritten as

$$\tan(\alpha X) = \frac{S_2}{S_1} \cot(X), \tag{6.9}$$

where α and X are as above. Solving for X at various values of α determines the frequencies of the odd-order modes for various values of h_g.

Equation (6.9) has a solution for $X \ll 1$ which satisfies $\alpha X = \frac{S_2}{S_1}\frac{1}{X}$. Rearranging for X gives $X^2 = \frac{S_2}{\alpha S_1}$ and substituting for α and X to solve for f gives equation (6.10) which is the form of a Helmholtz resonance (section 2.4.3) with the plate holes (in parallel) acting as the neck and the gap acting as the volume compliance.

$$f = \frac{c}{2\pi}\sqrt{\frac{2S_2}{(h_p + \Delta l)(h_g S_1)}}. \tag{6.10}$$

To calculate the frequency of the stop-band requires a third model which draws inspiration from the model used to calculate the stop-band frequency for the case of misaligned plates (section 6.3.2). A three-dimensional model of the sound field in the gap is used based on the assumption that the acoustic pressure in the central plane of

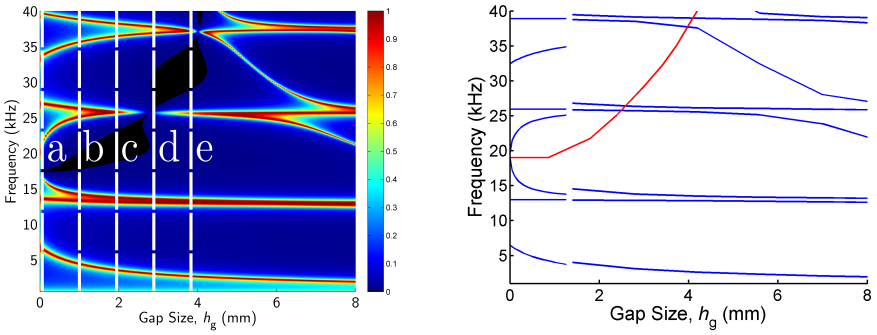

(a) (b)

Figure 6.10: (a)Repeat of figure 6.8 to facilitate comparison. (b) Combined plot of the transmission modes (solid lines) and acoustic stop-band (dashed lines) calculated from the three analytical models.

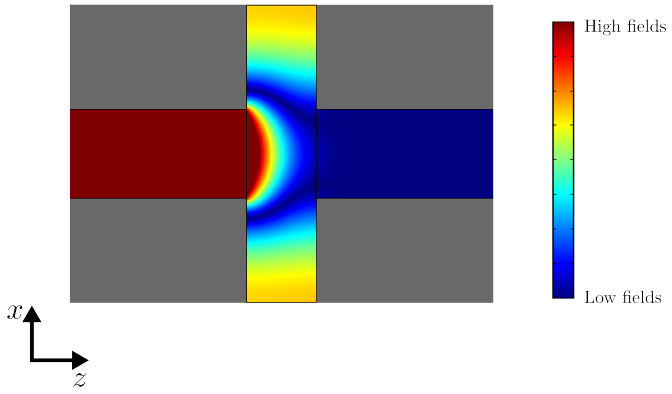

Figure 6.11: Time-averaged pressure field at the frequency of the acoustic stop-band on a plane through the centre of the unit cell.

the gap (i.e., mid-way between the plates) can be expanded as a sum Bessel functions of zero-order, as before. It is further assumed that the principal nodal line in this plane extends into the output half of the gap as a nodal surface with a hemispherical profile. The condition for a transmission minimum is that the nodal surface lies at the entrance to the output hole, i.e., the radius of the hemispherical profile is equal to half the plate separation h_g. On the central plane of the gap, this condition fixes the position of the nodal line in relation to the pressure antinode at the edge of the unit-cell. As the plate separation is increased, a shorter distance between the nodal line and the antinode, and hence a higher frequency, is required to achieve a transmission minimum. This is approximately equivalent to setting the wavelength to $\lambda = 4\left(\frac{\sqrt{2}\Lambda}{2} - \frac{h_g}{2}\right)$.

Figure 6.10 shows the frequencies of the stop-band (dashed line) and the pipe modes

(solid lines) predicted by these three analytical models. There has been no attempt made to model the interaction between the stop-band and the pipe modes. Additionally, no attempt has been made to join the two models used to calculated the pipe modes for smaller and larger gap sizes. Given the relative simplicity of the models and the assumptions made it is remarkable that the analytic models show agreement with the MM model (figure 6.8) and that the two models used to predict the pipe mode frequencies can almost be joined up. As previously noted, the utility of the analytical modelling is that it explicitly indicates the nature of the various resonances and anti-resonances. For example, it shows that the 'extra' resonance, observed in addition to the equally spaced pipe modes at $h_g = 0$, originates at the frequency of the stop band. To observe the shape of the nodal surface within the gap at the frequency of the stop-band FEM modelling is used to plot the time-averaged pressure field in the yz-plane through the centre of the unit cell. Figure 6.11 shows this for a gap size of $h_g = 3.5$ mm at a frequency of 32.5 kHz. A pressure node (deep blue) can be seen at the entrance to the output hole however the nodal surface clearly has a more complex shape than the hemi-spherical surface assumed in the analytical model. While the shape of the nodal surface is not hemispherical, the FEM modelling confirms that the stop-band occurs when a node in the time-averaged pressure field coincides with the output hole.

6.4.2 Experimental Study of the Effect of Gap Size

In the corresponding experimental studies the transmittance at different values of h_g have been measured for a DF with plate thickness $h_p = 12$ mm, hole pitch $\Lambda = 8$ mm and hole diameter $d = 2.4$ mm. The plate separation is varied from 0 mm to 3.76 mm in integer steps of 0.94 mm corresponding to the white dashed lines labelled (a)-(e) on figure 6.8. Figure 6.12 shows the experimentally determined transmittance (blue line) of the DF structure for $h_g =$ (a) 0.94 mm, (b) 1.88 mm, (c) 2.82 mm and (d) 3.76 mm. The experimental data accords with the FEM modelling data (red line).

6.5 Acoustic Triple Mode

It was previously mentioned that at larger gap sizes the pipe modes exhibit unusual behaviour whereby some of the modes appear to shift down in frequency and change order (figure 6.13(a), the region of interest is highlighted by the the white box. The same behaviour is observed in the analytical treatment (figure 6.10). To understand the origins of this frequency shift we simulate the transmittance of a structure with $\Lambda = 3$ mm and $d = 0.45$ mm. The shorter pitch shifts the stop-band up in frequency leaving the lower frequency pipe modes unperturbed and the reduced hole diameter

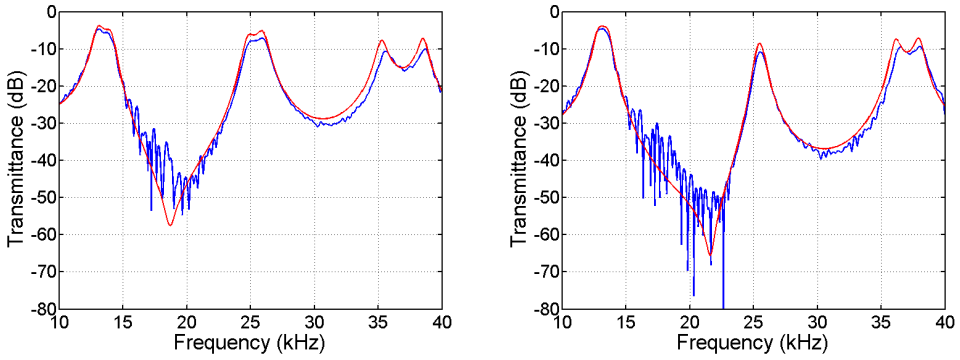

(a) $h_g = 0.94$ mm (b) $h_g = 1.88$ mm

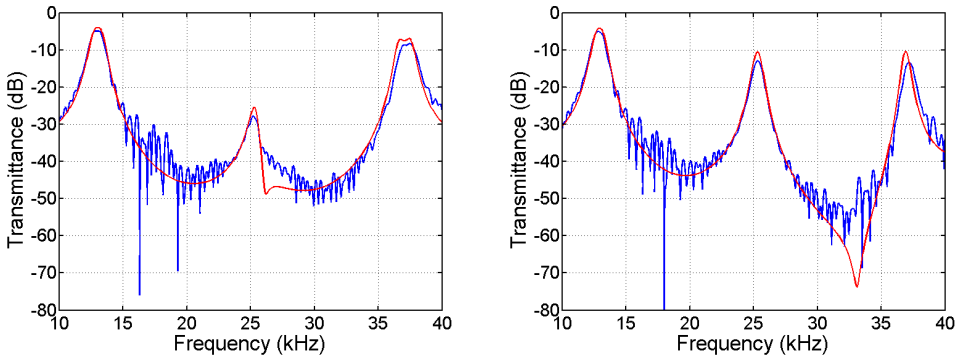

(c) $h_g = 2.82$ mm (d) $h_g = 3.76$ mm

Figure 6.12: Experimental (blue line) and FEM modelled (red line) transmission data for the DF structure at gap sizes h_g = (a) 0.94 mm, (b) 1.88 mm, (c) 2.82 m and (d) 3.76 mm.

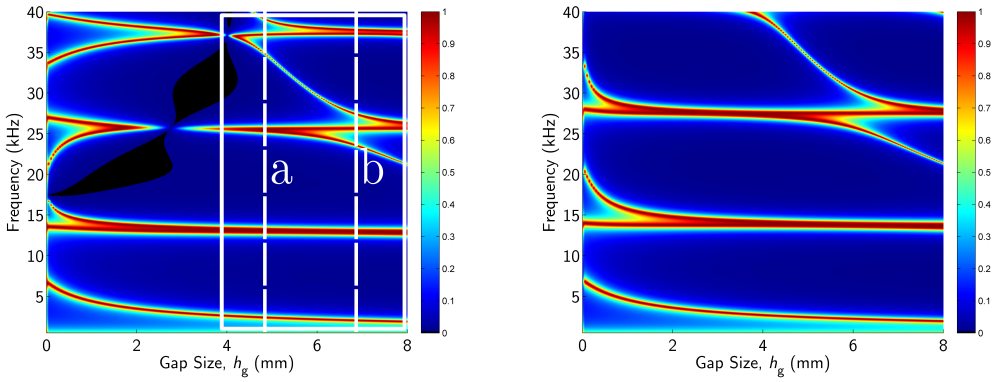

(a) (b)

Figure 6.13: MM modelled transmission spectra of the DF structure as a function of the gap size h_g. (a) Plate thickness $h_p = 12$ mm, hole diameter $d = 2.4$ mm and pitch $\Lambda = 8$ mm. (b) Plate thickness $h_p = 12$ mm, hole diameter $d = 0.45$ mm and pitch $\Lambda = 3$ mm.

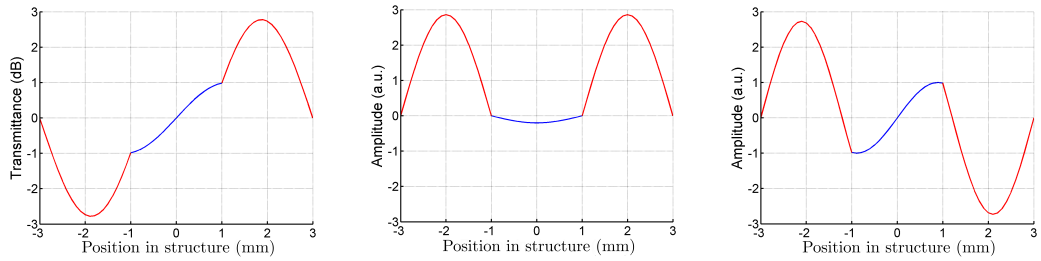

(a) (b) (c)

Figure 6.14: Analytic prediction of the instantaneous pressure field for each of the three resonances seen around $f = 25$ kHz for a gap size $h_g = 6.8$ mm.

maintains the percentage of the unit cell which is perforated. Figure 6.13(b) shows the results of this analysis. At $h_g = 0$ mm we can see the expected modes of a single plate of thickness $2h_p$. Increasing h_g has little effect on the even-order modes while the odd-order modes appear to ecrease in frequency to converge with the even-order modes at the expected frequencies of a single plate of thickness h_p. At larger values of h_g we again see the same unusual behaviour whereby some of the modes appear to shift down in frequency. The similarity between both cases suggests that the behaviour is associated with the gap size.

To understand the behaviour we consider the modes described by equations 6.4 and 6.8. The apparent downward shift in frequency corresponds to the mode in the z axis of the gap i.e. the mode that would exist between two parallel, partial mirrors corresponding to $\lambda = 2h_g$. This mode originates at infinite frequency when $h_g = 0$ mm and decreases in frequency as h_g is increased. As the additional mode decreases in frequency it couples to the pipe modes of the DF and the triple mode behaviour exhibited in figure 6.13 is obtained.

The analytical model previously described allows the fields of the three modes to be explicitly described. Figure 6.14 shows the instantaneous pressure fields of the three modes observed around 25 kHz for a gap size $h_g = 6.8$ mm.

6.5.0.1 Experimental Evidence of the Triple Mode

Figure 6.15 plots the experimental transmittance of the DF at gap sizes of (a) $h_g = 4.8$ mm and (b) $h_g = 6.8$ mm corresponding to the white dashed lines in figure 6.13(a). For each case the experimental transmittance of the DF structure (blue line) shows the three peaks associated with the triple mode. The experimental data accords with FEM modelling of the structure (red line) except in regions of low transmittance where the ratio of signal-to-noise is low.

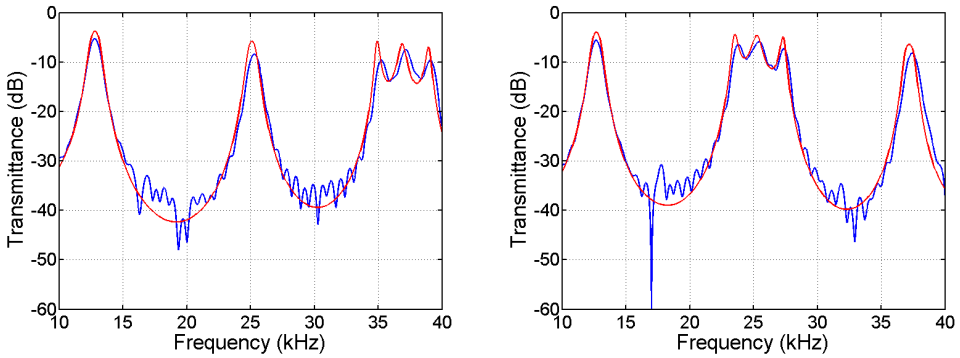

(a) $h_g = 4.8$ mm (b) $h_g = 6.8$ mm

Figure 6.15: Experimental (blue lines) and simulated (red lines) transmission data of the the DF structure at gap sizes (a) 4.8 mm and (b) 6.8 mm.

6.6 Concluding Remarks

In this chapter the acoustic transmittance of the DF was investigated numerically and experimentally as a function of the angle of incidence, the plate offset, and the gap size. The stop-band of the DF was shown to be largely unaffected by the angle of incidence. Control of the stop-band frequency was achieved by varying the plate offset h_{off} and the gap size h_g, however the frequency shift was only to higher frequencies as either parameter was increased. For the case of hole misalignment the frequency of the stop-band can be approximately determined by the shortest distance between the corner of the unit cell and a circular nodal line, centred on the input hole, with radius equal to h_{off}. This is equivalent to setting the wavelength to $\lambda = 4\left(\frac{\sqrt{2}\Lambda}{2} - h_{\text{off}}\right)$. For the case of varying gap size the frequency of the stop-band can be similarly determined approximately by the shortest distance between the corner of the unit cell and a circular nodal line, centred on the input hole with radius $\frac{h_g}{2}$. This is equivalent to setting the wavelength to $\lambda = 4\left(\frac{\sqrt{2}\Lambda}{2} - \frac{h_g}{2}\right)$. An additional mode is observed as h_g is increased that decreases in frequency, passing through the pipe modes of the system. This mode corresponds to the excitation of a mode in the gap, which is analogous to the lowest mode of a Fabry-Pérot etalon, and provides an additional condition for enhanced acoustic transmission. The coupling of this mode with the pipe modes of the DF leads to a condition where three resonant modes occur within a narrow frequency band.

Chapter 7

Acoustic Transmission of Structured Hole Arrays in Air

7.1 Introduction

It was previously shown that the response of the double fishnet (DF) structure has an acoustic stop-band at a frequency determined by the resonance in the gap between the plates (section 5.3). This stop-band can be tuned by varying the offset between the plates (section 6.3) or by increasing the gap between the plates (section 6.4). However increasing either of these parameters serves only to increase the frequency of the stop-band. In this chapter we modify the internal structure of the DF to significantly lower the frequency of the associated stop-band. This new geometry is herein referred to as the Helmholtz Double Fishnet (HDF) due to the similarity between the structured gap and a Helmholtz resonator.

7.2 Helmholtz Double Fishnet Sample

The HDF (figure 7.1) consists of a pair of 200 mm $\times$ 200 mm perspex plates of thickness $h_{\mathrm{p}} = 5.60$ mm which are perforated with circular holes of diameter $d = 2.40$ mm in a square array of pitch $\Lambda = 8$ mm. Two orthogonal arrays of 4 mm wide slots are milled to a depth of $h_{\mathrm{m}} = 3.00$ mm into one side of each plate forming two channels, whereby each hole is positioned within a square island of side length $l = 4.00$ mm, as shown in the upper right inset of figure 7.1. The two plates are then assembled with the holes aligned and the slotted faces on the inside of the structure. The plates are separated by a gap of $h_{\mathrm{g}} = 0.47$, 0.94 or 1.41 mm corresponding to the thickness of one, two or three spacers. The total cavity height h_{H} is given by $h_{\mathrm{H}} = 2h_{\mathrm{m}} + h_{\mathrm{g}}$.

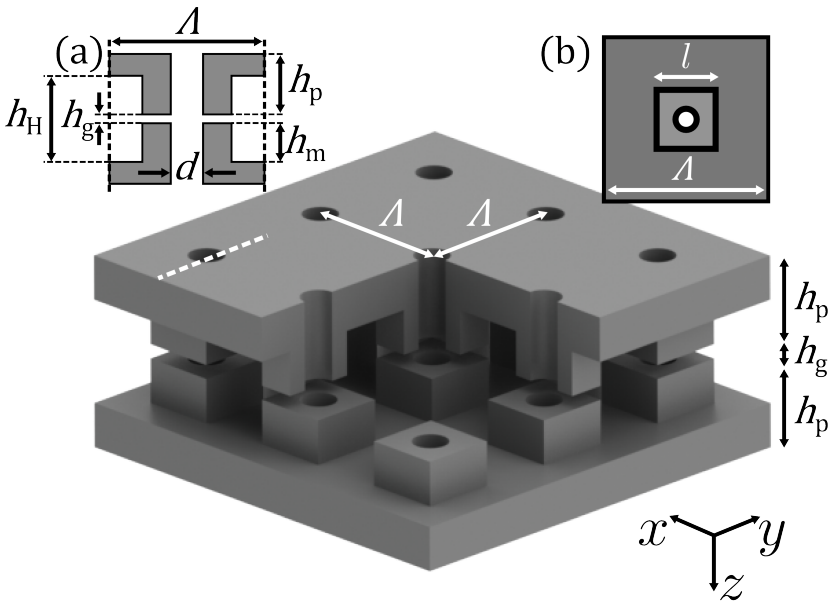

Figure 7.1: Schematic of the HDF structure with plate thickness h_p and gap size h_g. The HDF has a hole array with pitch Λ and a hole diameter d. Rectangular grooves of depth h_m milled into one face of each plate give a total cavity height of $h_H = 2h_m + h_g$. (a) A yz-plane view of the unit cell centred on one of the holes. (b) An xy-plane view of the unit cell within the gap showing the hole enclosed by an island with side l.

7.2.1 Simulated Transmittance of the Helmholtz Double Fishnet

The transmittance of the HDF cannot be simulated using the MM code used previously to model the transmittance of the DF due to the complex geometry of the interior gap. Instead, lossless FEM modelling of both structures is used to provide a comparison. Figure 7.2 shows the results of the FEM modelling confirming that the stop-band frequency of the HDF is significantly lower than that of the equivalent DF. The modelled stop-band of the HDF is at 8.0 kHz, corresponding to a factor of approximately 2.4 lower than the stop-band of the DF at 19.0 kHz. This HDF stop-band frequency is close to the predicted frequency of 8.9 kHz found by approximating the gap within a unit cell as a simple Helmholtz resonator (see below).

7.2.2 Analogy to the Helmholtz Resonator

The upper left inset of figure 7.1 shows a yz-plane view of the unit cell centred on one of the holes (position corresponding to the white dashed line in the main figure). The gap region consists of a narrow neck surrounded by a wider gap and hence this modified gap functions much like a Helmholtz resonator (section 2.4.3) where the compliance

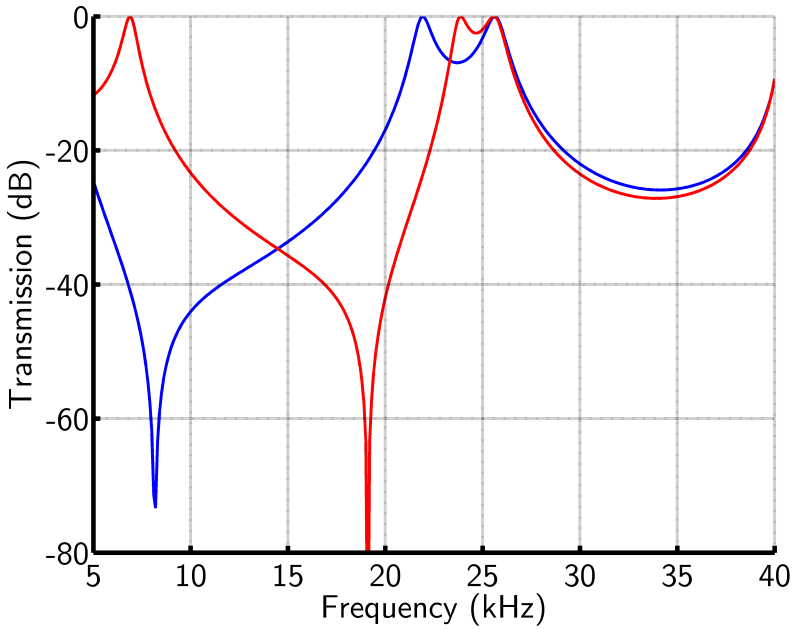

Figure 7.2: Comparison between a DF (red line) where $\Lambda = 8.00$ mm, $h_\mathrm{p} = 5.94$ mm, $d = 2.40$ mm and $h_\mathrm{g} = 0.94$ mm and an equivalent HDF (blue line) where $h_\mathrm{m} = 3.00$ mm and $l = 4.00$ mm.

is provided by the wider gap within a unit cell, with volume $V = \left(\Lambda^2 - l^2\right) h_\mathrm{H}$. The effective length and cross-sectional area of the neck are more complicated to determine, due to the geometry of the HDF. Allowing for the variation of the cross-section and length of the neck as it runs from the central hole towards the edge of the island, we estimate $L = \frac{l-d}{2}$ and $S = \pi d h_\mathrm{g}$. Substituting in values from the HDF sample the resonant frequency of the gap [equation (2.36)] is approximately 8.9 kHz. As already mentioned, this is close to the FEM value of 8.0 kHz, and may be compared to the gap-resonance frequency of the equivalent DF at 18.5 kHz, which is more than a factor of two higher.

7.2.3 Analytic Model of the Helmholtz Double Fishnet

An analytic model of the HDF is formed by adapting the analytic model of the DF described in section 5.3.2. Consider an open-ended pipe of length $h_\mathrm{T} = 2h_\mathrm{p} + h_\mathrm{g} + \Delta L$ (where ΔL is the end-correction) with a side branch at its mid-point that is modelled as a Helmholtz resonator and the modes calculated accordingly.

7.2.4 Even-order modes

As with the DF the even-order pipe modes are largely unperturbed by the gap and occur at frequencies approximately given by

$$f = \frac{Nc}{2h_{\mathrm{T}}}, \tag{7.1}$$

where N is an even integer and h_{T} is the total length of the pipe including end-effects.

7.2.5 Odd-order Modes

In section 5.3, the resonant frequencies of the DF were shown to be given by

$$\tan\left(\frac{\pi f h_{\mathrm{T}}}{c}\right) = -\frac{2X}{Z}, \tag{7.2}$$

where X is the reactance of the resonant side branch and $Z = \frac{4\rho_0 c}{\pi d^2}$ is the acoustic impedance of the pipe. If the gap corresponds to a Helmholtz resonator then the reactance is

$$X = 2\pi f \frac{\rho_0 L}{S} - \frac{\rho_0 c^2}{2\pi f V}, \tag{7.3}$$

where S is the cross-sectional area of the neck of the Helmholtz resonator, V is the cavity volume and L is the the length of the neck. This reactance is the sum of a mass term proportional to frequency and a compliance term inversely proportional to frequency. The resonant frequencies of the odd-order modes can thus be determined by evaluating

$$\tan\left(\frac{\pi f h_{\mathrm{T}}}{c}\right) = \frac{2A}{c}\left(\frac{c^2}{2\pi f V} - 2\pi f \frac{L}{S}\right). \tag{7.4}$$

Substituting numerical values, for the case of $h_{\mathrm{g}} = 0.94$ mm, the first three modes are found at 3.0 kHz, 20.8 kHz and 23.0 kHz which accord well with the FEM modelling of the HDF in figure 7.2. It is somewhat remarkable that the simplistic analytical model is in such agreement with the FEM modelling.

As outlined above, the stop-band is centred on the gap-resonance frequency, f_{gap}, which corresponds to the Helmholtz-resonance frequency given by (7.5)

$$f_{\mathrm{gap}} = \frac{c}{2\pi}\sqrt{\frac{S}{LV}}. \tag{7.5}$$

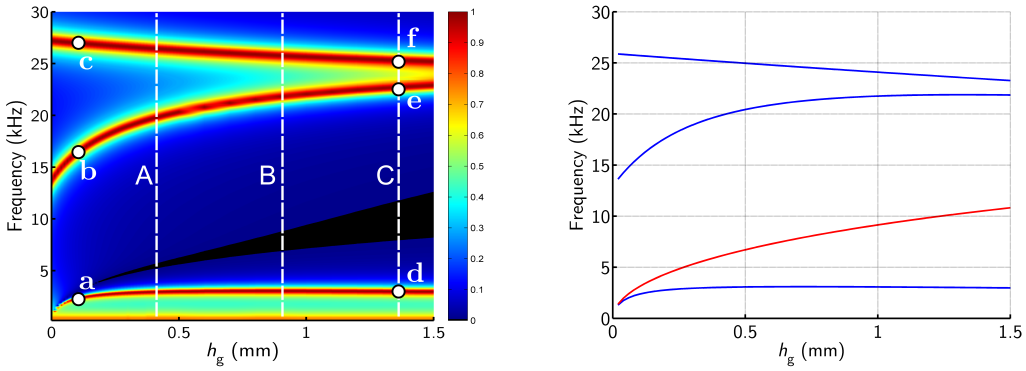

(a) FEM modelling

(b) Analytic modelling

Figure 7.3: (a)Modal matching method modelling of the transmission spectra of the HDF sample as a function of the gap size h_g. The black region corresponds to the stop-band, defined as less than −46 dB (0.05%) transmission. (b) Pipe mode frequencies (blue lines) and stop-band frequency (red line) calculated from the analytic treatment of the HDF.

7.3 Effect of the Gap Size on the Stop-band of the Helmholtz Double Fishnet

As $h_g \to 0$ mm the frequency of the stop-band associated with the DF approaches the resonant frequency of the gap, determined by the pitch of the hole array Λ. The resonant frequency of the Helmholtz resonators in the HDF on the other hand approaches 0 kHz as $h_g \to 0$ mm due to the area of the neck $S \to 0$ mm, as can be seen from equation (2.36).

7.3.1 Simulated Transmittance as a Function of Gap Size

FEM modelling of the HDF as a function of h_g is plotted in figure 7.3(a). At $h_g = 0$ mm, the results show the first mode of the structure at 13 kHz and the second mode at 26 kHz, corresponding to the two lowest-frequency modes of an open-ended pipe of length 11.2 mm (at zero gap the two 5.6 mm thick plates form an unbroken pipe). As the plates are separated ($h_g > 0$) the second mode (passing through marker 'c' in figure 7.3(a)) is largely unaffected due to the pressure node being at the position of the gap. However, the first mode which has a pressure antinode at the position of the gap, and hence couples to the gap resonance, splits into two distinct branches with frequencies above and below the gap resonance frequency (the modes passing through markers 'a' and 'b' in figure 7.3(a)). As $h_g \to \infty$ the system tends towards two isolated plates (i.e., two sets of 5.6 mm pipes) and the higher-frequency branch of the first mode converges

on the second mode. The lower branch of the first mode initially increases in frequency before reaching an almost constant frequency. The nature of these modes is discussed below in sections 7.3.2.1 and 7.3.2.2.

7.3.2 Analytic Model as a Function of Gap Size

To understand the properties of the HDF the previous analysis of the HDF (section 7.2.3) is extended to plot the pipe modes and stop-band frequency as a function of h_g, shown in figure 7.3(b). Comparison of the FEM and analytic modelling in figures 7.3(a) and 7.3(b), respectively, shows that the pipe mode frequencies and the frequency of the stop-band are in agreement. The analytic model explicitly shows the nature of the various modes.

7.3.2.1 Analysis of the Lowest Frequency Mode

As was previously mentioned, the lowest frequency mode shows an initial increase in frequency between $h_g = 0$ mm and 0.5 mm before reaching an almost constant frequency while all the other features of the graph are still shifting in frequency. This can be understood by looking for a low frequency solution to equation (7.4). Using $\tan(x) \approx x$ gives

$$\frac{\pi f h_T}{c} = \frac{\pi d^2}{2c}\left(\frac{c^2}{2\pi f V} - 2\pi f \frac{L}{S}\right), \tag{7.6}$$

which in turn can be rearranged to

$$f\left(\frac{\pi h_T}{c} + \frac{\pi d^2}{2c} 2\pi \frac{L}{S}\right) = \frac{1}{f}\left(\frac{\pi d^2}{2c}\frac{c^2}{2\pi V}\right). \tag{7.7}$$

This can be further manipulated to obtain

$$f = \frac{c}{\pi}\sqrt{\frac{\frac{\pi d^2}{4V}}{\left(h_T + \frac{\pi d^2 L}{S}\right)}}. \tag{7.8}$$

For larger values of h_g the second term in the denominator negligible, i.e. $h_T >> \frac{\pi d^2 L}{S}$ (where $S = \pi d h_g$), giving

$$f = \frac{c}{\pi}\sqrt{\frac{A}{V h_T}}, \tag{7.9}$$

where $A = \frac{\pi d^2}{4}$.

If this is compared to a Helmholtz resonator whose neck is formed by the plate holes acting in parallel, the formula for the Helmholtz resonance as given by equation (2.36) gives the same expression as equation (7.9). This explains why the lower frequency

branch in figure 7.3(a) shows little variation with h_g over most of the range; the resonant frequency depends on the cavity volume V and the pipe length h_T, but these show little variation with h_g if h_g is small. The same behaviour was observed in the study of the DF with gap size in section 6.4 although the size of the gap required for the mode to reach an almost constant frequency was significantly greater.

For small values of h_g, $\frac{1}{S}$ is large and the second term in the denominator dominates, i.e. $h_T << \frac{\pi d^2 L}{S}$, giving

$$f = \frac{c}{2\pi}\sqrt{\frac{S}{VL}}, \tag{7.10}$$

which is equivalent to the gap resonance.

7.3.2.2 Splitting of the Fundamental Mode

Unperturbed, the odd-order modes of a pipe correspond to pressure fields with phase shifts along the pipe of $n\pi$ (n odd). The first mode has a phase shift of π along the pipe and higher odd modes cycle through additional phase shifts of 2π, being still π out of phase at the exit due to the 2π degeneracy of sinusoidal waves. In the HDF the coupling of the first mode to the gap resonance causes it to split either side of the stop-band. The lower-frequency branch of the first mode would cycle through less than π phase along the pipe if unperturbed by the gap. It achieves an overall phase shift of π by coupling to the gap resonance and gaining phase at the gap. The higher-frequency branch would conversely cycle through more than π phase along the pipe if unperturbed. An overall phase shift of π is achieved by coupling to the gap resonance and losing phase at the gap. Instantaneous pressure profiles of these modes along a line through the centre of the HDF are shown in figure 7.4 (corresponding to markers a-f in figure 7.3(a)). A background image of the HDF unit cell corresponding to inset (a) in figure 7.1 is provided for clarity. Panels 7.4(a) and 7.4(b) correspond to the lower branch of the first mode at gap sizes of $h_g = 0.2$ mm and $h_g = 1.4$ mm respectively. The pressure field is almost linear through the pipes apart from a rapid curvature in the region of the gap. The linear regions correspond to 'lumped' volume flow in the two half pipes i.e., all in phase, as expected in the case of an overall Helmholtz resonance - see section 7.3.2.1. Panels 7.4(c) and 7.4(d) correspond to the upper branch of the first modes at gap sizes of $h_g = 0.2$ mm and $h_g = 1.4$ mm respectively. The pressure field shows a sinusoidal profile with phase shifts greater than $\frac{\pi}{2}$ in each half pipe, and a loss of phase at the gap. Panels 7.4(e) and 7.4(f) correspond to the second mode at gap sizes of $h_g = 0.2$ mm and $h_g = 1.4$ mm respectively. As expected, the profile is almost a perfect sinusoid and is largely unperturbed by the gap.

The two branches of the first mode might be expected to originate at 13 kHz, cor-

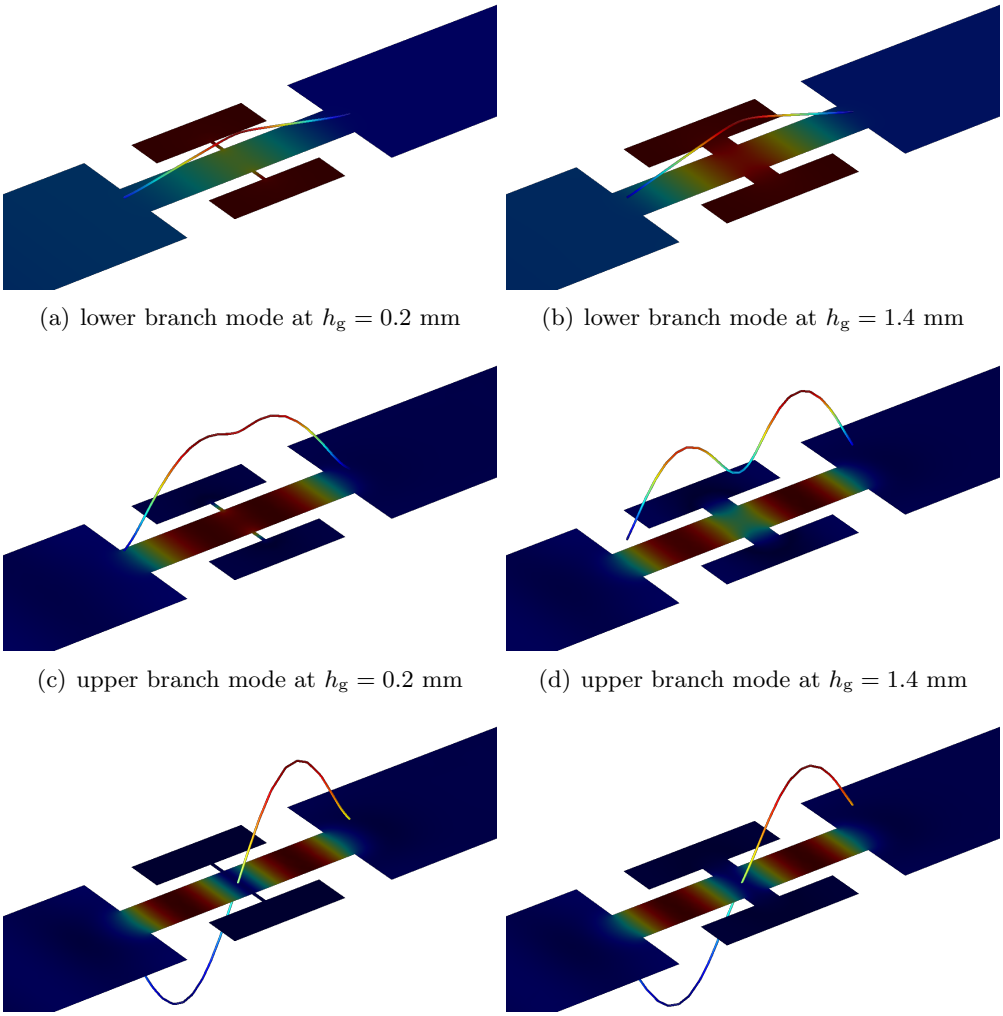

(a) lower branch mode at $h_g = 0.2$ mm

(b) lower branch mode at $h_g = 1.4$ mm

(c) upper branch mode at $h_g = 0.2$ mm

(d) upper branch mode at $h_g = 1.4$ mm

(e) 2nd mode at $h_g = 0.2$ mm

(f) 2nd mode at $h_g = 1.4$ mm

Figure 7.4: Time-averaged pressure profiles in a central xz-plane through the HDF structure. Profiles show the 2nd mode, the upper branch of the split fundamental and the lower branch of the split fundamental at gap sizes $h_g = 0.2$mm and $h_g = 1.4$ mm. The out-of-plane line corresponds to the instantaneous pressure of the mode at the phase angle of maximum amplitude.

responding to the fundamental mode of the system with $h_g = 0$ mm, however the lower branch originates at zero frequency as a consequence of the gap-resonance frequency tending to zero as $h_g \to 0$ mm.

7.3.3 Experimental Study of Gap Size

In the corresponding experimental study (see section 4.2.3) data were obtained for gap sizes of (a) $h_g = 0.47$ mm, (b) $h_g = 0.94$ mm, and (c) $h_g = 1.41$ mm. Figure 7.5

shows these experimental data (blue lines) along with the respective FEM modelling for each gap size (red lines). The expected positions of the acoustic stop-band are clearly seen as sharp troughs in the modelled data. General agreement can be seen between the experimental transmission peaks with the modelling and some agreement with the position of the stop-band. However, the data obtained in the region of the stop-band is considerably noisier than that obtained for the DF in chapters 5 and 6. This is attributed to the reduced signal-to-noise ratio attainable with the experimental equipment at lower frequencies. The stop-band frequencies corresponding with each gap size are in agreement with the square-root law suggested by equation (7.10). It is apparent that, as the gap size is reduced the width of the stop band decreases. For convenience, we define the width of the stop-band from the points of −46 dB transmission. This width for a 0.47 mm gap is 0.7 kHz (12% of the stop-band frequency) while for a 0.94 mm gap and for a 1.41 mm gap the widths are 2.3 kHz (30% of the stop-band frequency) and 4.3 kHz (46% of the stop-band frequency) respectively. There are two factors contributing to this reduced bandwidth with decreasing gap size. Firstly, the Q-factor [equation (7.11)] of the Helmholtz resonator increases as the neck cross-section is reduced [41]. Secondly, as the stop-band is lowered in frequency it converges with the frequency of the lower frequency transmission resonance, which will affect the transmittance.

$$Q_{\mathrm{H}} = 2\pi\sqrt{V\left(\frac{L}{S}\right)^3}. \tag{7.11}$$

7.4 Concluding Remarks

In this chapter the acoustic transmittance of a HDF was investigated experimentally and by modelling. The HDF was shown to possess an acoustic stop-band at lower frequency than the equivalent DF. Introduction of a bi-grating of grooves within the gap between the plates causes the gap to respond like an array of Helmholtz resonators and hence lowers the gap-resonance frequency. The lower branch of the first mode evolves into another Helmholtz resonator mode where the holes in each plate act as necks in parallel and the gap behaves as a compliance; this mode originates at zero frequency when $h_{\mathrm{g}} = 0$ mm.

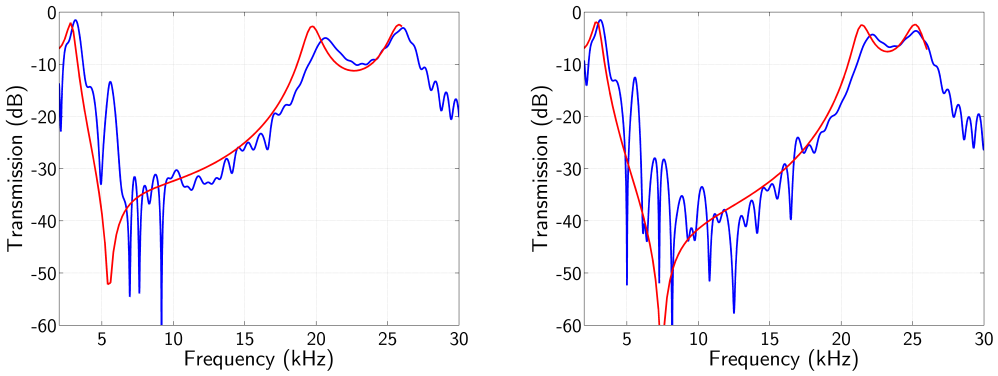

(a) $h_g = 0.47$ mm

(b) $h_g = 0.94$ mm

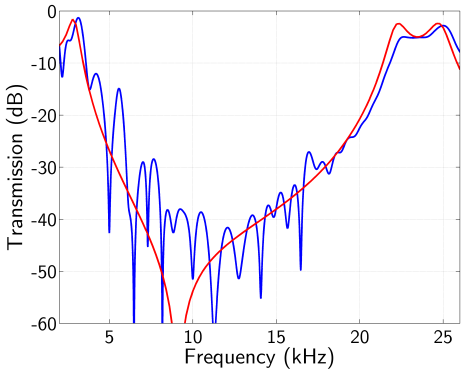

(c) $h_g = 1.41$ mm

Figure 7.5: Experimental (blue line) and modelled (red line) data for the HDF structure with gap sizes of $h_g = 0.47$ mm, 0.94 mm and 1.41 mm respectively.

Chapter 8

Acoustic Intromission at Near-Normal Incidence

8.1 Introduction

In chapter 5 the phenomenon of enhanced acoustic transmission of a single fishnet (SF) was discussed; the mechanism leading to the enhanced transmission was the excitation of resonant pipe modes. In this chapter a non-resonant mechanism is discussed whereby at a specific angle of incidence the transmission of sound through a SF approaches unity. We then look at how the system can be modified such that that broadband transmission may occur at angles close to normal incidence. Section 8.2 introduces the idea of intromission by looking at the transmission of sound from one medium to another. Section 8.3 looks at the geometric intromission through a SF in a single fluid. Section 8.4 then investigates the effect of replacing the fluid within the pipes with a different fluid. The choice of media is restricted to fluids so that only longitudinal acoustic waves are supported.

8.2 Transmission Between Dissimilar Media

To introduce the mechanism of intromission we first discuss the transmission of sound across the interface of an impedance mismatch.

8.2.1 Transmission Between Dissimilar Media at Normal Incidence

Consider a plane wave incident normal to the interface between two semi-infinite media (figure 8.1). The acoustic impedance of each media is given by ρc where ρ is the density of the medium and c is the speed of sound The pressure field of the incident, reflected

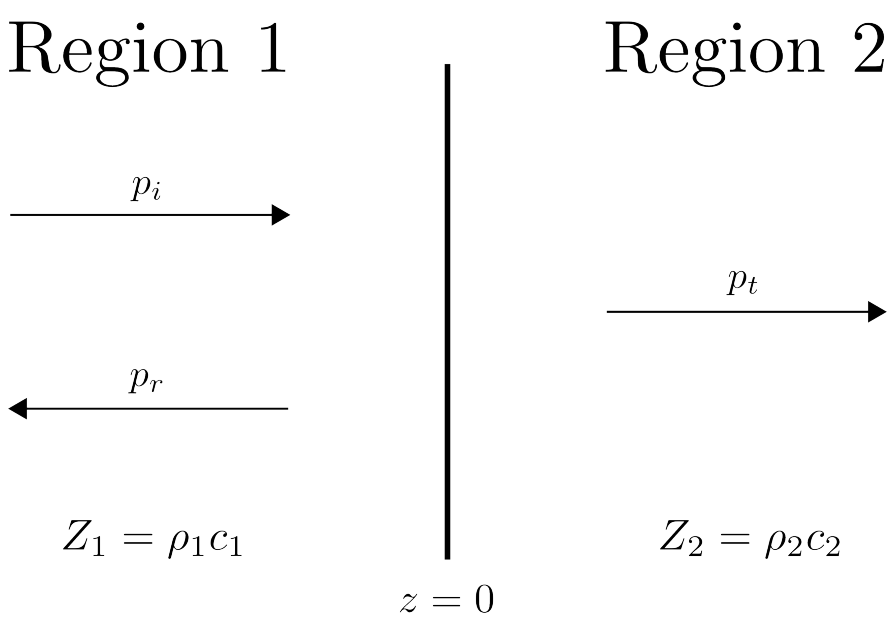

Figure 8.1: Transmission and reflection of a plane wave incident normal to the interface between two media with different specific impedances.

and transmitted components of the wave can be described by

$$p_i = P_i \exp\left[i\left(\omega t - kz\right)\right], \tag{8.1}$$

$$p_r = P_r \exp\left[i\left(\omega t + kz\right)\right], \tag{8.2}$$

$$p_t = P_t \exp\left[i\left(\omega t - kz\right)\right], \tag{8.3}$$

where P_i, P_r and P_t are the pressure amplitudes of the waves. The reflection and transmission coefficients, r and t, can be readily calculated by matching the pressure and the normal component of the particle velocity, u, across the boundary. The sound wave satisfies two boundary conditions at every point along the interface between the two media.

$$p_i + p_r = p_t, \tag{8.4}$$

$$u_i + u_r = u_t. \tag{8.5}$$

Taking the ratio of the two boundary conditions and substituting in for $u = \frac{p}{\pm \mathbf{Z}}$, where the sign of the impedance depends on the direction of propagation, gives

$$Z_1 \frac{p_i + p_r}{p_i - p_r} = Z_2, \tag{8.6}$$

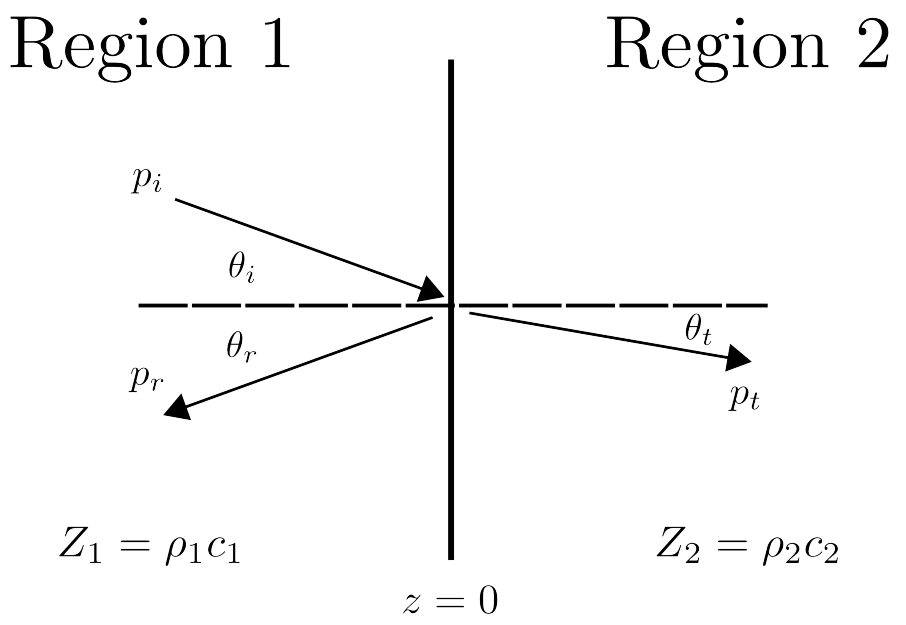

Figure 8.2: Transmission and reflection of a plane wave incident at an oblique angle to a planar interface between two media with different acoustic impedances.

which leads to the well established expressions for the reflection and transmission coefficients.

$$r = \frac{Z_2/Z_1 - 1}{Z_2/Z_1 + 1}, //t \qquad = \frac{2Z_2/Z_1}{Z_2/Z_1 + 1}. \tag{8.7}$$

It should be noted that the reflection coefficient may be either positive or negative, which corresponds to whether the reflected wave is in phase or π out of phase with the incident wave.

8.2.2 Transmission Between Dissimilar Media at Oblique Incidence

Assume now that the planar pressure field p_i is incident at an angle θ_i to the normal of a planar interface between two dissimilar media. The wave p_r is reflected at an angle θ_r to the normal of the interface, where $\theta_i = \theta_r$, and the transmitted wave p_t makes an angle θ_t to the normal. For simplicity, the propagation vectors are restricted to the xz-plane with the interface located at $z = 0$. The waves can be written as

$$p_i = P_i \exp\left[i(\omega t - k_1 \cos(\theta_i)\, z + k_1 \sin(\theta_i)\, x\right], \tag{8.8}$$

$$p_r = P_r \exp\left[i(\omega t + k_1 \cos(\theta_r)\, z + k_1 \sin(\theta_r)\, x\right], \tag{8.9}$$

$$p_t = P_t \exp\left[i(\omega t - k_2 \cos(\theta_t)\, z + k_2 \sin(\theta_t)\, x\right]. \tag{8.10}$$

As before, the pressure must be continuous across the boundary at $z = 0$, yielding

$$P_i \exp\left[ik_1 \sin\left(\theta_i x\right)\right] + P_r \exp\left[-ik_1 \sin\left(\theta_r\right) x\right] = P_t \exp\left[ik_2 \sin\left(\theta_t\right) x\right]. \tag{8.11}$$

Since equation (8.11) must be true for all values of x the exponents must all be equal. Hence is the amplitude of the incident wave is taken to be unity equation (8.11) reduces to give a statement regarding the amplitudes of the reflected and transmitted waves.

$$1 + r = t. \tag{8.12}$$

Also obtained is a statement of Snell's Law

$$k_i \sin\left(\theta_i\right) = k_t \sin\left(\theta_t\right). \tag{8.13}$$

Similarly, the normal component of the particle velocity must be continuous across the interface

$$u_i \cos\left(\theta_i\right) + u_r \cos\left(\theta_r\right) = u_t \cos\left(\theta_t\right). \tag{8.14}$$

Substituting in for

$$u = \frac{p}{\pm Z}$$

provides a second statement of r and t is obtained.

$$1 - r = \frac{Z_1}{Z_2} \frac{\cos\left(\theta_t\right)}{\cos\left(\theta_i\right)} t. \tag{8.15}$$

Combining equations (8.12) and (8.15) to eliminate $\mathbf{t}$ and obtain a statement for $\mathbf{r}$

$$R = \frac{Z_2/\cos(\theta_t) - Z_1/\cos(\theta_i)}{Z_2/\cos(\theta_t) + Z_1/\cos(\theta_i)}, \tag{8.16}$$

referred to as the Rayleigh reflection coefficient.

Before proceeding, Snell's law [equation (8.13)] can be rewritten to simplify later expressions.

$$\cos\left(\theta_t\right) = \sqrt{1 - \left(c_2/c_1\right)^2 \sin^2\left(\theta_i\right)}. \tag{8.17}$$

From the recast Snell's law (8.17) three results can be identified. Firstly if $c_1 > c_2$, the angle of transmission θ_t is a real number and less than the angle of incidence. Secondly if $c_1 < c_2$ and $\theta_i < \theta_c$, where θ_c is the critical angle defined by

$$\sin\left(\theta_c\right) = \frac{c_1}{c_2}, \tag{8.18}$$

the angle of transmission is a real number but greater than the angle of incidence.

Finally if $c_1 < c_2$ and $\theta_i > \theta_c$, the angle of the transmitted wave is now evanescent with no power transmitted. The consequence of this, if medium 2 is semi-infinite, is that the incident wave is completely reflected at the boundary.

8.2.3 Angle of Acoustic Intromission

Under certain circumstances an unusual phenomenon may occur whereby an incident wave is completely transmitted into the second medium. The phenomenon bares resemblance to the total transmission of TM polarised light at the Brewster angle [64]. Taking the Rayleigh reflection coefficient [equation (8.16)] and using Snell's law [equation (8.17))] to eliminate θ_t, an expression for θ_i is arrived at which satisfies $R = 0$. The angle at which this occurs is termed the angle of intromission, θ_I.

$$\theta_I = \sin^{-1}\left(\sqrt{\frac{\left(Z_2/Z_1\right)^2 - 1}{\left(Z_2/Z_1\right)^2 - \left(c_2/c_1\right)^2}}\right), \tag{8.19}$$

which is constrained by the conditions (1) $Z_1 < Z_2$ and $c_1 > c_2$ or (2) $Z_1 > Z_2$ and $c_1 < c_2$.

One situation where the phenomenon arises in nature is at the interface between water and high porosity marine sediments such as silty clay [1]. Silty clay has a slightly reduced speed of sound compared to water whilst possessing a higher acoustic impedance and thus satisfies constraint (2). However, there is an alternative route to acoustic intromission by the use of geometric impedance matching.

8.2.3.1 Geometric Intromission

Consider a periodic square array of apertures in a perfectly rigid plate. A unit cell can be described with an aperture at the centre of a square. The acoustic impedance of the incident wave, Z_1, is given by equation (2.19) as is the acoustic impedance, Z_2, of the wave travelling through the aperture. The ratio of the impedances is then given by

$$\frac{\mathbf{Z}_2}{\mathbf{Z}_1} = \frac{S_2}{S_1}, \tag{8.20}$$

where S_1 and S_2 are the respective cross-sectional areas of the unit cell and the aperture. If the angle of incidence is changed, the area of the unit cell normal to the propagation direction of the incident wave decreases. The change in the projected area is accounted for by replacing S_1 with $S_1 \cos(\theta_i)$ such that at normal incidence, the area remains unchanged and at any other angle, the projection of the wave onto the unit cell is equal to the area of the unit cell. Thus a simple formula is obtained giving a unity impedance

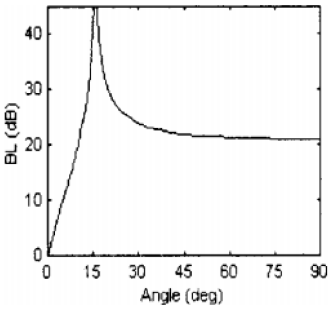

(a)

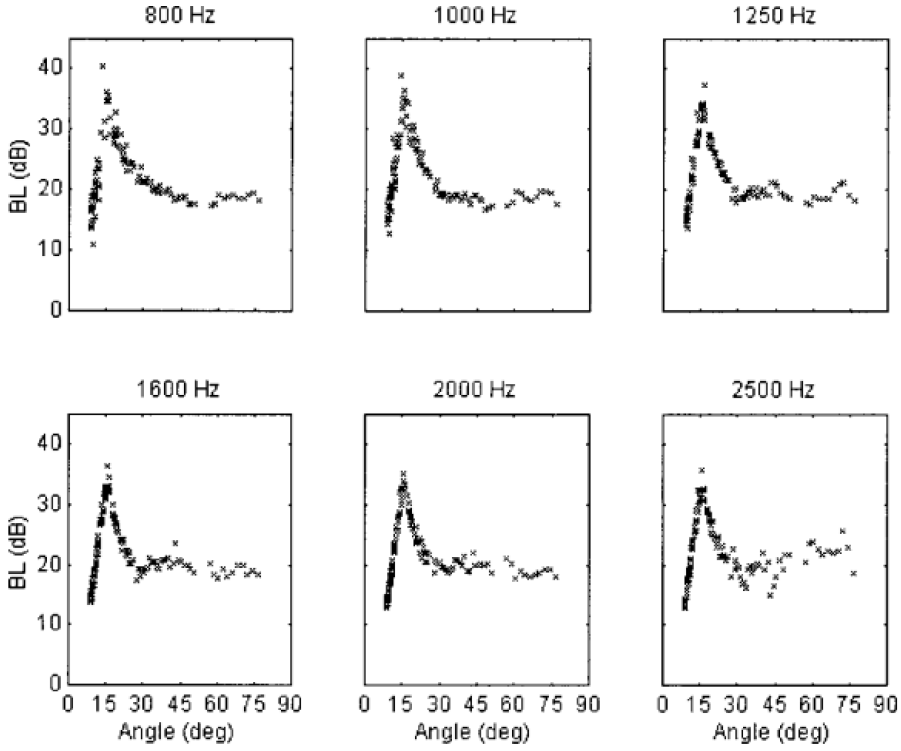

(b)

Figure 8.3: Figures taken from Holland [1] showing (a) Theoretical reflection loss for a seabed whose sound speed is smaller than that of water. Sound speed and density ratios are 0.9822 and 1.2174. respectively and (b) Bottom reflection loss from first sediment layer on the Malta Plain. The salient feature is the peak at 75° degrees from normal, corresponding to the angle of intromission.

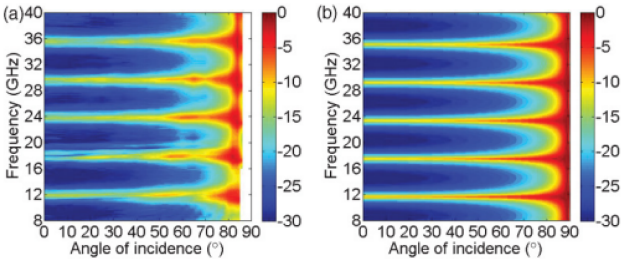

Figure 8.4: Experimental and FEM model data showing the broadband transmission of TE radiation through a 1D metallic grating, taken from Aközbek *et al.* [2]

ratio and the geometric angle of intromission is given by equation (8.21).

$$\theta_I = \arccos\left(\frac{S_2}{S_1}\right), \tag{8.21}$$

where $\frac{S_2}{S_1}$ is the aperture area ratio.

The existence of geometric impedance matching angle was originally demonstrated electromagnetically for a 1D metallic grating [42] and then for 2D metallic gratings [43]. Experimental data for the the 1D metallic grating was provided by Aközbek *et al.* [2]; transverse electric electromagnetic radiation is incident at an angle θ to a periodic array of metallic slits. Example data that clearly demonstrates the broadband transmission at high angle is shown in figure 8.4. The equivalent acoustic experiment was performed shortly afterwards [44].

At the geometric intromission angle the impedance of the incident radiation is perfectly matched to the impedance of the structure. The beauty of the mechanism is that it is non-resonant and hence transmission occurs across a wide band of frequencies. However, decreasing the aperture size causes a rapid increase in the angle at which intromission occurs; an incident angle of $\theta_i = 30°$ is required for an aperture ratio of 0.86 and an incident angle of $\theta_i = 60°$ is required for an aperture area ratio of 0.5. However as is explored in this chapter, varying the medium within the aperture allows the angle of acoustic intromission to be reduced such that it occurs at normal incidence.

8.3 Geometric Intromission within a Single Fluid

The method of modal matching was previously described and used to determine the acoustic transmission through a SF structure (appendix A). The calculation is reused here to investigate the transmission of sound through a rigid SF at the angle of intromission. As a reminder, the SF consists of a square array of sub-wavelength apertures in a perfectly rigid plate (figure 8.5). The system is split into three regions, I, II and III

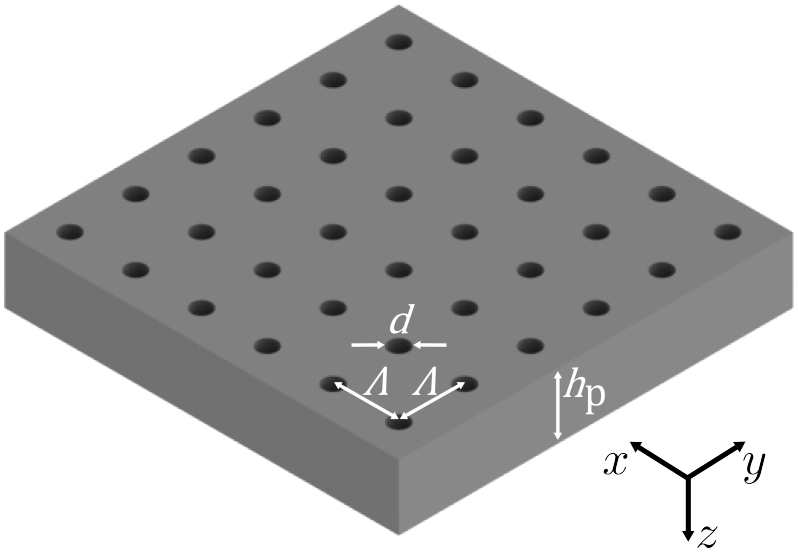

Figure 8.5: Schematic drawing of a single rigid plate perforated with a periodic square array of circular holes. Λ is the pitch of the hole array, d is the diameter of the holes and h_p is the thickness of the plate.

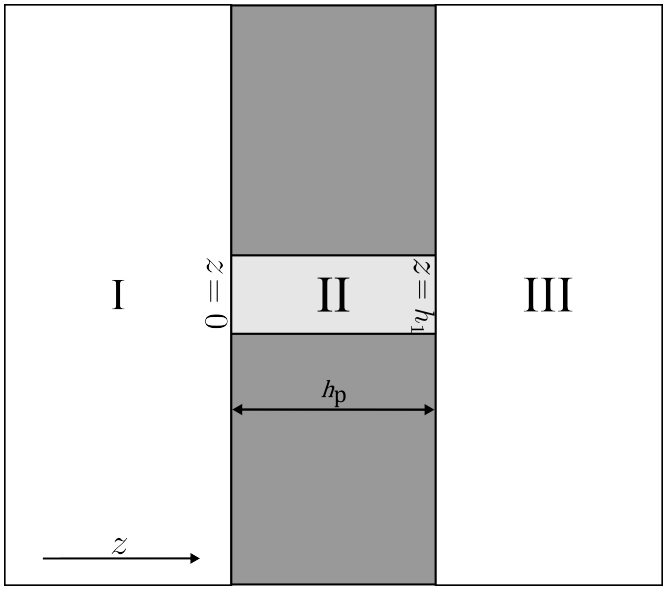

Figure 8.6: Schematic side view of the SF structure showing the different regions used in formulating the modal matching calculation of the structure's transmittance.

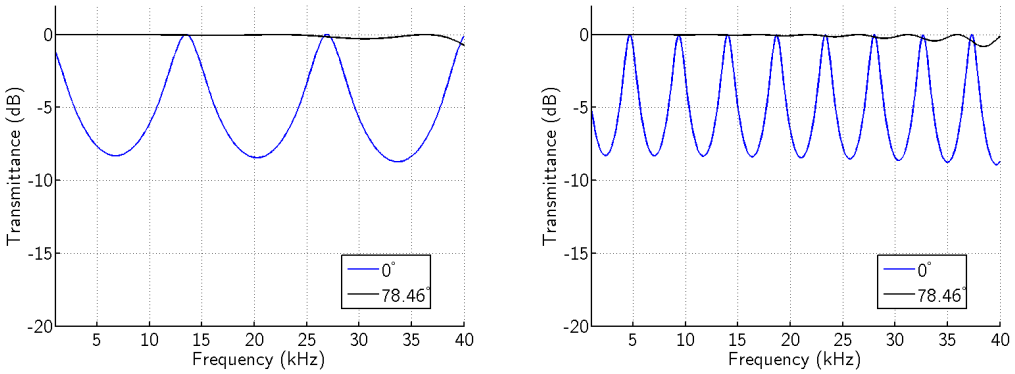

(a) $h_p = 12$ mm (b) $h_p = 36$ mm

Figure 8.7: MM modelling of the transmittance of a SF with an aperture area ratio of 0.2 at normal incidence (black line) and at the angle of intromission, $\theta_I = 78.46°$ (blue line).

comprising the incident medium, the medium within the apertures and the transmission medium as shown in figure 8.6. At the interface between each region the acoustic pressure and the normal component of the particle velocity fields are matched via the boundary conditions; the pressure field is continuous over the aperture and the normal component of the particle velocity is continuous over the whole of the surface.

In the works by D'Aguanno *et al.* [44] and Qi *et al.* [65] the fluid medium is identical in regions I, II and III; as such the angle of acoustic intromission is determined purely by the geometry. To achieve total transmission at normal incidence S_1 must equal S_2. As S_2 is reduced in any aperture geometry, the angle of incidence must increase to maintain the impedance matching condition. Figure 8.7 shows the MM simulated transmission of two different thickness SFs ($h_p = 12$ mm in figure 8.7(a) and $h_p = 36$ mm in figure 8.7(b) with an aperture ratio of 0.2. Air is chosen as the medium of propagation in all regions. The black line shows the transmittance at normal incidence and the blue line shows the transmittance at the angle of intromission, $\theta_I = 78.46°$. The pitch of the hole array is $\Lambda = 4$ mm, which has been chosen so that the analyses are below diffraction. At normal incidence the anticipated transmission peaks associated with the excitation of pipe modes are clearly observed. At the angle of intromission the transmittance approaches unity across the entire frequency range.

8.4 Geometric Intromission with a Different Fluid Filling the Apertures

Now the effect of filling the apertures of the SF with a different fluid is explored. In doing so the broadband total transmission of sound is obtained at normal incidence. The MM code is again used to simulate the transmission of the structure before verification of the observed response is undertaken using FEM modelling.

The angle of intromission occurs when the acoustic impedance in the regions I and III is perfectly matched to that in region II. When the same fluid is in all three regions, the impedance of region II is higher due to the smaller cross-sectional area. By recasting the geometric impedance matching equation to account for a change of media in the apertures, a new expression of the intromission angle is obtained, equation (8.22).

$$\theta_{\mathrm{I}} = \cos^{-1}\left(\frac{S_2}{S_1}\frac{\rho_1 c_1}{\rho_2 c_2}\right). \tag{8.22}$$

To obtain geometric intromission at normal incidence, i.e., $\theta_{\mathrm{I}} = 0°$, the expression

$$\frac{S_2}{S_1}\frac{\rho_1 c_1}{\rho_2 c_2} = 1.$$

Given that $S_2 < S_1$, we are restricted to choosing a fluid for region II which has a lower acoustic impedance than that in regions I and III in order to satisfy the condition. Suspending practicality and using water in regions I and III and air in region II, to satisfy the condition for intromission at normal incidence an aperture area ratio of $0.0002\dot{3}$ is required as calculated from equation (8.4). For a structure of the same pitch as those in section 8.3 this will lead to apertures with a negligible diameter where the effects of viscous losses will dominate and prevent transmission. Increasing the aperture size to the point where viscous losses become negligible would require a significant increase in the pitch of the hole array making an experimental sample impractical. Additionally, significantly increasing the pitch may lead to undesired diffraction. However, in the absence of viscous losses the transmission of the structure is shown in figure 8.8(a). As can be seen, the transmittance is not unity across the frequency range as was anticipated. A band of near unity transmission is seen at low frequencies and a series of peaks corresponding to the resonant modes of the pipe are present at higher frequencies. The trough between the peaks becomes progressively deeper as the the frequency is increased. This arrangement was recently proposed using slits rather than holes by Qiu *et al.* [45] however due to the decision to plot the results as transmittance against wavelength the observations made above were obscured. Plotting against wavelength has the effect of stretching the low frequency region while compressing the high fre-

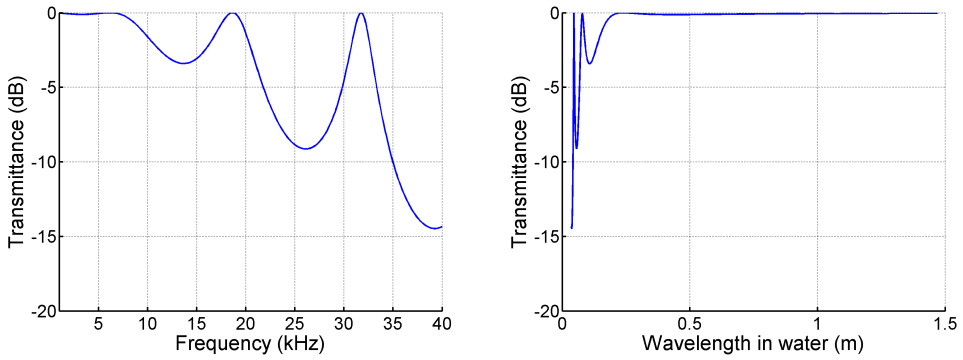

(a) (b)

Figure 8.8: (a) MM modelling of the normal incidence transmittance of a SF in water, with air filling the holes and an aperture area ratio of $0.0002\dot{3}$. (b) Data in (a) re-plotted against the wavelength in water

quency region as shown in figure 8.8(b), which shows the same data as figure 8.8(a). Similar behaviour is weakly observed in figure 8.7. Further investigation is required to determine the origin of why the impedance matching condition fails but it can be stated that the geometric intromission will occur below the fundamental resonance of the pipe. The speed of sound in air makes the pipe appear much longer than the equivalent pipe filled with water, which has the effect of decreasing the frequency of the fundamental mode of the pipe considerably.

In any case, such a system is likely to be impractical due to the requirements of trapping air in extremely narrow apertures. Additionally, the effect of submersion in water will compress the air leading to a change in the impedance of the air region. Compression of the air region will allow water to partially fill the aperture preventing the impedance matching across the interface.

In order to achieve a more realistic system the air can be replaced with an incompressible fluid with the appropriate acoustic properties. Silicon oil (Dow 200, 1 centistoke) with a density of $\rho = 818$ kgm^{-3} and speed of sound $c = 960$ ms^{-1} [66] provides suitable material properties. With these parameters the aperture area ratio required is 0.53. Figure 8.9 shows the transmittance at normal incidence of a SF with an aperture area ratio of 0.53 where the apertures have been filled with silicon oil. The transmittance is unity across the plotted frequency range. As both water and silicon oil are approximately incompressible this system is experimentally realisable.

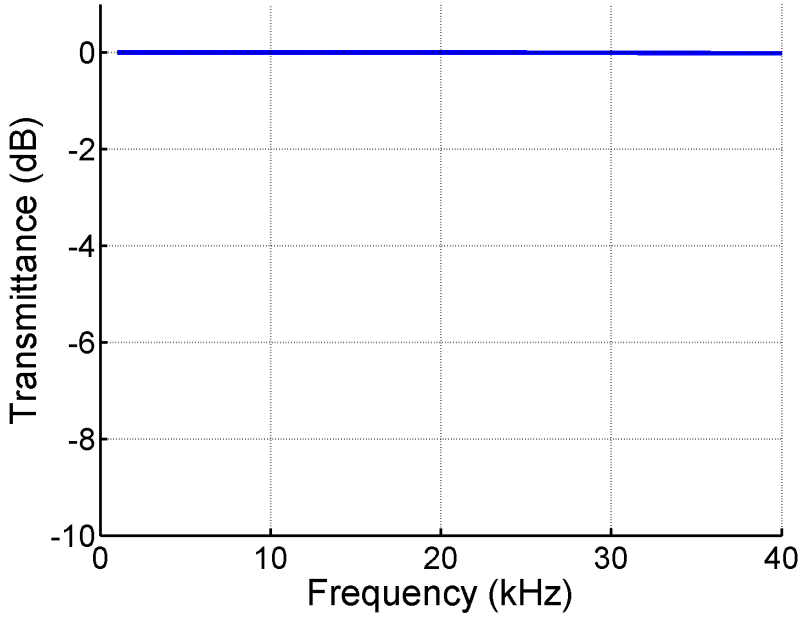

Figure 8.9: Modal matching modelling of the normal incidence transmittance of a SF in water, with silicon oil (Dow 200, 1 centistoke) filling the holes and an aperture area ratio of 0.53.

8.5 Conclusions and Future Work

The work in this chapter has demonstrated total transmittance of sound through a SF at normal incidence across a wide range of frequencies. The mechanism by which this occurs is by geometrically matching the impedance through the system. While the results are based entirely upon modelling we have proposed water and silicon oil (DOW 200, 1 centistoke) as providing a system where intromission at normal incidence to be experimentally realisable. The two fluids are required to be kept separate while being acoustically connected. This could be achieved through the use of a thin membrane covering each end of the aperture. While it is possible that the membrane itself would be resonant, any effects relating to this could be removed from the frequency range of interest by varying the tension on the membrane.

8.6 Acknowledgement

The work in this chapter was undertaken in collaboration with Prof. L. Martín-Moreno and Dr S. Carretero-Palacios. We are grateful to the both of them for the collaboration and their efforts.

Chapter 9

Resonant Acoustic Tunnelling through Acoustically Soft Waveguides

9.1 Introduction

The boundary condition imposed by an acoustically soft boundary forces the pressure of an incident wave to zero. A cavity with soft walls will for this reason have a cut-off frequency below which sound is forbidden from propagating. In this chapter we examine the tunnelling of sound through a soft walled waveguide at frequencies below the cut-off frequency. The transmission bares resemblance to the well established quantum mechanical tunnelling. The waveguide is required to be thin to allow evanescent coupling of the the acoustic field through the waveguide. Following this, we consider the effect of placing two waveguides in close proximity to one another, allowing demonstration of a resonant tunnelling condition which significantly increases the level of transmission below the cut-off frequency. This second phenomenon is similarly analogous to the resonant quantum mechanical tunnelling observed when two tunnel barriers are located in close proximity.

Section 9.2 discusses the boundary conditions imposed by different materials and the consequences they have on the propagation of sound through waveguides. Section 9.3 provides a brief discussion of tunnelling and resonant tunnelling. Section 9.5 looks at the transmission through a single soft-walled slit as an introduction to section 9.6 where the transmission through two closely spaced soft-walled slits is examined. Experimental data is compared to FEM modelling of the structures in both cases.

9.2 Acoustic Wave Guides

In 1948, Jacobi considered the propagation of sound through pipes with various boundary conditions, of which two systems are of particular interest to the work presented here [67]. The first case is that of sound propagating in a pipe with acoustically *rigid* walls (i.e. possessing characteristic impedance with magnitude greater than that of the medium of propagation). Consider a circular pipe with its axis in the z direction. The boundary condition imposed by a *rigid* boundary is that the normal component of the particle velocity must be zero at the wall. The allowed propagating modes of the pipe are determined from the solutions of the acoustic wave equation [equation (9.1)] in a circular waveguide, which are given by Bessel's equations.

$$\nabla^2 p = \frac{1}{c^2}\frac{\partial^2 p}{\partial t^2}. \tag{9.1}$$

The velocity is given by the derivative of the pressure function, thus the waveguide modes can be found by looking for $J'_{\mathrm{n}}(k_{\mathrm{n,m}}a) = 0$, where n is the order of the Bessel function, k is the wavenumber, m is the order of the zero and a is the radius of the pipe. The first of these zeroes occurs at zero frequency, $J'_0(0) = 0$, therefore permitting the propagation of plane waves at all frequencies (i.e. there is no cut-off for plane wave propagation). Higher order modes exist above cut-off frequencies determined by further zeroes in $J'_n(k_{\mathrm{n,m}}a)$. For a circular pipe, the cut-off frequencies are given by

$$f_{nm} = \frac{ck_{\mathrm{n,m}}}{2\pi}. \tag{9.2}$$

The transmission properties of a square array of rigid walled pipes was examined in the preceding chapters.

The second case arises for sound propagating in a higher impedance medium such as water where, by choice of the appropriate material such as a closed cell foam, the walls of the waveguide can be acoustically soft. An acoustically soft boundary occurs when the waveguide wall has a significantly lower acoustic impedance than that of the medium of propagation. A closed cell foam provides the required condition because of the low acoustic impedance it possesses whilst maintaining a semi-rigid structure; low impedance media tend to be gaseous and hence cannot be used to construct a waveguide. In contrast to the first case, the boundary conditions imposed by the pipe walls are that the pressure must vanish at the wall. For a circular waveguide this is equivalent to looking for the solutions to $J_n(k_{\mathrm{n,m}}a) = 0$. There is no solution and the propagation of plane waves is forbidden in this case. On inspection this result bears a great deal of similarity with the cut-off frequency exhibited by a closed cross-section

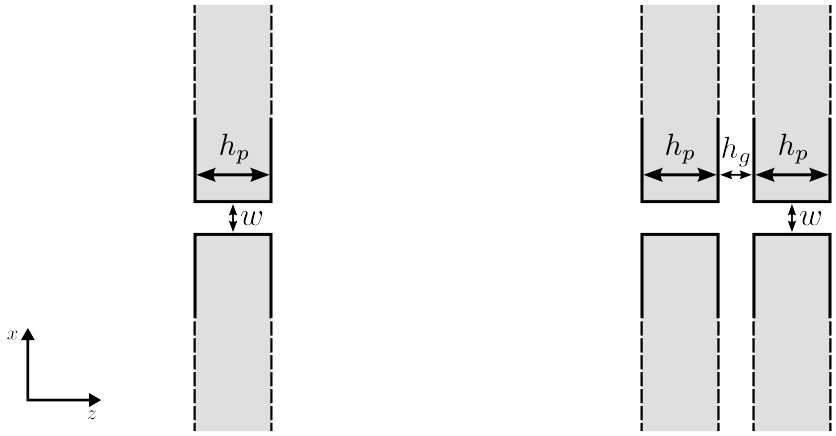

(a) Single Slit (b) Double Slit

Figure 9.1: Schematic diagram of (a) single foam slit and (b) double foam slit.

electromagnetic waveguide (i.e., not parallel plates).

Similarly, a slit formed from two parallel, acoustically soft plates will exhibit a cut-off frequency corresponding to $f = \frac{c}{2w}$, where w is the width of the slit. There is a significant difference between a slit in the acoustic and EM regimes, which arises due to the longitudinal nature of acoustic waves; the slit orientation is irrelevant acoustically whereas electromagnetically the orientation with respect to the orthogonal electric and magnetic fields contributes to the transmission properties. While a slit formed from two conducting, parallel plates exhibits no cut-off frequency when the electric field vector is parallel to the slit direction, a slit formed from two acoustically soft, parallel plates always exhibits a cut-off frequency, i.e., acoustically there is always a frequency below which no sound propagates in a soft walled slit.

Consider a single slit such as the one in figure 9.1(a), the cut-off frequency of which is given by $f = \frac{c}{2w}$. This is equivalent to stating that the transverse momentum $k_x = \frac{\pi}{w}$. At frequencies such that the incident wave has total momentum $k_0 > \frac{\pi}{w}$ a propagating wave exists within the slit. At frequencies such that $k_0 < \frac{\pi}{w}$, satisfying the condition imposed on the tangential momentum while conserving the total momentum requires that k_z is imaginary. This can be seen from $k_0 = \sqrt{k_x^2 + k_z^2}$ when $k_0 < k_x$ and hence the wave decays exponentially into the slit.

9.3 Wave Tunnelling

Tunnelling is a phenomenon most commonly associated with quantum mechanics, having been discovered by Becquerel in 1896 [68]. A particle possessing energy E may have

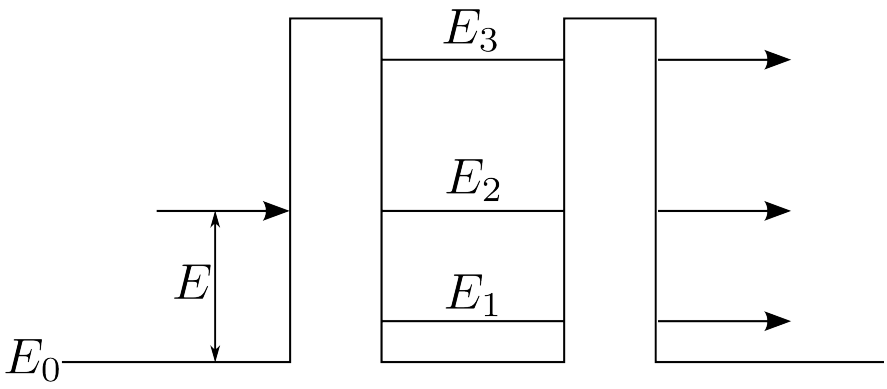

Figure 9.2: Schematic showing a wave incident with energy E upon a double barrier system. At energies $E_1, 2, 3$ corresponding to the energy levels of the double barrier the incident wave is completely transmitted.

insufficient energy to overcome a potential barrier with energy V, however there is still a probability that the particle may tunnel through the potential barrier. Several analogous phenomena exhibit similar behaviour to quantum tunnelling. Electromagnetically, extraordinary optical transmission has been attributed to the coupling of evanescent fields through holes perforated in a thin silver film [26]. Alternatively, light incident upon a dielectric medium will undergo total internal reflection beyond a critical angle as determined by Snell's law. Evanescent fields that exist at the interface have been used to couple power into a system placed in close proximity [69, 70].

The tunnelling transmission strength can approach unity when two barriers are placed in proximity, at frequencies corresponding to the resonant frequency of the cavity formed between the two barriers [71]. The resonance phenomenon bears similarities to that of an optical Fabry-Pérot etalon, which is typically an air cavity bounded by thin, parallel, metal films on each side [62]. A more appropriate analogy for the work presented is to the resonant tunnelling observed with a double tunnel barrier (see figure 9.2). Resonant acoustic tunnelling has been promoted as a possible route to achieving super-resolution imaging [72, 73]: Standard imaging techniques are limited by the wavelength of the sound or light being used to create an image. Sub-wavelength information contained within evanescent fields is confined to the surface and as such cannot be detected using standard methods. Resonant tunnelling provides a route for the information contained within the evanescent fields to be amplified and detected.

9.4 Samples and Modelling

Achieving a sound soft boundary whilst using air as a background medium is inherently difficult due to the low impedance of air. However, it is possible in water with the choice

of appropriate waveguide material. Water has an acoustic impedance of $Z = 1.47$ MPa, to achieve an acoustically soft interface a material with a lower impedance is required. The experimental samples are machined from a high density (200 kg/m^3) polyurethane (PU) foam plate with thickness, h_p. While the speed of sound in the foam is unknown, making the impedance difficult to determine, it is primarily composed by air and evidence suggests that the speed of sound in closed-cell, elastic foams is lower than that of the gas alone ([74]). As an approximation we take the speed of sound in air, 343 ms^{-1} which along with the density of the PU foam, 200 kgm^{-3}, gives an acoustic impedance of $Z = 68.6$ kPa, which is two orders of magnitude lower than that of water. Hence the PU foam provides the required soft boundary condition.

A central slit of thickness w is cut into the short-axis of a 150 mm $\times$ 200 mm $\times$ h_p plate of the PU foam (figure 9.1(a)). Due to its density, the foam is naturally buoyant in water and requires a heavy frame to submerse the sample. A metal frame is made that borders the foam plate and attaches to a heavy retort stand allowing the slit to be positioned underwater.

For the purposes of modelling the foam is assumed to impose a perfectly soft boundary condition. The considerable impedance mismatch between the foam and the water suggests this is a reasonable approximation. Additionally, sound propagation is assumed to be forbidden within the foam itself. In reality, sound will propagate through the foam itself, however as shown in figure 9.3 the level of the transmission is extremely low over the experimental frequency range due to the significant impedance mismatch between the foam and water. The transmission level is shown for an unstructured foam plate of thickness $h_\mathrm{p} = 10$ mm. The systems are modelled in two dimensions by surrounding the system in PML layers. The model geometry is shown in figure 9.4. A planar acoustic wave is launched from the orange shaded region through the slit. The boundaries of the slit and the surrounding region are highlighted green to indicated they are sound soft boundaries. The whole system is surrounded by PMLs, which are shaded blue. The transmittance is determined by integration of the time-averaged pressure field along the red line.

9.5 Acoustic Transmittance of a Single Slit in Polyurethane Foam

Consider a plate of PU foam which has a single slit machined into it (figure 9.1(a)). At frequencies below the cut-off of the slit, minimal transmission of sound is anticipated. As the frequency increases and approaches the cut-off frequency the transmission level will gradually increase as the evanescent sound wave tunnels through the slit. The

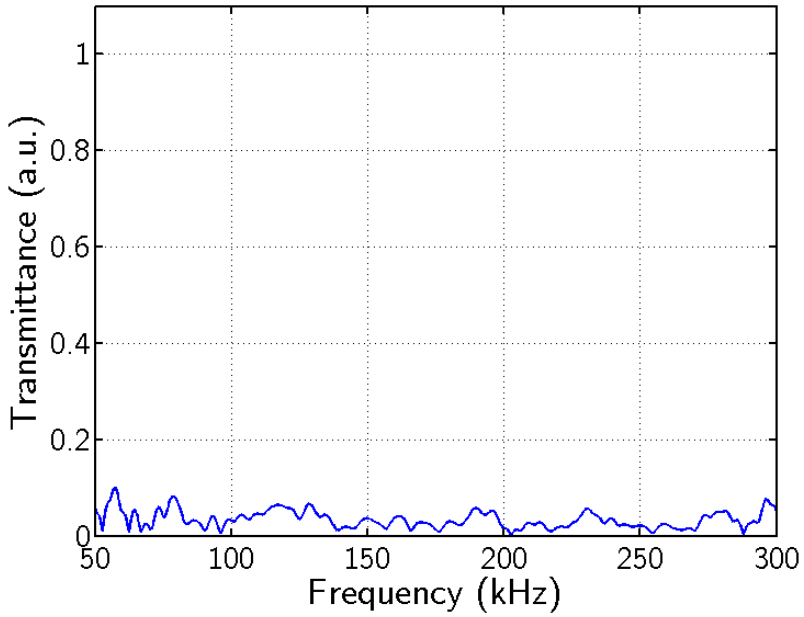

Figure 9.3: Acoustic transmittance through a 10 mm thick plate of PU foam.

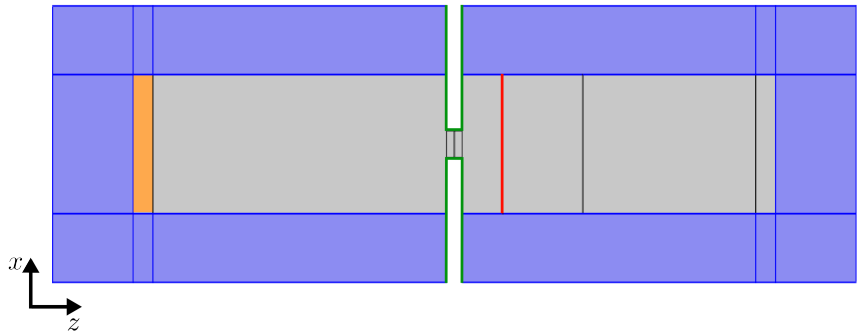

Figure 9.4: System used to model the transmission through foam slits. Perfectly matched layers are shaded blue, soft boundaries are highlighted in green, the acoustic wave is launched from the orange shaded region and the transmittance is determined by integration of the time-averaged pressure field along the red line.

rate at which this transmission level increases depends on the thickness of the foam plate, i.e. a long long slit will show a step change in transmission f_{cut} and a short slit will show a gradual increase in the transmission level as the frequency approaches f_{cut}. At frequencies above the cut-off frequency the sound is free to propagate through the waveguide and will be strongly transmitted.

9.5.1 Simulated Transmittance

Figure 9.5 shows the transmission of the soft-walled slit for a number of different thickness plates as simulated using FEM modelling. The width of the slit is $w = 4$ mm, which in water (using $c = 1470$ ms^{-1}, corresponding to standard temperature and pressure) corresponds to a cut-off frequency of $f_{\text{cut}} = 183.75$ kHz. The transmission of the thickest plate, $h_{\text{p}} = 20$ mm (black line) shows negligible transmission at frequencies below f_{cut} and strong transmission above f_{cut}. The transition from low to high transmission at f_{cut} is extremely rapid. As the thickness of the plate is reduced to $h_{\text{p}} = 10$ mm (blue line) and $h_{\text{p}} = 5$ mm (red line), the transition between low and high transmission is more gradual as expected. While at a single frequency the exponential decay rate of the evanescent fields is the same for any plate thickness, the amplitude of the fields at the output of the shorter slit will obviously be greater and hence a higher level of sound will tunnel through. However, the amplitude of the evanescent fields is greater at the exit of the slit for the thinner plates and hence the transmission level rises sooner but more gradually than the thicker plates. The series of peaks and troughs observed above f_{cut} (and weakly below f_{cut}) are artefacts of the modelling process, the origin of which could not be determined. They are not modes associated with the plate thickness, which would exhibit as a series of equally spaced peaks with the spacing dependent upon the thickness of the plate h_{p}.

9.5.2 Experimental Transmittance

Experimental results of the transmittance were obtained using the methods detailed in section 4.3. The source and detection transducers are separated by a distance of approximately 0.5 m with the output slit of the sample positioned approximately 1 cm from the detection transducer. Accurate measurement of the distances is inherently difficult due to the set up of the underwater testing facility.

Figure 9.6 shows the results of these experiments for two different thickness samples (blue lines) along with the predictions from FEM modelling (red lines). Figure 9.6(a) corresponds to a 2 mm thick plate and figure 9.6(b) corresponds to a 5 mm thick structure. The data shows good agreement with the predicted frequency of f_{cut}. As observed in the model, the rate at which the transmission increases as the frequency

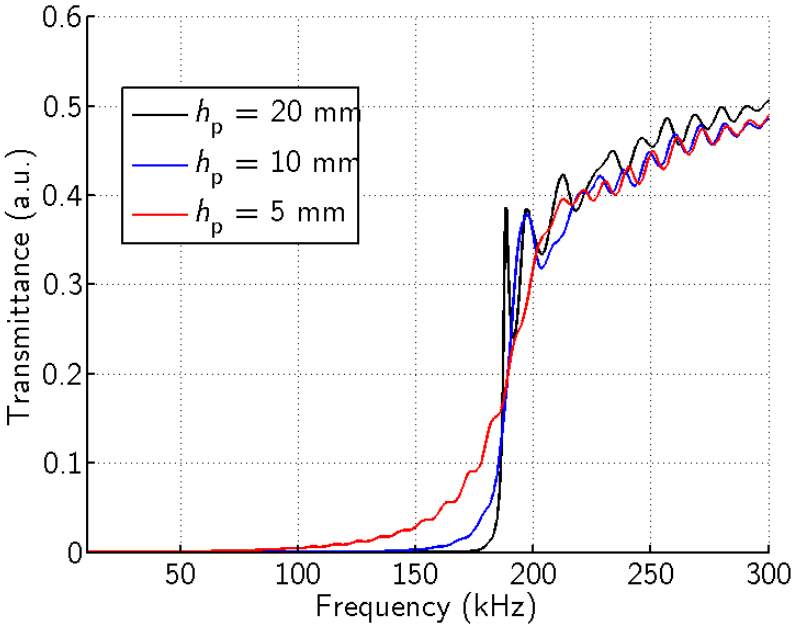

Figure 9.5: FEM simulated transmittance through a single slit with various thickness plates of PU foam.

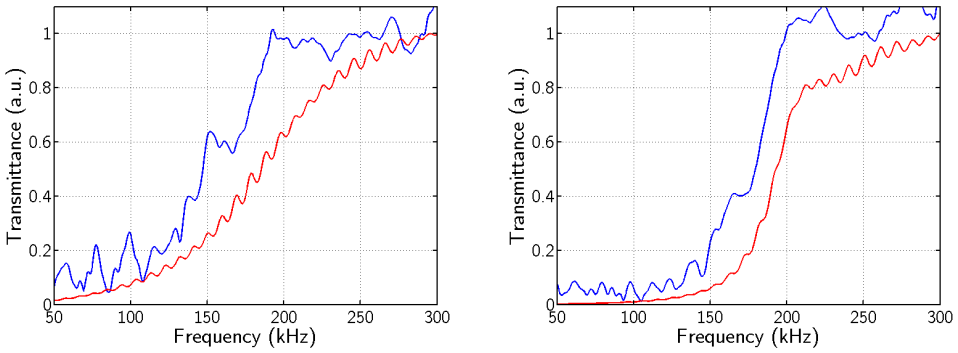

(a) $h_p = 2$ mm (b) $h_p = 5$ mm

Figure 9.6: Acoustic transmittance through a 4 mm wide slit in a (a) 2 mm and (b) 5 mm thick polyurethane foam plate.

approaches f_{cut} is more gradual for the thinner structure. This is due to the exponential decay of the fields within the slit being truncated at higher amplitudes in the thinner structure (i.e. thinner plates are less good mirrors).

9.6 Resonant Acoustic Tunnelling through Two Closely-Spaced Soft-walled Slits

Placement of a second identical foam plate as in figure 9.1(b), such that the slits are parallel, aligned and separated by a gap, h_{g}, creates a cavity between the two plates. Careful choice of the plate separation, h_{g}, such that a resonant mode of the gap lies below f_{cut} leads to the enhanced transmission of sound through the excitation of the gap mode.

9.6.1 Simulated Transmittance

Figure 9.7 shows the simulated transmittance for various values of h_{g} of two perfectly soft plates with thickness $h_{\text{p}} = 2$ mm that have had a slit machined into them. For the largest gap size, $h_{\text{g}} = 7$ mm, the fundamental resonance of the gap is 105 kHz (calculated from $f = \frac{c}{2h_{\text{g}}}$). This is just an estimate of the resonant frequency as end-effects will effectively increase the size of the gap. In the corresponding modelling (black line), a sharp peak in transmission can be seen at 100 kHz which accords with the simple prediction of 105 kHz. As the gap between the plates is reduced to $h_{\text{g}} = 6$ mm (blue line), $h_{\text{g}} = 5$ mm (red line) and $h_{\text{g}} = 4$ mm (green line) the transmission peak can be seen to shift upwards in frequency to 120 kHz, 135 kHz and 150 kHz respectively - these frequencies correspond to the resonant mode of the cavity between the two plates. The peak broadens as it approaches f_{cut} due to the slits become less good mirrors and the Q of the mode decreasing.

9.6.2 Experimental Transmittance

Experimental evidence of resonant acoustic tunnelling is provided by separating two PU foam plates with thickness $h_{\text{p}} = 2$ mm by a gap of $h_{\text{g}} = 4.8$ mm. Experimental data (blue line) shows a peak in the transmission strength at approximately 145 kHz while the corresponding model data shows a peak at a slightly lower frequency. While the experimental data does not agree with the FEM modelling data, there is a very clear peak in transmission that occurs well below the cut-off frequency of the slits. This peak is not observed in the transmission data for a single plate leading to the conclusion that the resonant tunnelling phenomenon has been demonstrated.

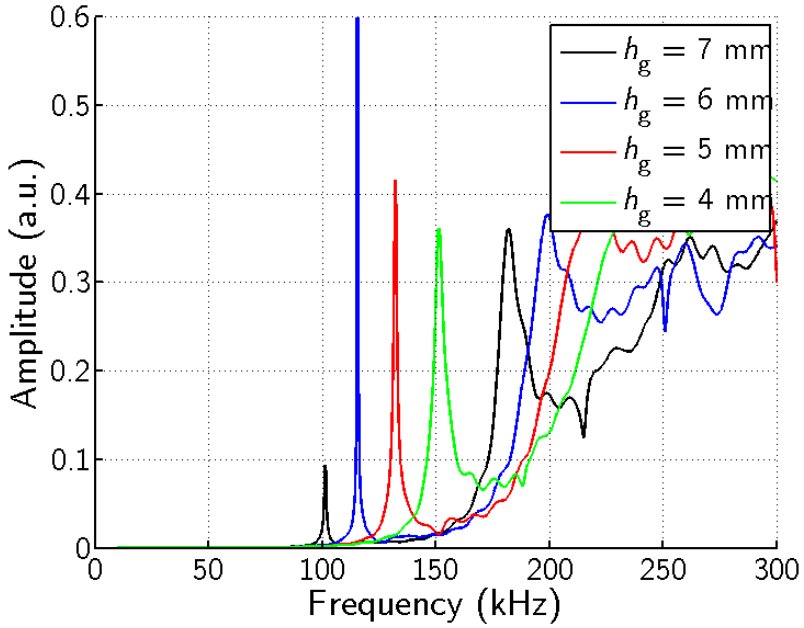

Figure 9.7: Simulated FEM transmittance through a pair of foam plates with a slit each plate, aligned with each other. The plate thickness is $h_p = 10$ mm and the plate separation h_g is varied from 4 mm to 7 mm.

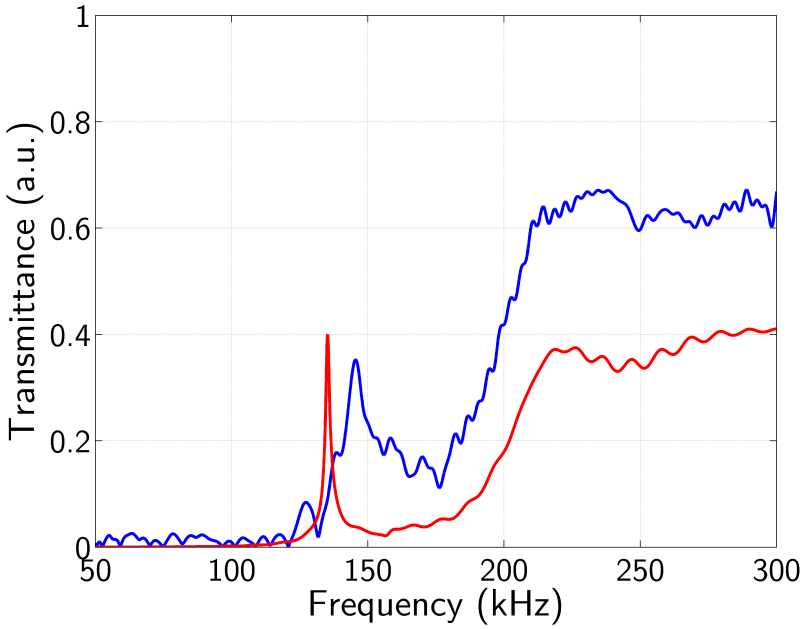

Figure 9.8: Experimental transmittance through a $w = 4$ mm wide slit in a pair of $h_p = 2$ mm thick polyurethane foam plates which are separated by a $h_g = 4.8$ mm gap (blue line). FEM modelling of the transmittance of the structure (red line).

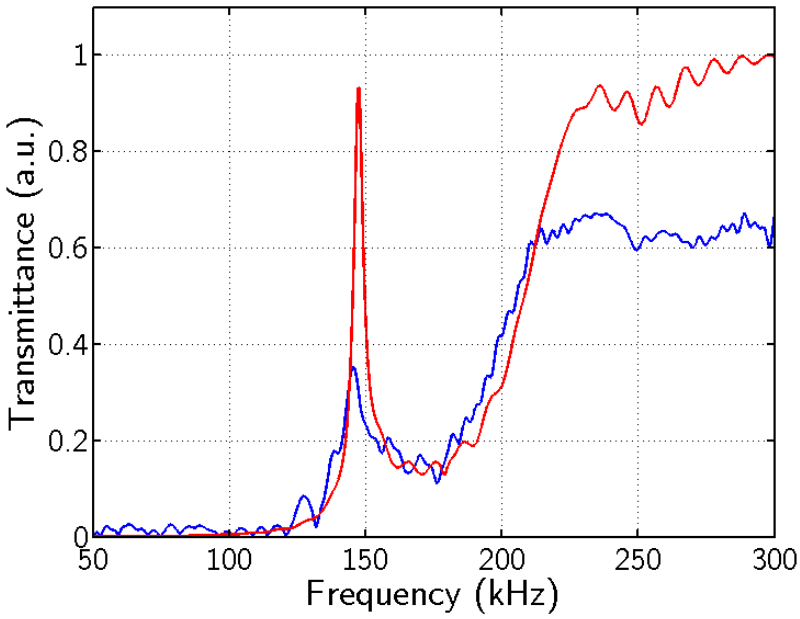

Figure 9.9: Experimental transmittance through a $w = 4$ mm wide slit in a pair of $h_p = 2$ mm thick polyurethane foam plates that are separated by an assumed $h_g = 4.8$ mm gap. FEM modelling of the transmittance with a modified gap of $h_g = 4.2$ mm (red line).

The FEM modelling can be fitted to the experimental data by assuming the gap size was reduced from $h_g = 4.8$ mm to $h_g = 4.2$ mm. This is shown in figure 9.9 where the experimental data is in excellent agreement with the FEM predictions.

It is possible that the frame holding the two plates exerted a compressive force on the foam plates leading to a slightly smaller gap as follows. The frame consists of a metal aperture (black framed rectangle) placed on either side of the foam plates (dark grey) with spacers (light grey) between the foam plates as in figure 9.10(a). Nuts on threaded pins around the edge of the frame hold the system together. If these nuts are overtightened then they will exert a compressive force, F, which could cause a reduction in the gap size as shown in figure 9.10(b).

9.7 Concluding Remarks

In this chapter we have demonstrated that a PU foam material can be structured with slits to act as a high pass filter. For sound propagating in water, the PU foam presents a soft acoustic boundary which forces a pressure node at the the interface between the water and the foam. This boundary condition prevents the propagation of plane wave

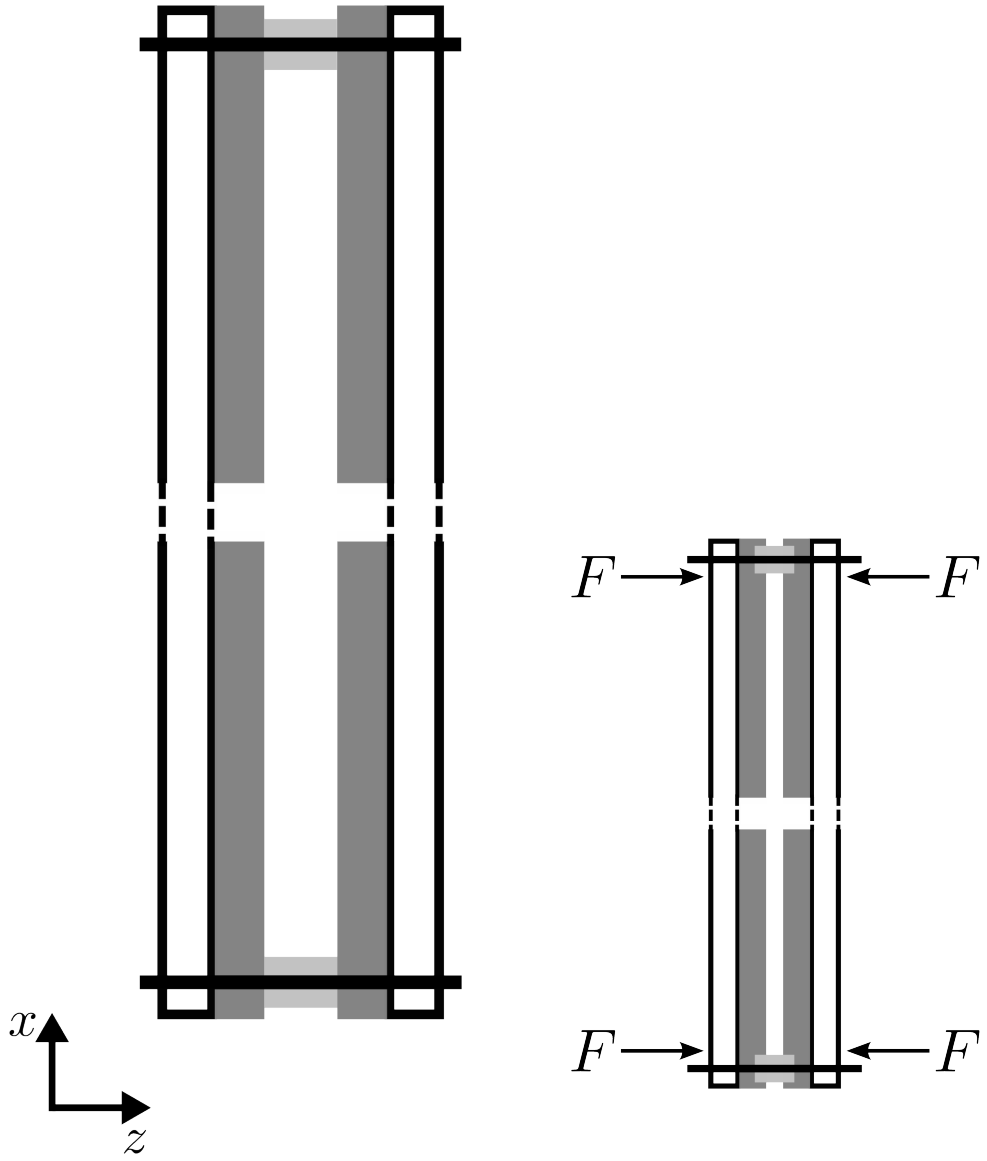

(a) Uncompressed (b) Compressed

Figure 9.10: Schematic diagram of sample in frame whilst (a) uncompressed and (b) compressed.

modes within the slit and as such the cut-off frequency is determined by the width of the slits. Unlike for electromagnetic radiation where the cut-off frequency of a slitted structure is only applicable to a single polarisation, the scalar nature of the acoustic field means that the cut-off frequency is always preventing the transmission of sound.

Placement of two such plates separated by a gap allows the resonant transmission of sound below f_{cut}. The frequency of this resonant tunnelling phenomenon is determined by the size of the gap, h_{g}, corresponding to the resonant end-to-end modes of the gap.

Chapter 10

Acoustic Pseudo-Surface-Waves on Rigid Slit Arrays

10.1 Introduction

Rigid, periodically structured surfaces, such as a periodic array of slits milled into an acoustically rigid solid will support a wave, which propagates along and is confined to the surface. Such a wave is labelled here as an acoustic pseudo-surface-wave (APSW) owing to the similarities with surface acoustic waves (SAWs). A preliminary study into APSWs is presented using an experimental method adapted from the electromagnetic regime. Hibbins *et al.* originally employed the method to provide experimental evidence for the analagous 'spoof' surface plasmon that is supported by a structured metal surface [18].

Section 10.2 provides a background to SAWs and APSWs. Section 10.3 presents the results of FEM simulations of two slit gratings and section 10.4 presents experimental data for the modelled surfaces.

10.2 Surface Acoustic Waves

At the surface of a material a wave may be supported with fields that are confined to the surface. The wave travels slower than a freely propagating wave due to the greater momentum it possesses in the direction of propagation compared to a freely propagating wave. The excess momentum in the direction of propagation is accounted for by an imaginary momentum in the direction perpendicular to the interface. The imaginary momentum component forces the fields to decay exponentially away from the surface, thus the wave is confined at the surface. Assuming a wave is propagating in the x direction at the interface of a surface this can be seen by considering the

angular frequency $\omega = ck_0$, where c is the speed of propagation and $k_0 = \sqrt{k_{\parallel}^2 + k_z^2}$ is the wavenumber; z is perpendicular to the surface. There are two main forms of SAWs, the first of which, the Rayleigh wave has particle oscillations perpendicular to the surface with a longitudinal component in the direction of motion in a the surface (see figure 10.1(a)) [7]. The second type, the Love wave has particle oscillations from side-to-side in the plane of the surface (see figure 10.1(b)) [8]. Both these waves occur during an earthquake and are responsible for the majority of the damage inflicted by an earthquake. There are other manifestations of the Rayleigh-type wave that occur in specific geometries [9, 10, 75]. There are other types of wave that exist, known as 'leaky surface acoustic waves', which consist of a term that decays into a substrate and a term describing a radiative component [76, 77].

In all cases, the surface wave requires the media of propagation to be elastic; as a surface becomes more rigid the frequency of the surface wave increases until for a perfectly rigid surface the surface wave only exists at infinite frequency. However, it is possible to support a wave that exhibits surface wave characteristics on a rigid structured surface, the APSW. In this case, the solid body can be assumed perfectly rigid while the structuring, for instance a series of slits, allows the acoustic field to penetrate the surface. This surface penetration effectively gives the surface a finite bulk modulus and allows it to support an APSW. A family of APSWs are supported that will disperse to asymptotic frequencies determined by the resonant modes of the structuring. In recent years APSWs have been studied on a number of structured surfaces [13–16] and have been attributed with enhancing the transmission through a structure and the collimation of sound [25]. Prior work on rigid perforated plates was undertaken by Norris and Luo [78] showing that the reflection is unity at frequencies determined by the double periodicity of the perforations (i.e. 2Λ). The feature they describe is a manifestation of the Rayleigh-Woods anomaly, however they also describe a number of features that occur at the cut-off frequencies of the perforations. These features are themselves manifestations of APSWs although they are not referred to in such a fashion.

Analogous non-radiative waves have been studied extensively in the electromagnetic regime [79–95]. The seminal work by Pendry [17] predicted that at the interface between a dielectric and a structured, highly conducting surface, a wave would be supported that displayed similar characteristics to a surface plasmon. A surface plasmon, first described by Ritchie [96], is a collective electron oscillation at a metal-dielectric interface. As a surface becomes more conducting, the surface plasmon frequency tends to infinity and is hence not supported on materials that may be approximated as perfect conductors, such as metals at microwave frequencies. The 'spoof' surface plasmon uses periodic surface

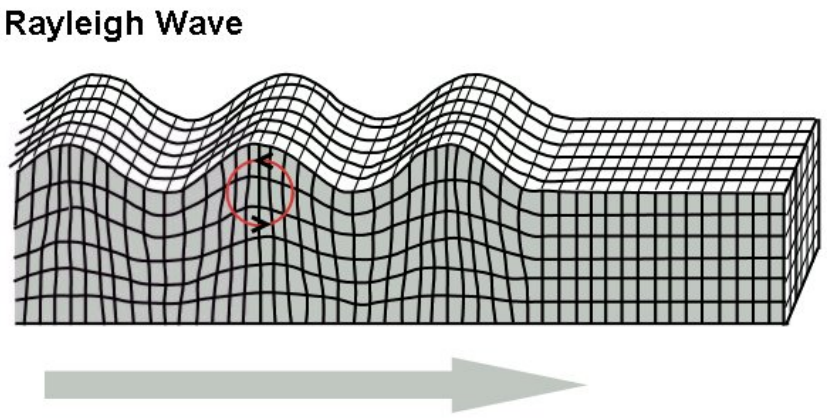

(a) Rayleigh Wave

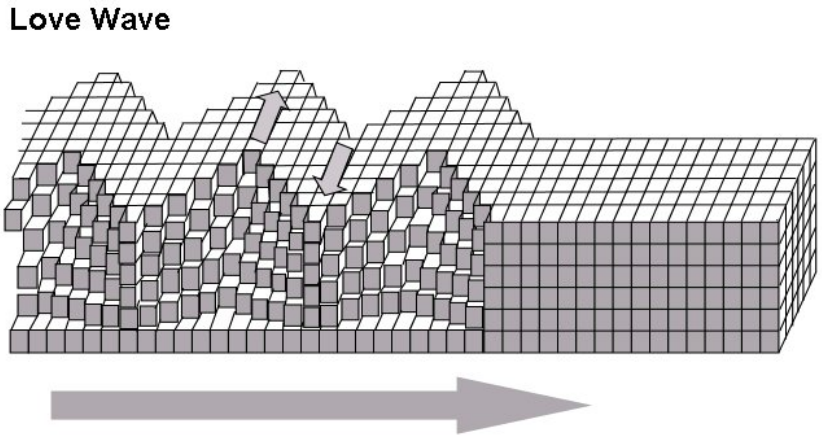

(b) Love Wave

Figure 10.1: Depictions of the surface motion associated with (a) Rayleigh waves and (b) Love waves. Images obtained from the Wikimedia Commons.

structuring to support a wave that is remarkably similar to the surface plasmon on a perfectly conducting surface. Experimental evidence for the 'spoof' surface plasmon for finite depth holes was subsequently provided by Hibbins *et al.* [18]. Pendry's original work focused on an array of infinitely deep holes in a perfectly conducting surface where the surface wave asymptotes to the cut off frequency associated with the holes; it was later realised that a the finite depth holes would support a family of modes, which asymptote instead at the resonances of the holes [19].

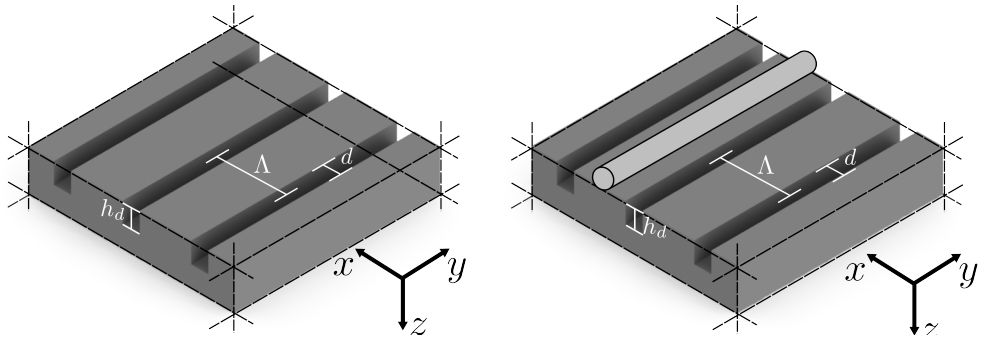

(a) Slits (b) Slits with grating

Figure 10.2: Geometry of the surfaces used in the surface wave experiments, (a) solid plate with array of slits milled into the the surface and (b) with the addition of a long pitch grating.

10.3 Simulated Dispersion of Structured Slits

Consider a rigid surface that has a periodic array of slits described by it as in figure 10.2(a). The pitch of the slits is Λ, the depth of the slits is h_d and the width of the slits is w. A resonant mode is found at a frequency determined primarily by the depth of the slit; with an end-correction made to the slit length. The fundamental resonance of the slit corresponds to fitting a quarter-wave into the depth of the slit, which after accounting for end corrections is calculated to be $f = 27.2$ kHz. The corrected depth of the slit is $h'_\mathrm{d} = h_\mathrm{d} + \Delta L$, where ΔL is the end-correction of a slit in an array as approximated by from equation (10.1) [97]. The equation is arrived at by matching the pressure and velocity functions of an incident plane wave across the entrance and exit of a periodic array of slits.

$$\Delta h_\mathrm{d} = \frac{d^2}{} \sum_{n=1}^{\infty} \frac{\sin^2\left(\frac{n\pi d}{\Lambda}\right)}{\left(\frac{n\pi d}{\Lambda}\right)^3}. \tag{10.1}$$

Approximating the summation with an integration leads to equation (10.2), which has been used to calculate the end-correction of the slits for the described surfaces [97].

$$\Delta h_\mathrm{d} \approx \left[\frac{1}{\pi}\left(\ln\left[\frac{1}{2}\tan\left(\frac{\pi d}{4\Lambda}\right) + \frac{1}{2}\cot\left(\frac{\pi d}{4\Lambda}\right)\right]\right)\right] d. \tag{10.2}$$

The limit of equation (10.2) for $d \to 0$ and $d \to \Lambda$ is zero as would be expected in both cases, as would be expected for a plate with no perforations and the limit of no plate. In addition to the quarter-wave resonance, the surface will support a bound APSW whose resonant frequency condition disperses to an asymptote equal to that of

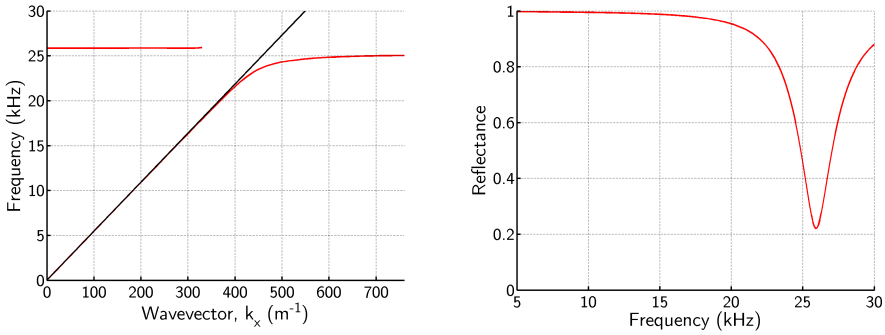

(a) Dispersion

(b) Reflectance at $\theta = 0°$

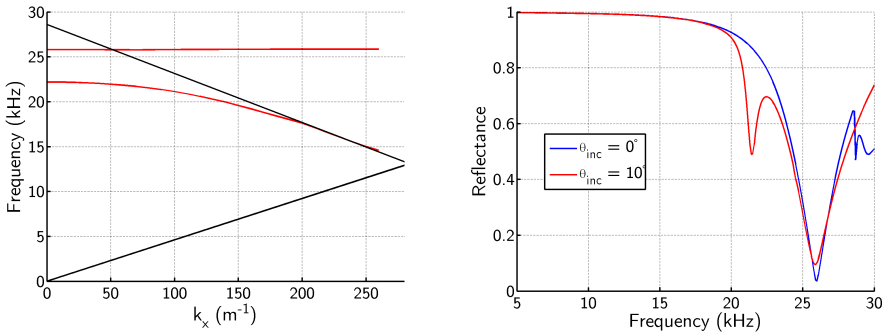

(c)

(d) Reflectance at $\theta = 10°$

Figure 10.3: (a) FEM prediction of the dispersion of the slitted surface and (b) simulated reflectance of the structure at normal incidence. (c) FEM determined dispersion plot of 200 µm slit sample after the addition of a 12 mm pitch grating and (d) simulated reflectance of the structure at normal incidence.

the quarter-wave resonance. Two surfaces are considered in this chapter, both having pitch $\Lambda = 4$ mm. The first sample has slit parameters $h_{\mathrm{d}} = 2.97$ mm and $d = 200$ µm, figure 10.2(a). FEM simulations are used to plot the dispersion of the supported APSW in figure 10.3(a) alongside the simulated normal incidence reflectance of the sample (figure 10.3(b)). As can be seen from figure 10.3(a), the asymptote of the APSW is at 25.9 kHz, which agrees with the trough observed in the reflection data in figure 10.3(b). The discrepancy between the observed resonant frequency of the slits and the predicted frequency is attributed to the effects of viscous losses in narrow slits, which can serve to reduce the speed of sound [98].

A modification to the sample is made by the addition of an array of metal rods, placed in contact with the sample, running between two slits with a period of 3Λ as shown in figure 10.2(b). This 3Λ grating causes a band-folding of the APSW about the Brillouin zone (BZ) boundary. Figure 10.4 shows an extended dispersion plot of the surface with and without the addition of a 3Λ grating. Blue lines correspond to the

modes supported by the unmodified surface and red lines correspond to the band-folded modes supported after the adddition of the 3Λ grating. (there are some discontinuties where the FEM simulation was unable to find the mode). Solid black lines correspond to the sound line and first diffracted sound line associated with the Λ periodicity and the dashed black lines correspond to the diffracted sound lines associated with the 3Λ grating. The dashed red lines indicate the BZ boundary associated with the 3Λ grating. The first order diffracted sound line associated with the rods crosses the frequency axis at 28.4 kHz allowing the APSW associated with this diffracted sound line to be coupled to by radiative acoustic waves. In the absence of the 3Λ grating, the APSW only exists outside the radiative regime, preventing the coupling of radiative waves to the APSW. As the diffracted sound line crosses the $k_x = 0$ axis a band gap will open up and the frequency of APSW will be reduced. Results of an FEM simulation predicting the dispersion of the surface is shown in figure 10.3(c) alongside simulated reflection data at $\theta_{\text{inc}} = 0°$ (red line) and $\theta_{\text{inc}} = 10°$ (blue line) in figure 10.3(d). The normal incidence data shows no dip in reflection associated with the APSW, however the $\theta_{\text{inc}} = 10°$ data shows an additional dip in the reflection at 21.4 kHz corresponding to the lower branch of the APSW. The upper branch of the band gap of the APSW is obscured by the strong coupling to the slit resonance. The coupling to the upper and lower branches will be discussed in section 10.3.1.

A second surface with slit width $d = 850$ µm and slit depth $h_{\text{d}} = 2.65$ mm is investigated where the width of the slits has been chosen to reduce the coupling strength of the quarter-wave resonance of the slit. This is achieved by widening the slit so that it is now over coupled. The fundamental mode of the slit is calculated to be $f = 29.0$ kHz. FEM modelling of the dispersion of the supported APSW is shown in figure 10.5(a) alongside the normal incidence reflectance of the structure in figure 10.5(b). The FEM modelling is unable to determine the mode corresponding to the quarter-wave resonance of the structure due to the modes low Q. A shallow dip (86% reflectance) centred on 28.2 kHz is seen in the reflection data that corresponds to the fundamental mode of the system. This frequency is slightly lower than the calculated frequency of 29 kHz, a discrepancy that is again attributed to the effects of viscous losses within the slits.

The surface is modified as before by the addition of an array of rods with pitch 3Λ on top of the surface as in figure 10.2(b). The dispersion of the surface is shown in figure 10.5(c) and reflection data at $\theta_{\text{inc}} = 0°$ (red line) and at $\theta_{\text{inc}} = 10°$ (blue line) are shown in figure 10.5(d). Normal incidence data shows a single dip in reflection corresponding with the upper branch of the APSW, which unlike for the previous surface is not obscured by strong coupling to the quarter-wave resonance of the slits. The $\theta_{\text{inc}} = 10°$ data shows an additional dip in the reflectance at 21.4 kHz corresponding to the lower branch of the APSW. In both datasets, the first-order diffracted sound line, which

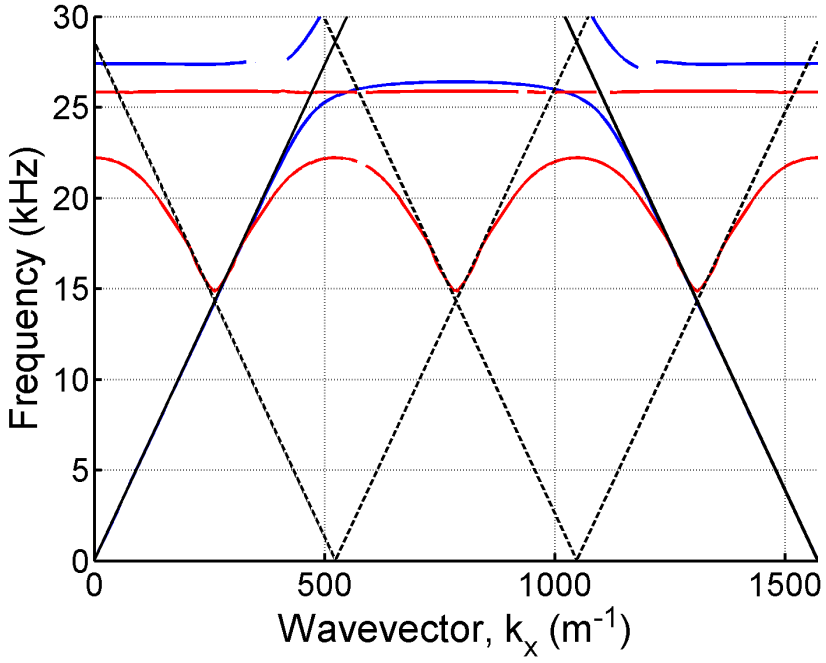

Figure 10.4: FEM simulation of the band structure of the slitted surface with (red lines) and without (blue lines) the addition of a 3Λ grating. Solid black lines correspond to the sound line and first diffracted sound line associated with Λ. Dashed black lines correspond to the additional diffracted sound lines associated with the 3Λ grating.

crosses $k_x = 0$ at 28.4 kHz obscures the broad quarter-wave resonance of the slits. The coupling to the upper and lower branches will be discussed further in section 10.3.1.

10.3.1 Pressure Field Profiles of Surface Modes

Both the modelled surfaces show no coupling to the lower branch of the APSW at normal incidence. A dip in the reflectance associated with the upper branch is clearly observed for the $d = 850$ µm surface however, the upper branch of the APSW for the $d = 200$ µm is obscured by the strong coupling to the quarter-wave resonance of the slits. At $\theta_{\text{inc}} = 10°$ both samples are observed to couple to the lower branch of the APSW. FEM modelling of the pressure profiles of both branches at $\theta_{\text{inc}} = 0°$ and $\theta_{\text{inc}} = 10°$ reveals that a symmetry condition forbids coupling at normal incidence (see figure 10.6). Red dashed lines in figure 10.6 mark the two symmetry points of the surface; the upper branch is symmetric about these lines and so can be coupled to at normal incidence; the lower branch is not symmetric about either of the lines and as such can only be coupled to at an oblique angle.

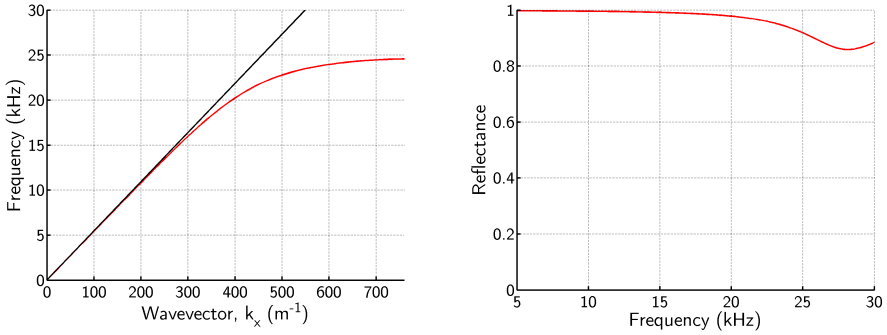

(a) Dispersion

(b) Reflectance at $\theta_{\text{inc}} = 0°$

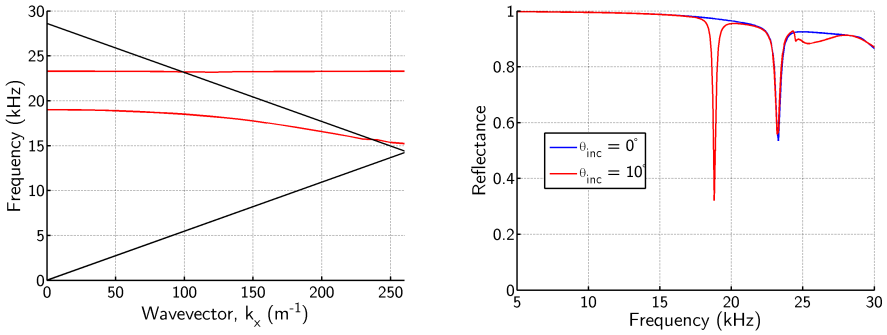

(c)

(d) Reflectance at $\theta_{\text{inc}} = 0°$

Figure 10.5: (a) FEM predicted dispersion of the $d = 850$ µm slit sample and (b) simulated reflectance of the structure at normal incidence. (c) Dispersion plot of the sample after the addition of a 12 mm pitch grating and (d) simulated reflectance of the structure at $\theta_{\text{inc}} = 0°$ and $\theta_{\text{inc}} = 10°$.

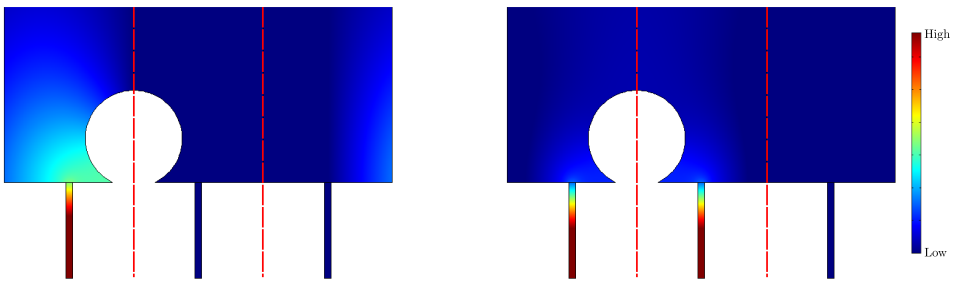

(a) Lower branch

(b) Upper branch

Figure 10.6: (a) Instantaneous pressure profile of lower branch of the APSW at normal incidence. (b) Instantaneous pressure profile of upper branch of the APSW at normal incidence.

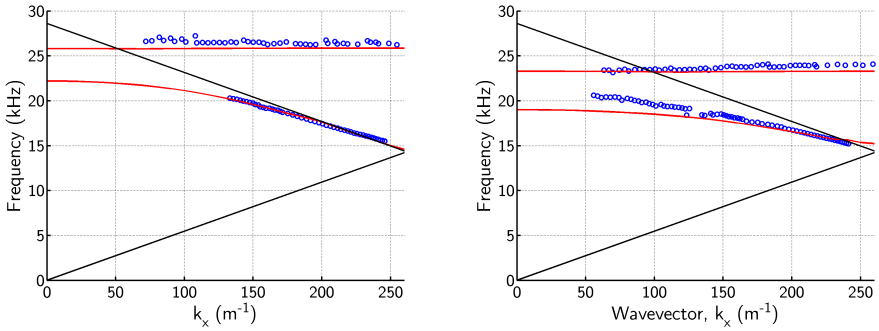

(a) (b)

Figure 10.7: Dispersion plots of the samples. (a) $w = 200$ µm, $h_d = 2.97$ mm and $\Lambda = 4$ mm, and (a) $w = 850$ µm, $h_d = 2.65$ mm and $\Lambda = 4$ mm.

10.4 Experimental Dispersion of Slitted Surfaces

Samples to match the modelled surfaces discused above are machined from 400 mm × 400 mm × 6 mm perspex plates. Milled into sample A is a periodic array slits of pitch $\Lambda = 4$ mm, depth $h_d = 2.97$ mm and slit width $d = 200$ µm as shown in figure 10.2(a). Sample B is machined with parameters $\Lambda = 4$ mm, depth $h_d = 2.65$ mm and slit width $d = 850$ µm.

Experimental data of the dispersion of the APSW for both samples is obtained using the reflection set up detailed in section 4.2.4. The reflectance of the samples is obtained between $\theta_{inc} = 8.5°$-$30°$ in $0.5°$ increments and from $\theta_{inc} = 30°$-$60°$ in $1°$ increments. Dips in the reflectance correspond to the diffractive coupling of the incident wave to the APSW. The dips are used in conjunction with the phase data (section 4.4) to map out the dispersion of each sample. Figures 10.7(a) and 10.7(b) plot the data for the $w = 200$ µm and the $w = 850$ µm samples respectively. It must be noted that the upper branch plotted for the $w = 200$ µm sample is actually the quarter-wave resonance rather than the upper branch of the APSW. As mentioned above, the upper brance of the APSW is obscured by the strong coupling to the quarter-wave resonance.

Figure 10.7(a) shows experimental data for the w =200 µm slits that is in accordance with the predicted dispersion from FEM modelling. The upper branch of the experimental data is very slightly higher in frequency than the simulated data and the lower branch cannot be resolved at smaller angles of incidence due to weaker coupling. Figure 10.7(b) shows experimental data for the $w = 850$ µm slits and clearly shows a disagreement with the modelling. The explanation for which is as follows.

The FEM modelling makes the assumption that the rods forming the long pitch grating are in contact with the surface. If the rods are instead raised above the surface

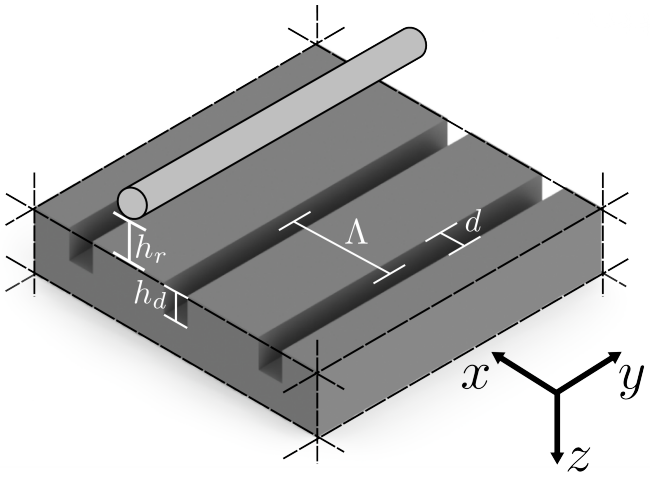

Figure 10.8: Modified geometry of the surface with rods raised vertically above the surface by a height, h_r.

slightly, the simulated data can be made to fit the experimental data extremely well. In the modified simulation, the rods are raised above the surface by empirically determined values of 400 µm for the $w = 850$ µm slit sample. The experimental and modified simulation data shown in figure 10.9 is now in agreement. The origins of this gap between the rods and the surface is due to a curvature induced into the sample by machining the slits into the sample. This curvature is negligible in sample A due to the narrower slits and hence the simulation data does not require modification. The curvature is more pronounced for the sample with larger slits and thus a gap between the rods and the surface is introduced for the $w = 850$ µm sample.

10.5 Concluding Remarks

In this chapter we have experimentally demonstrated a method for detecting surface waves that was previously unused in the acoustics regime. Data was obtained for a rectangular groove grating with pitch $\Lambda = 4$ mm, depth $h_\mathrm{d} \approx 3$ mm, slit width $d = 200$ µm and a similar structure with slit width $w = 850$ µm. Agreement between experiment and modelling was achieved by varying the height of the long pitch grating above the surface. Varying the height of the gap between the rods and the surface can be used to tailor the dispersion of the APSW.

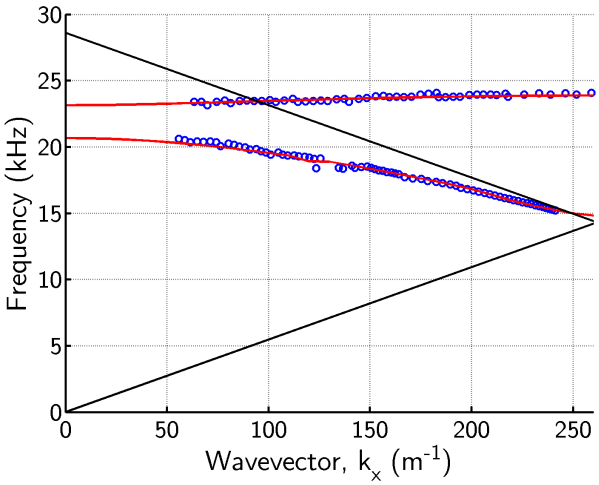

Figure 10.9: Experimental (blue points) and modified simulated data (red line) for the dispersion of the APSW on the $w = 850$ µm sample.

Chapter 11

Conclusions and Future Work

11.1 Introduction

This thesis has presented original investigations into the acoustic transmission and reflection properties of structured plates. The thesis can be broadly split into three sections, the first comprising the investigations presented in chapters 5, 6 and 7. Through these chapters a comprehensive study of the transmission properties of rigid, perforated plates is developed; starting with the transmission properties of a single perforated plate, to the transmission properties of pair of stacked plates separated by a narrow gap and culminating in a study of the transmission properties of stacked plates with a structured gap. The second thesis section is comprised of chapters 8, 9 where the effect of varying the material properties of the propagation media and the plate are explored. Finally, in chapter 10 an investigation into the pseudo surface acoustic waves supported on periodic structured surfaces is presented.

11.1.1 Summary of Thesis

Chapter 5 looked at the acoustic transmittance of single and double fishnet structures both numerically and experimentally. The transmittance of the single fishnet exhibited a series of transmission peaks at frequencies corresponding to the excitation of pipe modes. The double fishnet was shown to exhibit a similar family of transmission peaks, again associated with the excitation of pipe resonances at frequencies determined by the total thickness of the structure. However, while the even-order modes were unperturbed by the gap between the plates, the odd-order modes were modified in frequency from where they would be expected to lie in the absence of the gap due to coupling to a mode of the gap. An acoustic stop-band corresponding to the resonant excitation of the mode of the gap was shown and demonstrated to be unaffected by the thickness of the plates.

Allowing one of the plates to differ in thickness from the other, which is equivalent to shifting the position of a resonant side branch along a single long pipe, similarly has no effect on the frequency of the stop-band. Similar work has been undertaken previously both theoretically [36] and experimentally [35]; where this chapter has extended this prior work is by considering the effect of constructing the double fishnet with two different thickness plates.

Chapter 6 further investigated the acoustic transmittance of the double fishnet as a function of the angle of incidence, the plate offset, and the gap size. As predicted by prior research [36], the stop-band of the double fishnet was shown to be largely unaffected by the angle of incidence. The effect of misaligning the plates has not previously been considered and varying the gap between the plates has only considered in a limited way - and the gap was maintained as sub-wavelength. This chapter showed that varying the plate offset h_{off}, or the gap size h_{g}, allowed the frequency of the acoustic stop-band to be controlled. However, the frequency shift was only to higher frequencies as either parameter was increased. For the case of hole misalignment, the frequency of the stop-band is approximately determined by the shortest distance between the corner of the unit cell and the perimeter of a circular nodal line, centred on the input hole, with radius equal to h_{off}. For the case of varying gap size, a similar case arose whereby the frequency of the stop-band is approximately determined by the shortest distance between the corner of the unit cell and the surface of a hemispherical nodal line, centred on the input hole at $\frac{h_{\text{g}}}{2}$ with radius $\frac{h_{\text{g}}}{2}$. Increasing the gap size further allowed end-to-end modes within the gap to be excited (i.e., with the front at back plates acting as partial mirrors). These modes were subsequently shown to provide an additional condition for enhanced acoustic transmission. The coupling of the end-to-end modes with the pipe modes of the double fishnet led to a condition where three resonant modes occur within a narrow frequency band.

Chapter 7 modified the double fishnet such that the gap between the plates behaved as an array of Helmholtz resonators. The acoustic transmittance of the modified structure, referred to as the Helmholtz double fishnet, was investigated analytically, numerically and experimentally. An acoustic stop-band was found at a considerably lower frequency than the stop-band of the equivalent size double fishnet. Modification of the double fishnet structure was achieved through the introduction of a bi-grating of grooves into the internal side of each fishnet i.e., the walls of the gap. The HDF may improve the viability of fishnet structures for use as a thin and lightweight sound screening devices that simultaneously allow air flow. However, the lower frequency stop-band has the potentially unwanted side-effect of introducing a transmission resonance at a frequency lower than both the fundamental resonance (in the absence of the gap) and the stop-band itself. Considerable research has gone into creating thin and lightweight

structures that prevent the transmission of low frequency sound, this chapter explored one such method that could readily be designed to operate at much lower frequencies.

Chapter 8 returned to the single fishnet structure and investigated the geometric intromission of sound. Prior work has shown that complete transmission of sound can be achieved at high angles of incidence. Intromission can occur easily at low angles of incidence if the hole aperture ratio is large, however in this case the structure will appear acoustically transparent anyway. It was numerically demonstrated that through careful choice of the media surrounding the single fishnet and within the holes geometric intromission can occur at normal incidence. In contrast to a recent study demonstrating the same effect under the assumption that air is incompressible [45], a system was proposed that is experimentally realisable.

Chapter 9 demonstrated that an acoustically soft material (poly-urethane foam) structured with a slit forbids the propagation of plane waves within the slit. The result of this is that sound is prevented from propagating at frequencies below a cut-off frequency determined by the width of the slit. In the equivalent experiment for the case of electromagnetic radiation (a metal plate structure with a slit) the cut-off frequency of a slitted structure is only applicable to a single polarisation. Placement of two such plates parallel to each other, with the slits aligned and separated by a gap allows the resonant transmission of sound below f_{cut}. The frequency of this resonant tunnelling phenomenon is determined by the size of the gap, h_{g}, corresponding to the resonant end-to-end modes of the gap. The system bares a strong resemblance to the quantum phenomena of a resonant tunnelling diode [99] but has not previously been demonstrated acoustically. Resonant acoustic tunnelling has recently been proposed as a path to super-resolution imaging [73]. Having demonstrated experimentally resonant acoustic tunnelling we would seek to demonstrate super-resolution imaging experimentally through its implementation.

Chapter 10 looked at acoustic pseudo-surface-waves supported on periodic slit arrays. These confined waves are normally non-radiative and cannot be coupled to with radiative waves. The addition of a longer pitch grating on top of the surface allows coupling of incident acoustic radiation to the band-folded APSW associated with the first diffracted sound line of the long pitch grating. Such waves have been explored previously on a number of surfaces using other methods. The work in this chapter adapted an experimental method from analogous work on spoof surface plasmons into the acoustic regime.

Overall the experimental, numerical and analytical studies presented within this thesis have shown that structural geometry can be used to tailor the transmission and reflection response of the structures. Experimental results are generally in good agreement with numerical simulations. Analytic modelling of the presented material

provides considerable insight into the underlying physics of the observed response.

11.2 Future Work

In this section some suggestions of future work stemming from the work presented are considered. The first section relates to the work presented in chapters 5 and 6. It is proposed that the inherently narrow acoustic stop-band associated with the double fishnet structure could be effectively broadened by combining multiple plates together. The second section proposes how the theoretical work on acoustic intromission, presented in chapter 8, could be achieved experimentally. Thirdly, a number of suggestions are proposed for furthering the investigation of resonant acoustic tunnelling presented in chapter 9. Finally, a range of ideas for further exploration of the APSWs presented in chapter 10 are provided.

11.2.1 Broadening the Acoustic Stop Band of the Double Fishnet by Combining Multiple Fishnets

The stop-band of the double fishnet is inherently narrow banded owing to its resonant nature. To increase the bandwidth we propose stacking a number of plates together to form a multi fishnet structure. Figure 11.1(a) compares modelling of the transmittance of three structures, a single fishnet with $h_{\mathrm{p}} = 12$ mm, a double fishnet with $h_{\mathrm{p}} = 5.94$ mm and a quadruple fishnet with $h_{\mathrm{p}} = 2.97$ mm. The gap size(s) for the double and quadruple fishnets are $h_{\mathrm{g}} = 0.94$ mm. Compared to the single fishnet, the double fishnet reduces the transmittance across the frequency range except at transmission resonances and introduces an acoustic stop-band at 18.5 kHz. The quadruple fishnet reduces the transmission level across the frequency range further and enhances the transmission loss at the stop-band. By itself, this is an unsurprising result as we introduced more impedances mismatches for the sound wave to cross and we have to acoustic stop-bands, at the same frequency, acting in series. However, combined with the knowledge that varying the gap size (or the plate offset) allows control of the stop-band frequency allows us to effectively broaden the bandwidth of the stop-band. Figure 11.1(b) shows modelling of the transmittance three distinct quadruple fishnets. Plot (a) corresponds to the case where $h_{\mathrm{g}_{1,2,3}} = 0.94$ mm, plot (b) corresponds to the case where $h_{\mathrm{g}_1} = 0.47$ mm, $h_{\mathrm{g}_2} = 0.94$ mm and $h_{\mathrm{g}_3} = 1.41$ mm, and Plot (c) corresponds to the case where $h_{\mathrm{g}_1} = 0.47$ mm, $h_{\mathrm{g}_2} = 1.41$ mm and $h_{\mathrm{g}_3} = 1.88$ mm; the subscript enumerations refer to the three gaps that are present in the quadruple fishnet. Individual stop-bands associated with each gap are clearly seen as sharp troughs and it is clear that varying the gap size in this way offers an effective way of broadening the stop-band.

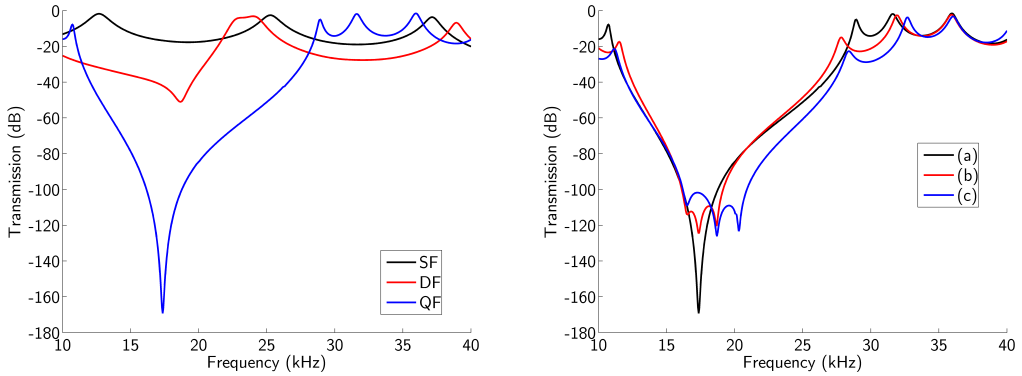

(a) (b)

Figure 11.1: (a) Modelled data of the transmission through a single fishnet with plate thickness $h_p = 12$ mm, a double fishnet with plate thickness $h_p = 5.94$ mm plates and a quadruple fishnet with plate thickness $h_p = 2.97$ mm. Where relevant, the gap size $h_g = 0.94$ mm. (b) Modelled data of the transmission through a QF with plate thickness $h_p = 2.97$ mm for (a) $h_{g1,2,3} = 0.94$ mm, (b) $h_{g1} = 0.47$ mm, $h_{g2} = 0.94$ mm, $h_{g3} = 1.41$ mm and (c) $h_{g1} = 0.47$ mm, $h_{g2} = 1.41$ mm, $h_{g3} = 1.88$ mm.

The above suggestions could be readily incorporated with the the work on the Helmholtz double fishnet presented in chapter 7. Although, the effect of offsetting the plates is likely to have a considerable effect on the resonant frequency of the gap region.

11.2.2 Proposal for Experimental Demonstration of Acoustic Intromission at Normal Incidence

The transmittance of rigid plates perforated with an array of holes has been considered extensively throughout this thesis. The transmission level is less than unity except on resonance and for obvious reasons, being lower in magnitude for smaller ratios of the hole area to unit cell size. At the angle of intromission, which is at greater angles of incidence for smaller holes, the impedance of the incident wave and the wave in the hole is the same; the plate effectively becomes acoustically transparent. Appropriate choice of the incident and transmission media along with a suitable choice of the media within the holes would allow intromission to occur at normal incidence. In chapter 8 a proposal was made that in a water environment, with silicon oil filling the holes - with these choices of fluid, normal incidence intromission would occur for a hole aperture size ratio of 0.53. For such large holes, the acoustic transmission would be relatively high anyway, however with further investigation there may be other fluid options where complete transmission would occur for much smaller holes.

One of the main difficulties in arranging such an experiment is in preventing the two

fluids from mixing. This could be achieved through the use of a thin membrane separating the fluids. While the membrane would have inherent resonances, the frequency of these resonances could be shifted by appropriate tensioning of the membrane.

Additionally, there is the unresolved issue why the pipe resonances associated with the thickness of the rigid plate can still be observed at the angle of intromission. These modes arise from an impedance mismatch at the entrance and exit to each aperture, which creates a parallel pair of partial mirrors. At the intromission angle, the impedance across the boundary is matched and the structure should effectively appear transparent. Clearly the explanation of the intromission phenomenon is overly simplified.

11.2.3 Expansion of Studies into Resonant Acoustic Tunnelling

There is a wide scope for work to be undertaken investigating resonant acoustic tunnelling. The work presented in chapter 9 covered only the transmission through a single slit; it is likely that the signal-to-noise could be improved by using an array of slits. This is likely a vital first step as the transmitted signal could only be detected when the hydrophone sensor was in close proximity (a few cm) to the output side of the slit.

The process of milling the slit into thin sheets of foam was not ideal and could be made vastly simpler by replacing the slit with a hole, or an array of holes.

It was mentioned in chapter 9 that the utility of resonant acoustic tunnelling could be in sub-wavelength imaging. Assuming the signal-to-noise could be improved by methods including those above, it would be desirable to test whether sub-wavelength imaging could be achieved. At this stage the arrangement of such an experiment is unknown.

11.2.4 Development of New Structures for the In-Plane Control of Pseudo Acoustic Surface Waves

APSWs were detected in chapter 10 by the diffractive coupling of incident acoustic radiation to the band-folded modes; achieved through the addition of a long pitch grating above the surface. One avenue briefly explored in chapter 10 was the effect of the height of the grating above the surface. This effect could be more fully investigated to better understand how the coupling strength depends on the proximity of the rod grating to the surface. Similarly, the effect of rotating the grating azimuthally on the sample would provide an additional avenue of investigation.

The method of detection employed can not be utilised to map the fields of the supported surface waves. Development of an alternate method that would allow for 2D/3D mapping of the fields above the surface would allow the investigation of novel acoustic structures. Structures such as a surface wave "omni-directional absorber", or

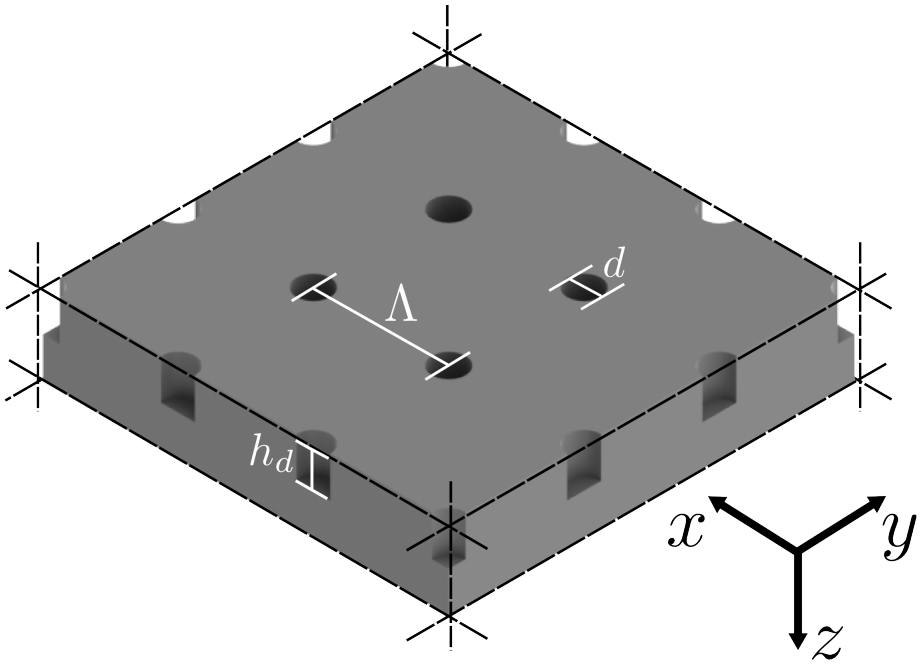

Figure 11.2: Schematic diagram of the square array of holes with pitch Λ, hole diameter d and hole depth h_d.

any surface designed to control the propagation of sound over the surface would be of considerable interest. The asymptote frequency of the APSW dispersion is determined primarily by the depth and shape of the holes or slits on a surface; by varying the geometry of holes across the surface, the propagation speed of the wave can be controlled and hence the propagation path. This could be utilised to direct surface waves provide in-plane control of the propagation of APSWs.

To illustrate how the propagation speed of the APSW changes with hole depth, FEM modelling of a hole array was undertaken (see figure 11.2). The propagation speed of the APSW is determined by the gradient of the dispersion, given by $v = \frac{\partial \omega}{\partial k}$. A square array of holes with pitch $\Lambda = 4$ mm is modelled, the hole diameter is 1 mm and the depth is varied from 3 mm to 6 mm. Figure 11.3 plots the mode index of the surface wave against frequency. The mode index, n, is defined as $n = \frac{c}{v}$ where c is the speed of sound in air and v is the propagation speed of the APSW. It is clear that for a single frequency, the APSW will propagate at a different speed over different surfaces and varies considerably for different hole depths. If it is assumed that the propagation speed is largely unaffected by different depth holes surrounding an individual holes, then a variety of surfaces could be investigated. Potentially the most useful is that of an "omni-directional absorber", which could act as an acoustic absorber or potentially an energy harvester.

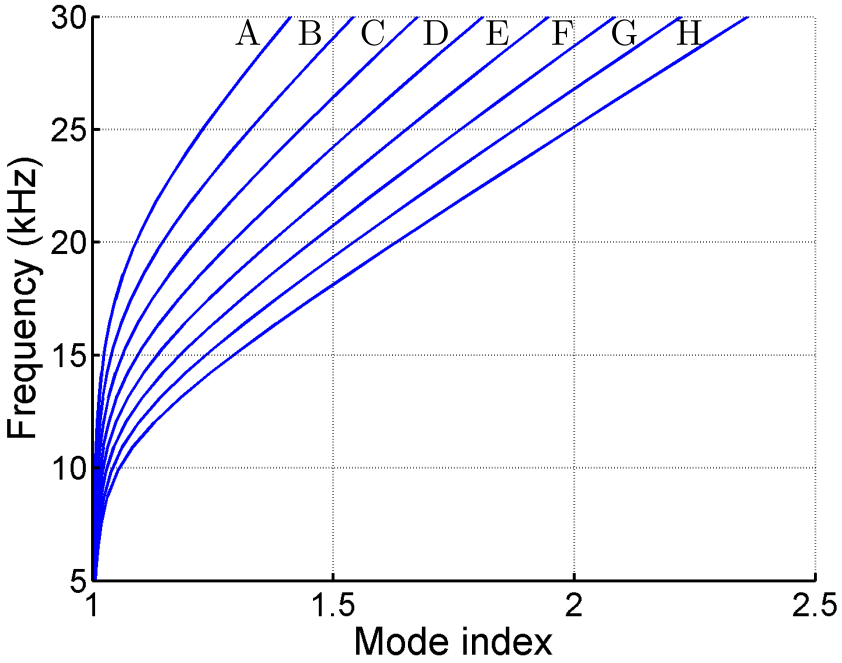

Figure 11.3: Mode speed of the APSW supported on a square array of closed-ended holes. The pitch of the hole array $\Lambda = 4$ mm, the diameter of the holes $d = 1$ mm and the hole depth h_{d} is varied from 3-6.5 mm in increments of 0.5 mm, corresponding to lines A-H respectively.

11.3 Publications

- Bell, J.S., Summers, I.R., Murray, A.R.J., Hendry, E., Sambles, J.R., and Hibbins, A.P. Low acoustic transmittance through a holey structure. *Physical Review B*, **85**, 214305 (2012)

- Murray, A.R.J., Hendry, E., Summers, I.R., Sambles, J.R., and Hibbins, A.P. Control of the stop band of an acoustic double fishnet. *The Journal of the Acoustical Society of America*, **134**, 1754 (2013)

- Lovelock, R., Murray, A.R.J., Ward, G.P., Hibbins, A.P., Sambles, J.R., and Smith, J.D. Slit Width Dependence of the Acoustic Transmission through a Thin Slit. *(Submitted)* (2014)

- Murray, A.R.J., Summers, I.R., Sambles, J.R., and Hibbins, A.P. Acoustic double fishnet using Helmholtz resonators. *The Journal of the Acoustical Society of America*, **Accepted** (2014)

- Carretero-Palacios, S., Murray, A.R.J., Martín-Moreno, L., and Hi-

BBINS, A.P. Broadband and broadangle extraordinary acoustic transmission through subwavelength apertures surrounded by fluids. *New Journal of Physics*, **16**, 083044 (2014)

11.4 Conferences

- Metamaterials 2011 - *5th International Congress on Advanced Electromagnetic Materials in Microwaves and Optics*, Barcelona, Spain - Poster
- Meta' 12 - *3rd International Conference on Metamaterials, Photonic Crystals and Plasmonics*, Paris, France - Talk
- ECUA 2012 - *11th European Conference on Underwater Acoustics*, Edinburgh, Scotland - Talk

Appendices

Appendix A

Single Fishnet Modal Matching Code

Here a full derivation is provided for the modal matching method used to simulate the transmittance of a plane acoustic wave incident upon a SF structure. This final expression is used in chapters 5 and 8. In chapter 8 the fluid media within the pipe is allowed to vary and the expression for the transmittance is derived as such.

First the SF is split into three regions, the region before the plate, the region within the holes, and the region after the plate. The plate itself is assumed to be rigid. The z axis is along the pipe[1] and the x-y plane describing the face of the plate with the front face of the SF at $z = 0$ (figure A.1). Ignoring the time dependence, which divides out, a plane wave defined by its pressure field is incident upon the SF with wavevectors k_x, k_y and k_z in the x, y and z axes. The reflected wave is defined in terms of a Fourier-Floquet expansion.

$$\begin{aligned} p_{\mathrm{I}} &= \exp\left[i\left(k_z z + k_x x + k_y y\right)\right] \\ &+ R\left[m_1, m_2\right] \exp\left[i\left(\left(k_x + \frac{2\pi m_1}{d}\right)x + \left(k_y + \frac{2\pi m_2}{d}\right)y - k_z\left[m1, m2\right]z\right)\right], \end{aligned} \tag{A.1}$$

the dimensions of the hole array are sub-wavelength and the wave within the cavity is described by the lowest order waveguide mode, i.e. a simple plane wave:

$$p_{\mathrm{II}} = A_1 \exp\left[ik_0' z\right] + A_2 \exp\left[-ik_0' z\right], \tag{A.2}$$

where the ($'$) suffix indicates the variable is measured in the hole region. The trans-

[1] While the experimental samples in chapter 5 have circular holes, the modelling assumes square holes. As only the plane wave mode of propagation is allowed within the pipe shape of the aperture is not critical as long as the area of the hole is maintained.

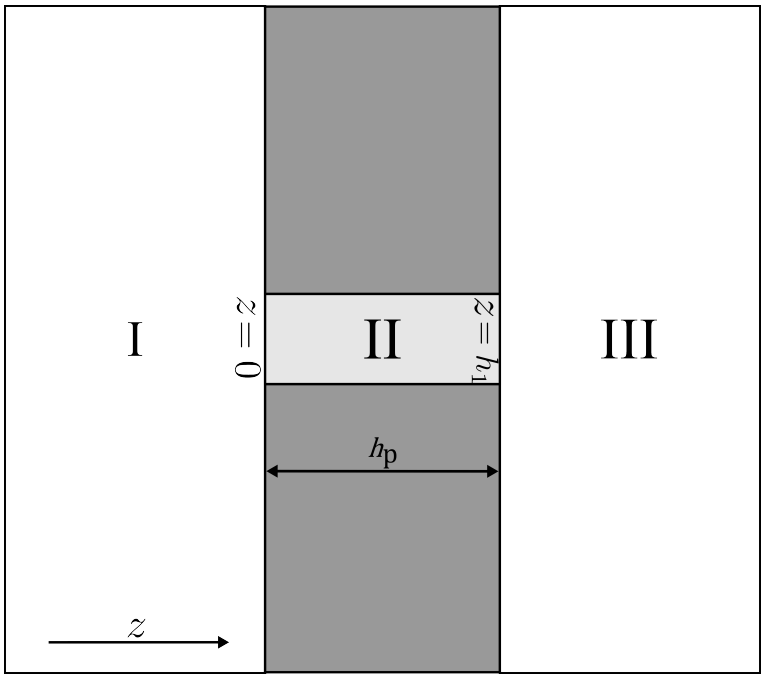

Figure A.1: Schematic side view of the SF structure showing the different regions used in formulating the modal matching calculation of the structure's transmittance.

mitted wave is described by a Fourier-Floquet expansion:

$$p_{\mathrm{III}} = T\left[m_1, m_2\right] \exp\left[i\left(\left(k_x + \frac{2\pi m_1}{d}\right)x + \left(k_y + \frac{2\pi m_2}{d}\right)y - k_z\left[m1, m2\right]z\right)\right]. \tag{A.3}$$

Expressions describing the velocity component of the wave are also required. Equation (2.10) allows expressions for the velocity to be determined directly from the pressure function.

From equation (2.10) the expression for the velocity of the incident wave in the z-axis is

$$\begin{aligned} u_{\mathrm{I}} = {} & i\frac{k_z}{\rho_0}\exp\left[i\left(k_z z + k_x x + k_y y\right)\right] \\ & - i\frac{k_z}{\rho_0}R\left[m_1, m_2\right]\exp\left[i\left(\left(k_x + \frac{2\pi m_1}{d}\right)x + \left(k_y + \frac{2\pi m_2}{d}\right)y - k_z\left[m1, m2\right]z\right)\right], \end{aligned} \tag{A.4}$$

the expression for the velocity within the pipe is

$$u_{\mathrm{II}} = i\frac{k_0'}{\rho_0'}\left(A_1\exp\left[ik_0'z\right] - A_2\exp\left[-ik_0'z\right]\right), \tag{A.5}$$

and the expression for the velocity of the transmitted wave is

$$u_{\mathrm{III}} = -i\frac{k_z}{\rho_0} T\left[m_1, m_2\right] \exp\left[i\left(\left(k_x + \frac{2\pi m_1}{d}\right)x + \left(k_y + \frac{2\pi m_2}{d}\right)y - k_z\left[m1, m2\right]z\right)\right]. \tag{A.6}$$

The required boundary conditions that allow solution of the problem are easily determined. Consider a planar surface of particles all incident normal to the structure. All the particles are travelling at the same speed and arrive at the object at the same instant, therefore the velocity across the interface must be continuous. However, the particles that impact on the rigid body will exert a different pressure than the particles incident on the hole. Thus the pressure function is only continuous across the hole. From this simple picture the boundary conditions are:

1. The function describing the acoustic pressure is continuous over the hole.

2. The function describing the particle velocity is continuous over the whole of the unit cell.

Using these two conditions, continuity equations can be set up at each interface. Taking the first boundary condition for the pressure function:

$z = 0$

$$\int_0^a \int_0^a \exp\left[i\left(k_x x + k_y y\right)\right] dxdy + R\left[m_1, m_2\right] \int_0^a \int_0^a \exp\left[i\left(\left(k_x + \frac{2\pi m_1}{d}\right)x + \left(k_y + \frac{2\pi m_2}{d}\right)y\right)\right] dxdy = \left(A_1 + A_2\right) \int_0^a \int_0^a dxdy. \tag{A.7a}$$

$z = h_1$

$$T\left[m_1, m_2\right] \int_0^a \int_0^a \exp\left[i\left(\left(k_x + \frac{2\pi m_1}{d}\right)x + \left(k_y + \frac{2\pi m_2}{d}\right)y\right)\right] dxdy = \left(A_1 \exp\left[ik_0' h_1\right] + A_2 \exp\left[-ik_0' h_1\right]\right) \int_0^a \int_0^a dxdy. \tag{A.7b}$$

Taking the second boundary condition for the function describing the particle velocity and multiplying both sides of the equality by $\exp\left[-i\left(k_x + \frac{2\pi m_1}{d}\right)x - i\left(k_y + \frac{2\pi m_2}{d}\right)y\right]$ the equations obtained are:

$z = 0$

$$\frac{k_z\left[0,0\right]\delta\left[m_1,m_2\right]}{\rho_0}\int_0^d\int_0^d dxdy - k_z\left[m_1,m_2\right]R\left[m_1,m_2\right]\int_0^d\int_0^d dxdy$$
$$= \frac{k_0'\left(A_1-A_2\right)}{\rho_0'}\int_0^a\int_0^a \exp\left[-i\left(k_x+\frac{2\pi m_1}{d}\right)x - i\left(k_y+\frac{2\pi m_2}{d}\right)y\right]dxdy. \quad \text{(A.7c)}$$

$z = h_1$

$$\frac{T\left[m_1,m_2\right]k_z\left[m_1,m_2\right]d^2}{\rho_0}$$
$$= \frac{k_0'\left(A_1\exp\left[ik_0'h_1\right] - A_2\exp\left[-ik_0'h_1\right]\right)}{\rho_0'}\times$$
$$\int_0^a\int_0^a \exp\left[-i\left(k_x+\frac{2\pi m_1}{d}\right)x - i\left(k_y+\frac{2\pi m_2}{d}\right)y\right]dxdy. \quad \text{(A.7d)}$$

To simplify the equations the expression $Q_\pm$ is defined:

$$Q_\pm = \int_0^a\int_0^a \exp[\pm i(k_x+\frac{2\pi m_1}{d})x \pm i(k_y+\frac{2\pi m_2}{d})y]dxdy. \quad \text{(A.8)}$$

Substituting $Q_\pm$ and calculating the remaining integrals leaves the following simplified continuity equations: Continuity of pressure:

$$Q_+\left[0,0\right] + \sum R\left[m_1,m_2\right]Q_+\left[m_1,m_2\right] = a^2\left(A_1+A_2\right) \quad \text{(A.9a)}$$
$$a^2\left(A_1\exp\left[ik_0'h_1\right] + A_2\exp\left[-ik_0'h_1\right]\right) = \sum T\left[m_1,m_2\right]Q_+\left[m_1,m_2\right]. \quad \text{(A.9b)}$$
$$\text{(A.9c)}$$

Continuity of particle velocity:

$$\frac{d^2k_z\left[0,0\right]\delta\left[m_1,m_2\right] - d^2k_z\left[m_1,m_2\right]R\left[m_1,m_2\right]}{\rho_0} = \frac{k_0'\left(A_1-A_2\right)Q_-\left[m_1,m_2\right]}{\rho_0'}, \quad \text{(A.9d)}$$
$$\frac{k_0'\left(A_1\exp\left[ik_0'h_1\right] + A_2\exp\left[-ik_0'h_1\right]\right)Q_-\left[m_1,m_2\right]}{\rho_0'} = \frac{d^2k_z\left[m_1,m_2\right]T\left[m_1,m_2\right]}{\rho_0}. \quad \text{(A.9e)}$$

Rearranging and eliminating variables to find $T\left[m_1,m_2\right]$ is a relatively straightforward task from here. First we rearrange equation A.9d as follows:

$$R\left[m_1,m_2\right] = \delta\left[m_1,m_2\right] - \left(A_1-A_2\right)\frac{\rho_0k_0'Q_-\left[m_1,m_2\right]}{\rho_0'k_z\left[m_1,m_2\right]d^2}, \quad \text{(A.10)}$$

and substitute into equation A.9a:

$$2Q_{+}\left[0,0\right]-\left(A_{1}-A_{2}\right)\sum\frac{\rho_{0}k_{0}^{\prime}Q_{+}\left[m_{1},m_{2}\right]Q_{-}\left[m_{1},m_{2}\right]}{\rho_{0}^{\prime}k_{z}\left[m_{1},m_{2}\right]}. \tag{A.11}$$

At this stage the expression S_1 is defined to further simplify the equations:

$$S_{\mathrm{I}}=\sum\frac{k_{0}^{\prime}Q_{+}\left[m_{1},m_{2}\right]Q_{-}\left[m_{1},m_{2}\right]}{k_{z}\left[m_{1},m_{2}\right]d^{2}}, \tag{A.12}$$

leaving

$$2Q_{+}[0,0]-\frac{\rho_{0}\left(A_{1}-A_{2}\right)S_{\mathrm{I}}}{\rho_{0}^{\prime}}=a^{2}\left(A_{1}+A_{2}\right). \tag{A.13}$$

Equation A.9e is rearranged for $T[m_1, m_2]$

$$T\left[m_{1},m_{2}\right]=\left(A_{1}\exp\left[ik_{0}^{\prime}h_{1}\right]-A_{2}\exp\left[-ik_{0}h_{1}\right]\right)\frac{\rho_{0}k_{0}^{\prime}Q_{-}\left[m_{1},m_{2}\right]}{\rho_{0}^{\prime}k_{z}\left[m_{1},m_{2}\right]d^{2}}, \tag{A.14}$$

and substituted into equation A.9b

$$\frac{\rho_{0}\left(A_{1}\exp\left[ik_{0}^{\prime}h_{1}\right]-A_{2}\exp\left[-ik_{0}^{\prime}h_{1}\right]\right)S_{1}}{\rho_{0}^{\prime}}=a^{2}\left(A_{1}\exp\left[ik_{0}^{\prime}h_{1}\right]+A_{2}\exp\left[-ik_{0}^{\prime}h_{1}\right]\right). \tag{A.15}$$

Using equations A.13 and A.15 we can eliminate A_1 and A_2 to obtain a final expression for the transmission $T[m_1, m_2]$.

$$\begin{aligned}T[m_{1},m_{2}]\\ =-\frac{4a^{2}\exp\left[ik_{0}h_{1}\right]\rho_{0}\rho_{0}^{\prime}Q_{-}\left[m_{1},m_{2}\right]Q_{+}\left[0,0\right]}{d^{2}((-1+\exp[2ik_{0}h_{1}])\,S_{1}^{2}\rho_{0}^{2}-2a^{2}\left(1+\exp[2ik_{0}^{\prime}h_{1}]\right)S_{1}\rho_{0}\rho_{0}^{\prime}\\ +a^{4}\left(-1+\exp[2ik_{0}^{\prime}h_{1}]\rho_{0}^{\prime2}\right)k_{z}\left[m_{1},m_{2}\right])}.\end{aligned} \tag{A.16}$$

Appendix B

Double Fishnet Modal Matching Code

Here a full derivation is provided of the modal matching method used to simulate the transmittance of the DF structure. As with the previous derivation for a single plate detailed in 3.3 the structure is split into different regions; the incident region, the hole in the first plate, the region between the plates, the hole in the second plate and the transmission region (see figure B.1). The plates are assumed to be perfectly rigid and the sub wavelength size allows the wave inside the plate to be represented by a plane wave.

Ignoring the time dependence, which will divide out, a plane wave defined by its pressure field is incident upon the SF with wavevectors k_x, k_y and k_z in the x, y and z axes. The waves in the holes are represented by a simple plane wave. The reflected, gap and transmitted waves are defined in terms of a Fourier-Floquet expansion.

Region I:

$$p_{\mathrm{I}} = \exp\left[i\left(k_x x + k_y y + k_z z\right)\right] + R\left[m_1, m_2\right] \times \exp\left[i\left(\left(k_x + \frac{2\pi m_1}{d}\right)x + \left(k_y + \frac{2\pi m_2}{d}\right)y - k_z\left[m_1, m_2\right]z\right)\right]. \quad \text{(B.1)}$$

Region II:

$$p_{\mathrm{II}} = A_1 \exp[ik_0 z] + A_2 \exp[-ik_0 z]. \quad \text{(B.2)}$$

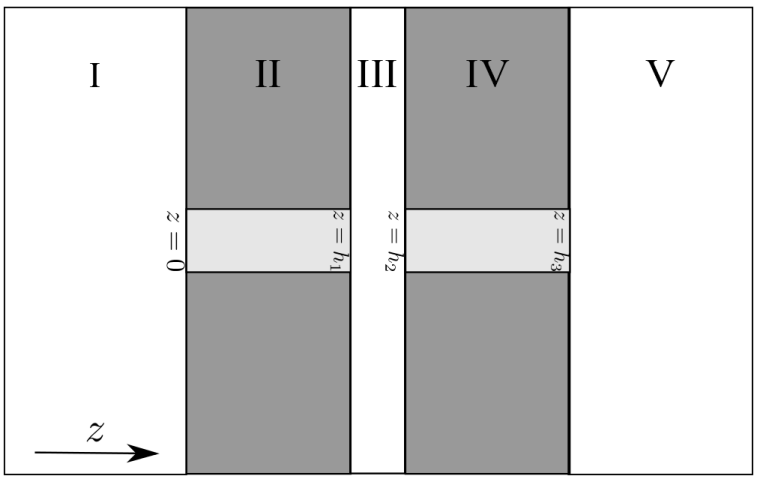

Figure B.1: Schematic side view of the DF structure showing the different regions used in formulating the modal matching calculation of the transmittance.

Region III:

$$p_{\mathrm{III}} = B_1\left[m_1, m_2\right] \exp\left[i\left(\left(k_x + \frac{2\pi m_1}{d}\right)x + \left(k_y + \frac{2\pi m_2}{d}\right)y - k_z\left[m_1, m_2\right](z - h_1)\right)\right] + B_2\left[m_1, m_2\right] \exp\left[i\left(\left(k_x + \frac{2\pi m_1}{d}\right)x + \left(k_y + \frac{2\pi m_2}{d}\right)y - k_z\left[m_1, m_2\right](z - h_1)\right)\right]. \tag{B.3}$$

Region IV:

$$p_{\mathrm{IV}} = C_1 \exp[i(k_0(z - h_1 - h_2))] + C_2 \exp[-i(k_0(z - h_1 - h_2))]. \tag{B.4}$$

Region V:

$$p_{\mathrm{V}} = T\left[m_1, m_2\right] \times \exp\left[i\left(\left(k_x + \frac{2\pi m_1}{d}\right)x + \left(k_y + \frac{2\pi m_2}{d}\right)y - k_z\left[m_1, m_2\right](z - h_1 - h_2 - h_3)\right)\right]. \tag{B.5}$$

Euler's equation [equation (2.10)] can be used to determine the particle velocity in the z axis. As the medium is the same throughout the DF the density will cancel out and as such is ignored in the following expressions.

Region I:

$$u_{\mathrm{I}} = ik_z\left[m_1, m_2\right]\exp\left[i\left(k_x x + k_y y + k_z\left[m_1, m_2\right] z\right)\right] - ik_z\left[m_1, m_2\right] R\left[m_1, m_2\right] \times \exp\left[i\left(\left(k_x + \frac{2\pi m_1}{d}\right)x + \left(k_y + \frac{2\pi m_2}{d}\right)y - k_z\left[m_1, m_2\right] z\right)\right]. \quad \text{(B.6)}$$

Region II:

$$u_{\mathrm{II}} = ik_z\left[0,0\right]\left(A_1\exp\left[ik_0 z\right] - A_2\exp\left[-ik_0 z\right]\right). \quad \text{(B.7)}$$

Region III:

$$u_{\mathrm{III}} = ik_z\left[m_1, m_2\right] B_1\left[m_1, m_2\right] \times \exp\left[i\left(\left(k_x + \frac{2\pi m_1}{d}\right)x + \left(k_y + \frac{2\pi m_2}{d}\right)y + k_z\left[m_1, m_2\right]\left(z - h_1\right)\right)\right] - ik_z\left[m_1, m_2\right] B_2\left[m_1, m_2\right] \times \exp\left[i\left(\left(k_x + \frac{2\pi m_1}{d}\right)x + \left(k_y + \frac{2\pi m_2}{d}\right)y - k_z\left[m_1, m_2\right]\left(z - h_1\right)\right)\right]. \quad \text{(B.8)}$$

Region IV:

$$u_{\mathrm{IV}} = ik_z[0,0](C_1\exp[ik_z[0,0](z - h_1 - h_2)] - C_2\exp[-ik_z[0,0](z - h_1 - h_2)]). \quad \text{(B.9)}$$

Region V:

$$u_{\mathrm{V}} = ik_z\left[m_1, m_2\right] T_1\left[m_1, m_2\right] \times \exp\left[i\left(\left(k_x + \frac{2\pi m_1}{d}\right)x + \left(k_y + \frac{2\pi m_2}{d}\right)y - k_z\left[m_1, m_2\right]\left(z - h_1 - h_2 - h_3\right)\right)\right]. \quad \text{(B.10)}$$

Boundary conditions are applied at each of the interfaces $z = 0, h_1, h_2$ and h_3:

1. The function describing the acoustic pressure is continuous only over the hole.

2. The function describing the particle velocity is continuous over the whole of the unit cell.

Boundary condition 1:

$z = 0$

$$\int_0^a \int_0^a \exp\left[i\left(k_x x + k_y y\right)\right] dxdy + R\left[m_1, m_2\right] \int_0^a \int_0^a \exp\left[i\left(\left(k_x + \frac{2\pi m_1}{d}\right) x + \left(k_y + \frac{2\pi m_2}{d}\right) y\right)\right] dxdy = \left(A_1 + A_2\right) \int_0^a \int_0^a dxdy. \quad \text{(B.11)}$$

$z = h_1$

$$B_1\left[m_1, m_2\right] \int_0^a \int_0^a \exp\left[i\left(\left(k_x + \frac{2\pi m_1}{d}\right) x + \left(k_y + \frac{2\pi m_2}{d}\right) y\right)\right] dxdy + B_2\left[m_1, m_2\right] \int_0^a \int_0^a \exp\left[i\left(\left(k_x + \frac{2\pi m_1}{d}\right) x + \left(k_y + \frac{2\pi m_2}{d}\right) y\right)\right] dxdy = \left(A_1 \exp\left[ik_0 h_1\right] + A_2 \exp\left[-ik_0 h_1\right]\right) \int_0^a \int_0^a dxdy. \quad \text{(B.12)}$$

$z = h_1 + h_2$

$$B_1\left[m_1, m_2\right] \exp\left[ik_z\left[m_1, m_2\right] h_2\right] \times \int_g^{g+a} \int_h^{h+a} \exp\left[i\left(\left(k_x + \frac{2\pi m_1}{d}\right) x + \left(k_y + \frac{2\pi m_2}{d}\right) y\right)\right] dxdy + B_2\left[m_1, m_2\right] \exp\left[-ik_z\left[m_1, m_2\right] h_2\right] \times \int_g^{g+a} \int_g^{g+a} \exp\left[i\left(\left(k_x + \frac{2\pi m_1}{d}\right) x + \left(k_y + \frac{2\pi m_2}{d}\right) y\right)\right] dxdy = \left(C_1 + C_2\right) \int_0^a \int_0^a dxdy. \quad \text{(B.13)}$$

$z = h_1 + h_2 + h_3$

$$T\left[m_1, m_2\right] \int_g^{g+a} \int_h^{h+a} \exp\left[i\left(\left(k_x + \frac{2\pi m_1}{d}\right) x + \left(k_y + \frac{2\pi m_2}{d}\right) y\right)\right] = \left(C_1 \exp\left[ik_0 h_3\right] + C_2 \exp\left[-ik_0 h_3\right]\right) \int_g^{g+a} \int_h^{h+a} dxdy. \quad \text{(B.14)}$$

Taking the second boundary condition for the function describing the particle velocity and multiplying both sides of the equality by $\exp\left[-i\left(k_x + \frac{2\pi m_1}{d}\right) x - i\left(k_y + \frac{2\pi m_2}{d}\right) y\right]$ the equations obtained are:

$z = 0$

$$k_z[0,0]\int_0^d\int_0^d dxdy - k_z[m_1,m_2]R[m_1,m_2]\int_0^d\int_0^d dxdy$$
$$= k_0(A_1 - A_2)\int_0^a\int_0^a \exp\left[-i\left(\left(k_x + \frac{2\pi m_1}{d}\right)x - \left(k_y + \frac{2\pi m_2}{d}\right)y\right)\right]dxdy. \quad \text{(B.15)}$$

$z = h_1$

$$k_z[0,0](B_1[m_1,m_2] - B_2[m_1,m_2])\int_0^d\int_0^d dxdy$$
$$= k_0(A_1\exp[ik_0h_1] - A_2\exp[-ik_0h_1])\times$$
$$\int_0^a\int_0^a \exp\left[-i\left(\left(k_x + \frac{2\pi m_1}{d}\right)x - i\left(k_y + \frac{2\pi m_2}{d}\right)y\right)\right]dxdy. \quad \text{(B.16)}$$

$z = h_1 + h_2$

$$k_z[m_1,m_2](B_1[m_1,m_2]\exp[ik_z[m_1,m_2]h_2] - B_2[m_1,m_2]\exp[-ik_z[m_1,m_2]h_2])\times$$
$$\int_0^d\int_0^d dxdy$$
$$= k_0(C_1 - C_2)\int_g^{g+a}\int_h^{h+a} \exp\left[-i\left(\left(k_x + \frac{2\pi m_1}{d}\right)x - i\left(k_y + \frac{2\pi m_2}{d}\right)y\right)\right]dxdy. \quad \text{(B.17)}$$

$z = h_1 + h_2 + h_3$

$$k_z[m_1,m_2]T[m_1,m_2]\int_0^d\int_0^d dxdy =$$
$$k_0(C_1\exp[ik_0h_3] - C_2\exp[-ik_0h_3])\times$$
$$\int_g^{g+a}\int_h^{h+a} \exp\left[-i\left(\left(k_x + \frac{2\pi m_1}{d}\right)x - i\left(k_y + \frac{2\pi m_2}{d}\right)y\right)\right]dxdy. \quad \text{(B.18)}$$

To simplify the equations the expressions $Q_\pm[m_1,m_2]$ and $Q'_\pm[m_1,m_2]$ are defined:

$$Q_\pm[m_1,m_2] = \int_0^a\int_0^a \exp\left[\pm i\left(\left(k_x + \frac{2\pi m_1}{d}\right)x + \left(k_y + \frac{2\pi m_2}{d}\right)y\right)\right]dxdy,$$

$$Q'_\pm[m_1,m_2] = \int_g^{g+a}\int_h^{h+a} \exp\left[\pm i\left(\left(k_x + \frac{2\pi m_1}{d}\right)x + \left(k_y + \frac{2\pi m_2}{d}\right)y\right)\right]dxdy.$$

Substituting $Q_\pm$ and calculating the remaining integrals leaves the following simplified

continuity equations: Continuity of pressure:

$$Q_+[0,0] + \sum R[m_1,m_2]Q_+[m_1,m_2] = a^2(A_1 + A_2), \tag{B.19a}$$

$$\sum (B_1[m_1,m_2] + B_2[m_1,m_2])Q_+[m_1,m_2] = a^2(A_1 \exp[ik_0h_1] + A_2 \exp[-ik_0h_1]), \tag{B.19b}$$

$$\sum (B_1[m_1,m_2] \exp[ik_z[m_1,m_2]h_2] + B_2[m_1,m_2] \exp[-ik_z[m_1,m_2]h_2])Q'_+[m_1,m_2] = a^2(C_1 + C_2), \tag{B.19c}$$

$$\sum T[m_1,m_2]Q'_+[m_1,m_2] = a^2(C_1 \exp[ik_0h_3] + C_2 \exp[-ik_0h_3]). \tag{B.19d}$$

Continuity of particle velocity:

$$k_z[0,0]d^2\delta[m_1,m_2] - k_z[m_1,m_2]d^2R[m_1,m_2] = k_0(A_1 - A_2)Q_-[m_1,m_2], \tag{B.19e}$$

$$k_z[m_1,m_2]d^2(B_1[m_1,m_2] - B_2[m_1,m_2]) = k_0(A_1 \exp[ik_0h_1] - A_2 \exp[-ik_0h_1])Q_-[m_1,m_2], \tag{B.19f}$$

$$k_z[m_1,m_2]d^2(B_1[m_1,m_2] \exp[ik_z[m_1,m_2]h_2] - B_2[m_1,m_2] \exp[-ik_z[m_1,m_2]h_2]) = k_0(C_1 - C_2)Q'_-[m_1,m_2], \tag{B.19g}$$

$$T[m_1,m_2]k_z[m_1,m_2]d^2 = k_0(C_1 \exp[ik_0h_3] - C_2 \exp[-ik_0h_3])Q'_-[m_1,m_2]. \tag{B.19h}$$

Equations (B.19f) and (B.19g) are combined to determine expressions for $B_1[m_1,m_2]+B_2[m_1,m_2]$ and $B_1[m_1,m_2] \exp[ik_z[m_1,m_2]h_2] - B_2[m_1,m_2] \exp[-ik_z[m_1,m_2]h_2]$.

$$\sum (B_1[m_1,m_2] + B_2[m_1,m_2]) = \sum ik_0 \cot[k_z[m_1,m_2]h_2] \frac{Q_-[m_1,m_2](A_1 \exp[ik_0h_1] - A_2 \exp[-ik_0h_1])}{d^2k_z[m_1,m_2]} - \sum ik_0 \csc[k_z[m_1,m_2]h_2] \frac{Q'_-[m_1,m_2](C_1 - C_2)}{d^2k_z[m_1,m_2]}, \tag{B.20a}$$

$$\sum (B_1[m_1,m_2] \exp[ik_z[m_1,m_2]] + B_2[m_1,m_2] \exp[-ik_z[m_1,m_2]]) = \sum ik_0 \csc[k_z[m_1,m_2]h_2] \frac{Q_-[m_1,m_2](A_1 \exp[ik_0h_1] - A_2 \exp[-ik_0h_1])}{d^2k_z[m_1,m_2]} - \sum ik_0 \cot[k_z[m_1,m_2]h_2] \frac{Q'_-[m_1,m_2](C_1 - C_2)}{d^2k_z[m_1,m_2]}. \tag{B.20b}$$

Equations (B.19e) and (B.19h) are rearranged in terms of $R[m_1, m_2]$ and $T[m_1, m_2]$:

$$R[m_1, m_2] = \delta[m_1, m_2] - (A_1 - A_2) \sum \frac{k_0 Q_-[m_1, m_2]}{k_z[m_1, m_2] d^2}, \tag{B.20c}$$

$$T[m_1, m_2] = (C_1 \exp[ik_0 h_3] - C_2 \exp[-ik_0 h_3]) \sum \frac{k_0 Q'_-[m_1, m_2]}{k_z[m_1, m_2] d^2}). \tag{B.20d}$$

Substituting equation (B.20c) into equation (B.19a), equation (B.20a) into equation (B.19b), equation (B.20b) into equation (B.19c), and equation (B.20d) into equation (B.19d) gives:

$$2Q_+[0, 0] - (A_1 - A_2) \sum \frac{k_0 Q_+[m_1, m_2] Q_-[m_1, m_2]}{k_z[m_1, m_2] d^2} = a^2 (A_1 + A_2), \tag{B.21a}$$

$$\begin{aligned}(A_1 \exp[ik_0 h_1] - A_2 \exp[-ik_0 h_1]) \sum ik_0 \cot[k_z[m_1, m_2] h_2] \frac{Q_+[m_1, m_2] Q'_+[m_1, m_2]}{k_z[m_1, m_2] d^2} \\ - (C_1 - C_2) \sum ik_0 \csc[k_z[m_1, m_2] h_2] \frac{Q_+[m_1, m_2] Q'_-[m_1, m_2]}{k_z[m_1, m_2] d^2} \\ = a^2 (A_1 \exp[ik_0 h_1] + A_2 \exp[-ik_0 h_1]),\end{aligned} \tag{B.21b}$$

$$\begin{aligned}(A_1 \exp[ik_0 h_1] - A_2 \exp[-ik_0 h_1]) \sum ik_0 \csc[k_z[m_1, m_2] h_2] \frac{Q_-[m_1, m_2] Q'_+[m_1, m_2]}{k_z[m_1, m_2] d^2} \\ - (C_1 - C_2) \sum ik_0 \cot[k_z[m_1, m_2] h_2] \frac{Q_-[m_1, m_2] Q'_-[m_1, m_2]}{k_z[m_1, m_2] d^2} \\ = a^2 (C_1 + C_2),\end{aligned} \tag{B.21c}$$

$$\begin{aligned}(C_1 \exp[ik_0 h_3] - C_2 \exp[-ik_0 h_3]) \sum \frac{k_0 Q_-[m_1, m_2] Q'_-[m_1, m_2]}{k_z[m_1, m_2] d^2} \\ = a^2 (C_1 \exp[ik_0 h_3] + C_2 \exp[-ik_0 h_3]).\end{aligned} \tag{B.21d}$$

Further simplifications are made by defining the expressions S_{1-6}:

$$S_1 = \sum \frac{k_0 Q_+[m_1,m_2]Q'_+[m_1,m_2]}{k_z[m_1,m_2]d^2}, \tag{B.22a}$$

$$S_2 = \sum ik_0 \cot[k_z[m_1,m_2]h_2]\frac{Q_+[m_1,m_2]Q'_+[m_1,m_2]}{k_z[m_1,m_2]d^2}, \tag{B.22b}$$

$$S_3 = \sum ik_0 \csc[k_z[m_1,m_2]h_2]\frac{Q_+[m_1,m_2]Q'_-[m_1,m_2]}{k_z[m_1,m_2]d^2}, \tag{B.22c}$$

$$S_4 = \sum ik_0 \csc[k_z[m_1,m_2]h_2]\frac{Q_-[m_1,m_2]Q'_+[m_1,m_2]}{k_z[m_1,m_2]d^2}, \tag{B.22d}$$

$$S_5 = \sum ik_0 \cot[k_z[m_1,m_2]h_2]\frac{Q_-[m_1,m_2]Q'_-[m_1,m_2]}{k_z[m_1,m_2]d^2}, \tag{B.22e}$$

$$S_6 = \sum \frac{k_0 Q_-[m_1,m_2]Q'_-[m_1,m_2]}{k_z[m_1,m_2]d^2}. \tag{B.22f}$$

Using these, we can simplify equations (B.21) to:

$$2Q_+[m_1,m_2] - (A_1 - A_2)S_1 = a^2(A_1 + A_2), \tag{B.23a}$$

$$(A_1 \exp[ik_0h_1] - A_2 \exp[-ik_0h_1])S_2 - (C_1 - C_2)S_3 = a^2(A_1 \exp[ik_0h_1] + A_2 \exp[-ik_0h_1]), \tag{B.23b}$$

$$(A_1 \exp[ik_0h_1] - A_2 \exp[-ik_0h_1])S_4 - (C_1 - C_2)S_5 = a^2(C_1 + C_2), \tag{B.23c}$$

$$(C_1 \exp[ik_0h_3] - C_2 \exp[-ik_0h_3])S_6 = a^2(C_1 \exp[ik_0h_3] + C_2 \exp[-ik_0h_3]). \tag{B.23d}$$

Combining equations (B.23) the expression below is obtained:

$$\begin{aligned}
&\Big(C_1 \exp[ik_0h_3] - C_2 \exp[-ik_0h_3]\Big) \\
&= \frac{-2a^4 S_4 Q_1[0,0]}{a^2 \cos[k_0h_1]\Big(a^2\Big(S_3S_4 - (S_1+S_2)(S_5+S_6) + S_1(-S_3S_4 + S_2(S_5S_6))\Big)\cos[k_0h_3] \\
&\qquad + \Big(a^8 + S_1(-S_3S_4 + S_2S_5)S_6 + a^4(S_1S_2 + S_5S_6)\Big)\sin[k_0h_3]\Big)}.
\end{aligned} \tag{B.24}$$

Equation (B.24) is substituted into equation (B.20d) to obtain the final expression for the transmission through the ADF structure as a function of all the parameters.

$$T[m_1,m_2] = \frac{-2a^4 S_4 Q_+[0,0]}{D}\frac{k_0 Q'_-[m_1,m_2]}{k_z[m_1,m_2]d^2}, \tag{B.25}$$

where

$$
\begin{aligned}
D = a^2 \cos[k_0 h_1] \Big(& a^2 \Big(S_3 S_4 - (S_1 + S_2)(S_5 + S_6) \Big) \cos[k_0 h_3] \\
& + i \Big(- S_3 S_4 S_6 + (S_1 + S_2)(a^4 + S_5 S_6) \Big) \sin[k_0 h_3] \Big) \\
+ \sin[k_0 h_1] \Big(& i a^2 \Big(a^4 (S_5 + S_6) + S_1 (-S_3 S_4 + S_2 (S_5 + S_6)) \Big) \cos[k_0 h_3] \\
& + \Big(a^8 + S_1 (-S_3 S_4 + S_2 S_5) S_6 + a^4 (S_1 S_2 + S_5 S_6) \Big) \sin[k_0 h_3] \Big).
\end{aligned}
$$

References

[1] Holland, C.W. Geoacoustic inversion for fine-grained sediments. *The Journal of the Acoustical Society of America*, **111**, 1560 (2002). xi, 85, 86

[2] Aközbek, N., Mattiucci, N., de Ceglia, D., Trimm, R., Alù, A., DAguanno, G., Vincenti, M.A., Scalora, M., and Bloemer, M.J. Experimental demonstration of plasmonic Brewster angle extraordinary transmission through extreme subwavelength slit arrays in the microwave. *Physical Review B*, **85**, 205430 (2012). xi, 87

[3] Ovid. *Metamorphoses*. Oxford University Press Inc., New York (1998). 1

[4] Declercq, N.F. and Dekeyser, C.S.A. Acoustic diffraction effects at the Hellenistic amphitheater of Epidaurus: Seat rows responsible for the marvelous acoustics. *The Journal of the Acoustical Society of America*, **121**, 2011 (2007). 1

[5] Declercq, N.F., Degrieck, J., Briers, R., and Leroy, O. A theoretical study of special acoustic effects caused by the staircase of the El Castillo pyramid at the Maya ruins of Chichen-Itza in Mexico. *The Journal of the Acoustical Society of America*, **116**, 3328 (2004). 1

[6] Cruz Calleja, J.A. and Declercq, N.F. The Acoustic Raindrop Effect at Mexican Pyramids: The Architects' Homage to the Rain God Chac? *Acta Acustica united with Acustica*, **95**, 849 (2009). 1

[7] Rayleigh, L. On Waves Propagated along the Plane Surface of an Elastic Solid. *Proceedings of the London Mathematical Society*, **s1-17**, 4 (1885). 2, 108

[8] Love, A.E.H. *Some Problems of Geodynamics*. Cambridge University Press, Cambridge (1911). 2, 108

[9] Lamb, H. On Waves in an Elastic Plate. *Proceedings of the Royal Society A: Mathematical, Physical and Engineering Sciences*, **93**, 114 (1917). 2, 108

[10] Stoneley, R. Elastic Waves at the Surface of Separation of Two Solids. *Proceedings of the Royal Society A: Mathematical, Physical and Engineering Sciences*, **106**, 416 (1924). 2, 108

[11] Scholte, J.G. The Range of Existence of Rayleigh and Stoneley Waves. *Geophysical Journal International*, **5**, 120 (1947). 2

[12] Haldorsen, J.B.U., Johnson, D.L., Plona, T., Sinha, B., Valero, H.P., and Winkler, K. Borehole Acoustic Waves. *Oilfield Review*, **Spring**, 34 (2006). 2

[13] Kelders, L., Allard, J., and Lauriks, W. Ultrasonic surface waves above rectangular-groove gratings. *The Journal of the Acoustical Society of America*, **103**, 2730 (1998). 2, 108

[14] Tizianel, J., Allard, J.F., and Brouard, B. Surface waves above honeycombs. *The Journal of the Acoustical Society of America*, **104**, 2525 (1998). 2

[15] Allard, J., Kelders, L., and Lauriks, W. Ultrasonic surface waves above a doubly periodic grating. *The Journal of the Acoustical Society of America*, **105**, 2528 (1999). 2

[16] Torrent, D. and Sánchez-Dehesa, J. Acoustic Analogue of Graphene: Observation of Dirac Cones in Acoustic Surface Waves. *Physical Review Letters*, **108**, 174301 (2012). 2, 108

[17] Pendry, J.B., Martín-Moreno, L., and Garcia-Vidal, F.J. Mimicking Surface Plasmons with Structured Surfaces. *Science*, **305**, 847 (2004). 2, 108

[18] Hibbins, A.P., Evans, B.R., and Sambles, J.R. Experimental verification of designer surface plasmons. *Science (New York, N.Y.)*, **308**, 670 (2005). 2, 107, 109

[19] Rance, H.J., Hooper, I.R., Hibbins, A.P., and Roy Sambles, J. Structurally dictated anisotropic designer surface plasmons. *Applied Physics Letters*, **99**, 181107 (2011). 2, 109

[20] Luneburg, R.K. *Mathematical Theory of Optics*. Brown University, Providence, Rhode Island (1944). 3

[21] Dockrey, J.A., Lockyear, M.J., Berry, S.J., Horsley, S.A.R., Sambles, J.R., and Hibbins, A.P. Thin metamaterial Luneburg lens for surface waves. *Physical Review B*, **87**, 125137 (2013). 3

[22] Brun, M., Guenneau, S., and Movchan, a.B. Achieving control of in-plane elastic waves. *Applied Physics Letters*, **94**, 061903 (2009). 3

[23] Stenger, N., Wilhelm, M., and Wegener, M. Experiments on Elastic Cloaking in Thin Plates. *Physical Review Letters*, **108**, 014301 (2012). 3

[24] Mei, J., Hou, B., Ke, M., Peng, S., Jia, H., Liu, Z., Shi, J., Wen, W., and Sheng, P. Acoustic wave transmission through a bulls eye structure. *Applied Physics Letters*, **92**, 124106 (2008). 3

[25] Zhou, Y., Lu, M.H., Feng, L., Ni, X., Chen, Y.F., Zhu, Y.Y., Zhu, S.N., and Ming, N.B. Acoustic Surface Evanescent Wave and its Dominant Contribution to Extraordinary Acoustic Transmission and Collimation of Sound. *Physical Review Letters*, **104**, 1 (2010). 3, 108

[26] Ebbesen, T.W., Lezec, H.J., Ghaemi, H.F., Thio, T., and Wolff, P.A. Extraordinary optical transmission through sub-wavelength hole arrays. *Nature*, **391**, 667 (1998). 3, 96

[27] Martin-Moreno, L., Garcia-Vidal, F.J., Lezec, H.J., Pellerin, K.M., Thio, T., Pendry, J.B., and Ebbesen, T.W. Theory of extraordinary optical transmission through subwavelength hole arrays. *Nature*, **86**, 4 (2000). 3

[28] Bethe, H. Theory of Diffraction by Small Holes. *Physical Review*, **66**, 163 (1944). 3

[29] Lu, M.H., Liu, X.K., Feng, L., Li, J., Huang, C.P., Chen, Y.F., Zhu, Y.Y., Zhu, S.N., and Ming, N.B. Extraordinary Acoustic Transmission through a 1D Grating with Very Narrow Apertures. *Physical Review Letters*, **99**, 1 (2007). 3

[30] Zhou, L. and Kriegsmann, G.a. Complete transmission through a periodically perforated rigid slab. *The Journal of the Acoustical Society of America*, **121**, 3288 (2007).

[31] Estrada, H., García de Abajo, F., Candelas, P., Uris, A., Belmar, F., and Meseguer, F. Angle-Dependent Ultrasonic Transmission through Plates with Subwavelength Hole Arrays. *Physical Review Letters*, **102**, 3 (2009).

[32] Estrada, H., Candelas, P., Uris, A., Belmar, F., Meseguer, F., and García de Abajo, F.J. Sound transmission through perforated plates with subwavelength hole arrays: A rigid-solid model. *Wave Motion*, **48**, 235 (2011). 3

[33] Christensen, J., Martin-Moreno, L., and Garcia-Vidal, F. Theory of Resonant Acoustic Transmission through Subwavelength Apertures. *Physical Review Letters*, **101**, 2 (2008). 3, 22

[34] Estrada, H., Candelas, P., Uris, A., Belmar, F., García de Abajo, F., and Meseguer, F. Extraordinary Sound Screening in Perforated Plates. *Physical Review Letters*, **101**, 2 (2008). 3

[35] Liu, Z. and Jin, G. Acoustic transmission resonance and suppression through double-layer subwavelength hole arrays. *Journal of physics. Condensed matter : an Institute of Physics journal*, **22**, 305003 (2010). 3, 120

[36] Christensen, J., Martin-Moreno, L., and Garcia-Vidal, F.J. All-angle blockage of sound by an acoustic double-fishnet metamaterial. *Applied Physics Letters*, **97**, 134106 (2010). 3, 42, 53, 59, 120

[37] Bell, J.S., Summers, I.R., Murray, A.R.J., Hendry, E., Sambles, J.R., and Hibbins, A.P. Low acoustic transmittance through a holey structure. *Physical Review B*, **85**, 214305 (2012). 3

[38] Zhu, J., Christensen, J., Jung, J., Martin-Moreno, L., Yin, X., Fok, L., Zhang, X., and Garcia-Vidal, F.J. A holey-structured metamaterial for acoustic deep-subwavelength imaging. *Nature Physics*, **7**, 52 (2010). 3

[39] Popa, B.I., Zigoneanu, L., and Cummer, S. Experimental Acoustic Ground Cloak in Air. *Physical Review Letters*, **106**, 1 (2011). 3

[40] Zigoneanu, L., Popa, B.I., and Cummer, S.A. Three-dimensional broadband omnidirectional acoustic ground cloak. *Nature Materials* (2014). 3

[41] Kinsler, L.E., Frey, A.R., Coppens, A.B., and V., S.J. *Fundamentals of Acoustics*. John Wiley and Sons, fourth edition (2000). ISBN 04718478895. 3, 8, 9, 12, 15, 16, 79

[42] Alù, A., DAguanno, G., Mattiucci, N., and Bloemer, M.J. Plasmonic Brewster Angle: Broadband Extraordinary Transmission through Optical Gratings. *Physical Review Letters*, **106**, 123902 (2011). 4, 87

[43] Le, K.Q., Argyropoulos, C., Mattiucci, N., D'Aguanno, G., Bloemer, M.J., and Alu, A. Broadband Brewster transmission through 2D metallic gratings. *Journal of Applied Physics*, **112**, 094317 (2012). 87

[44] D'Aguanno, G., Le, K.Q., Trimm, R., Alù, A., Mattiucci, N., Mathias, A.D., Aközbek, N., and Bloemer, M.J. Broadband metamaterial for nonresonant matching of acoustic waves. *Scientific reports*, **2**, 340 (2012). 87, 89

[45] Qiu, C., Hao, R., Li, F., Xu, S., and Liu, Z. Broadband transmission enhancement of acoustic waves through a hybrid grating. *Applied Physics Letters*, **100**, 191908 (2012). 4, 90, 121

[46] Climente, A., Torrent, D., and Sanchez-Dehesa, J. Omnidirectional broadband acoustic absorber based on metamaterials. *Applied Physics Letters*, **100**, 144103 (2012). 4

[47] Umnova, O., Elliott, A., and Venegas, R. Omnidirectional acoustic absorber with a porous coreTheory and measurements. *The Journal of the Acoustical Society of America*, **133**, 3290 (2013). 4

[48] Liang, Z. and Li, J. Extreme Acoustic Metamaterial by Coiling Up Space. *Physical Review Letters*, **108**, 114301 (2012). 4

[49] Kock, W.E. and Harvey, F.K. Refracting Sound Waves. *The Journal of the Acoustical Society of America*, **21**, 471 (1949). 4

[50] Xie, Y., Popa, B.I., Zigoneanu, L., and Cummer, S.A. Measurement of a Broadband Negative Index with Space-Coiling Acoustic Metamaterials. *Physical Review Letters*, **110**, 175501 (2013). 4

[51] Euler, M. Principes Generaux Du Movement Des Fluides. *Memoires de l'academie des sciences de Berlin*, **11**, 274 (1757). 11

[52] Euler, M. Principes generaux de l'etat d'equilibre des fluides. *Memoires de l'academie des sciences de Berlin*, **11**, 217 (1757). 11

[53] von Helmholtz, H. *On the Sensations of Tone as a Physiological Basis for the Theory of Music*. Longmans, Green, and Co., London, third edition (1885). 15

[54] Stokes, G.G. On the Theories of the Internal Friction of Fluids in Motion, and of the Equilibrium and Motion of Elastic Solids. *Transactions of the Cambridge Philosophical Society*, **8**, 287 (1845). 17

[55] Navier, C.L.M.H. Mémoire sur les lois du mouvement des fluids. *Mémoires de l'Académie des sciences de l'Institut de France*, **6**, 432 (1823). 17

[56] Tijdeman, H. On the propagation of sound waves in cylindrical tubes. *Journal of Sound and Vibration*, **39**, 1 (1975). 17

[57] Kirchhoff, G. Ueber den Einfluss der Wärmeleitung in einem Gase auf die Schallbewegung. *Annalen der Physik und Chemie*, **210**, 177 (1868). 17

[58] Rayleigh, J. *The Theory of Sound, Vol. 2, 1896*. Dover, New York (1945). 17

[59] Rayleigh, L. On a problem relating to the propagation of sound between parallel walls. *Philosophical Magazine Series 6*, **1**, 301 (1901). 17

[60] Floquet, G. Sur les equations differentielles linaires a coefficients presque-periodiques. *Ann. Sci. Ecole. Norm. Sup.*, **12**, 47 (1883). 23

[61] COMSOL AB. COMSOL MULTIPHYSICS (1986). 23

[62] Fabry, C. and Pérot, A. Sur les franges des lames minces argentées et leur application a la mesure de petites épaisseurs dair. *Ann. Chim. Phys.*, **12**, 459 (1897). 38, 96

[63] Liu, F., Cai, F., Ding, Y., and Liu, Z. Tunable transmission spectra of acoustic waves through double phononic crystal slabs. *Applied Physics Letters*, **92**, 103504 (2008). 42

[64] Brewster, D. On the Laws Which Regulate the Polarisation of Light by Reflexion from Transparent Bodies. *Philosophical Transactions of the Royal Society of London*, **105**, 125 (1815). 85

[65] Qi, D.X., Fan, R.H., Peng, R.W., Huang, X.R., Lu, M.H., Ni, X., Hu, Q., and Wang, M. Multiple-band transmission of acoustic wave through metallic gratings. *Applied Physics Letters*, **101**, 061912 (2012). 89

[66] Onda Corporation. Tables of Acoustic Properties of Materials (2003). 91

[67] Jacobi, W.J. Propagation of Sound Waves along Liquid Cylinders. *The Journal of the Acoustical Society of America*, **21**, 2 (1948). 94

[68] Becquerel, H. Sur les radiations émises par phosphorescence. *Comptes-rendus de l'Académie de sciences*, **122**, 420 (1896). 95

[69] Otto, A. Excitation of nonradiative surface plasma waves in silver by the method of frustrated total reflection. *Zeitschrift für Physik*, **216**, 398 (1968). 96

[70] Hibbins, A.P., Lockyear, M.J., and Sambles, J.R. Otto coupling to a transverse-electric-polarized mode on a metamaterial surface. *Physical Review B*, **84**, 115130 (2011). 96

[71] Bohm, D. *Quantum Theory*. Prentice-Hall, Englewood Cliffs (1951). 96

[72] Zhou, X. and Hu, G. Superlensing effect of an anisotropic metamaterial slab with near-zero dynamic mass. *Applied Physics Letters*, **98**, 263510 (2011). 96

[73] Liu, A., Zhou, X., Huang, G., and Hu, G. Super-resolution imaging by resonant tunneling in anisotropic acoustic metamaterials. *The Journal of the Acoustical Society of America*, **132**, 2800 (2012). 96, 121

[74] Voronina, N. An empirical model for elastic porous materials. *Applied Acoustics*, **55**, 67 (1998). 97

[75] Pochhammer, L. Beitrag zur Theorie der Biegung des Kreiscylinders. *Crelle*, **81**, 324 (1876). 108

[76] Morgan, D. *Surface Acoustic Wave Filters: With Applications to Electronic Communications and Signal Processing*. Studies in Electrical and Electronic Engineering. Elsevier Science (2010). ISBN 9780080550138. 108

[77] Meier, H. and Russer, P. Analysis of leaky surface acoustic waves on LiTaO$_3$ substrate. In *Proceedings of the 1992 IEEE Frequency Control Symposium*, pages 378–383. IEEE (1992). ISBN 0-7803-0476-4. 108

[78] Norris, A.N. Acoustic radiation and reflection from a periodically perforated rigid solid. *The Journal of the Acoustical Society of America*, **82**, 2113 (1987). 108

[79] Xue, L. and Fusco, V. Printed Holey Plate Luneburg Lens. *Microwave and Optical Technology Letters*, **50**, 378 (2008). 108

[80] Maci, S., Minatti, G., Casaletti, M., and Bosiljevac, M. Metasurfing: Addressing Waves on Impenetrable Metasurfaces. *IEEE Antennas and Wireless Propagation Letters*, **10**, 1499 (2011).

[81] Maci, S. and Kildal, P.S. Hard and Soft Gangbuster Surfaces. In *URSI International Symposium on Electromagnetic Theory*, pages 209–292 (2004).

[82] Kildal, P.S. Definition of Artificially Soft and Hard Surfaces for Electromagnetic Waves. *Electronics Letters*, **24**, 168 (1988).

[83] Sievenpiper, D., Zhang, L., Broas, R., and Yablonovitch, E. High-Impedance Electromagnetic Surfaces with a Forbidden Frequency Band. *IEEE Transactions on Microwave Theory and Techniques*, **47**, 2059 (1999).

[84] Park, Y., Herschlein, A., and Wiesbeck, W. A Photonic Bandgap (PBG) Structure for Guiding and Suppressing Surface Waves in Millimeter-Wave Antennas. *IEEE Transactions on Microwave Theory and Techniques*, **49**, 1854 (2001).

[85] Stone, E.K. and Hendry, E. Dispersion of Spoof Surface Plasmons in Open-Ended Metallic Hole Arrays. *Physical Review B*, **84**, 035418 (2011).

[86] Maradudin, A.A. and Leskova, T.A. Transformation of Surface Plasmon Polaritons by Surface Structures. *Physica B: Condensed Matter*, **405**, 2972 (2010).

[87] Maier, S.A. and Andrews, S.R. Terahertz Pulse Propagation using Plasmon-Polariton-like Surface Modes on Structured Conductive Surfaces. *Applied Physics Letters*, **88**, 251120 (2006).

[88] Maier, S., Andrews, S., Martín-Moreno, L., and García-Vidal, F. Terahertz Surface Plasmon-Polariton Propagation and Focusing on Periodically Corrugated Metal Wires. *Physical Review Letters*, **97**, 176805 (2006).

[89] Lockyear, M., Hibbins, A., and Sambles, J.R. Microwave Surface-Plasmon-Like Modes on Thin Metamaterials. *Physical Review Letters*, **102**, 073901 (2009).

[90] Liu, Y. and Zhang, X. Metasurfaces for Manipulating Surface Plasmons. *Applied Physics Letters*, **103**, 141101 (2013).

[91] Kim, K.J., Kim, J.E., Park, H.Y., Lee, Y.H., Kim, S.H., Lee, S.G., and Kee, C.S. Propagation of Spoof Surface Plasmon on Metallic Square Lattice: Bending and Splitting of Self-Collimated Beams. *Optics Express*, **22**, 4050 (2014).

[92] Hibbins, A.P., Hendry, E., Lockyear, M.J., and Sambles, J.R. Prism Coupling to 'Designer' Surface Plasmons. *Optics Express*, **16**, 20441 (2008).

[93] Garcia-Vidal, F.J., Martin-Moreno, L., and Pendry, J.B. Surfaces with Holes in Them: New Plasmonic Metamaterials. *Journal of Optics A: Pure and Applied Optics*, **7**, S97 (2005).

[94] Brock, E., Hendry, E., and Hibbins, A. Subwavelength Lateral Confinement of Microwave Surface Waves. *Applied Physics Letters*, **99**, 051108 (2011).

[95] Brock, E.M.G. and Hibbins, A.P. Microwave Surface Waves Supported by a Tapered Geometry Metasurface. *Applied Physics Letters*, **103**, 111904 (2013). 108

[96] Ritchie, R. Plasma Losses by Fast Electrons in Thin Films. *Physical Review*, **106**, 874 (1957). 108

[97] Mechel, F.P. *Formulas of Acoustics*. Springer, New York, second edition (2008). 110

[98] Lovelock, R., Murray, A.R.J., Ward, G.P., Hibbins, A.P., Sambles, J.R., and Smith, J.D. Slit Width Dependence of the Acoustic Transmission through a Thin Slit. *(Submitted)* (2014). 111

[99] Chang, L.L. Resonant tunneling in semiconductor double barriers. *Applied Physics Letters*, **24**, 593 (1974). 121

[100] Murray, A.R.J., Hendry, E., Summers, I.R., Sambles, J.R., and Hibbins, A.P. Control of the stop band of an acoustic double fishnet. *The Journal of the Acoustical Society of America*, **134**, 1754 (2013).

[101] Murray, A.R.J., Summers, I.R., Sambles, J.R., and Hibbins, A.P. Acoustic double fishnet using Helmholtz resonators. *The Journal of the Acoustical Society of America*, **Accepted** (2014).

[102] Carretero-Palacios, S., Murray, A.R.J., Martín-Moreno, L., and Hibbins, A.P. Broadband and broadangle extraordinary acoustic transmission through subwavelength apertures surrounded by fluids. *New Journal of Physics*, **16**, 083044 (2014).